論文 / 著書情報
Article / Book Information

題目(和文)	
Title(English)	Electrochemical Study on Dissolution Mechanism of Pt Catalyst for PEFC by In Situ Channel Flow Double Electrode
著者(和文)	王 中奇
Author(English)	Zhongqi Wang
出典(和文)	学位:博士(工学), 学位授与機関:東京工業大学, 報告番号:甲第10111号, 授与年月日:2016年3月26日, 学位の種別:課程博士, 審査員:西方 篤,多田 英司,須佐 匡裕,河村 憲一,上田 光敏
Citation(English)	Degree:Doctor (Engineering), Conferring organization: Tokyo Institute of Technology, Report number:甲第10111号, Conferred date:2016/3/26, Degree Type:Course doctor, Examiner:,,,,
学位種別(和文)	博士論文
Type(English)	Doctoral Thesis

Electrochemical Study on Dissolution Mechanism of Pt Catalyst for PEFC by In Situ Channel Flow Double Electrode

Advisor: Prof. Atsushi Nishikata

Assoc. Prof. Eiji Tada

Department of Metallurgy and Ceramics Science

Tokyo Institute of Technology

Zhongqi WANG

Chapter 1

Introduction

This dissertation was motivated by the recent efforts for the development of poly electrolyte fuel cells (PEFCs) in Japan and other countries. I constructed the dissertation around the topic of platinum (Pt) dissolution, because it is one of the critical issues that concern the durability of PEFCs.

1.1. Polymer electrolyte fuel cell

A PEFC is a device that produces electricity from the electrochemical oxidation of hydrogen (H_2) [1]. The basic components of a PEFC unit cell was illustrated in **Fig. 1.1**. The central part is a membrane electrode assembly (MEA), wherein a proton-conducting membrane is sandwiched between an anode and a cathode. On the anode, H_2 is oxidized (Eq. 1.1), while on the cathode O_2 is reduced (Eq. 1.2). The reactants, H_2 and O_2 gases, are transported to the electrodes by the porous gas diffusion layers (**Fig. 1.1**). Besides electricity, water (H_2O) is the only byproduct from a PEFC (Eq. 1.3).

$$\text{Anode:} \quad H_2 \rightarrow 2H^+ + 2e^- \qquad [1.1]$$

$$\text{Cathode:} \quad 4H^+ + O_2 + 4e^- \rightarrow 2H_2O \qquad [1.2]$$

$$\text{Overall:} \quad H_2 + 1/2O_2 \rightarrow H_2O \qquad [1.3]$$

The advantages of using the electricity produced by a PEFC is mostly favored for its zero emission of greenhouse gases. As shown in **Fig 1.2**, there is a real need to reduce such emissions in Japan, and indeed, the development and application of PEFC and other types of fuel cells are in the blueprint of Japan's energy plans [2]. Likewise, the PEFC technology seems also promising for alleviating the air pollutions in China, where coal are currently burned indifferently for getting heat in winter. Another merit of PEFC is its

relatively low operating temperature, normally below 90 ^{o}C. Such temperature makes a PEFC more amenable to frequent transitions like start-up and shut-down cycles than other types of fuel cells. By piling up hundreds of PFEC cells, a stack is manufactured (**Fig. 1.3**). And with the recent improvement, the PEFC stacks have already been put in the field in Japan for auto and residential usage; the representatives are Toyota's fuel cell vehicle Mirai and Tokyo-gas's fuel cell unit Enefarm (**Fig. 1.4**).

The current challenges for the mass production of PEFC and its applications are cost and durability [1, 3]. We need to reduce its cost and extend its durability. For both issues, use of Pt is in the central place. As reviewed by Schmidt et al., Pt still has to be contained in the cathode catalyst for the sluggish oxygen reduction reaction (ORR) [4]. As a result, the focus for the next decades becomes a tradeoff between how much Pt could be reduced from the current model to provide an enough power density required by the benchmarks [3] and how long the Pt can survive under the harsh environment of a PEFC in the field [5].

For reducing the amount of Pt in the cathode catalyst, we have to use Pt both economically and efficiently. Two main pathways may lead us to achieve the goal: enlarging the reactive surface area (m^2/g) by synthesizing smaller Pt nanoparticles (Pt NPs) [6], and boosting its intrinsic ORR activity (A/m^2) by alloying with transient metals [7] or even manipulating the active site [8-9]. However, the degradation of Pt in the varying PEFC catalyst seems to be universal [5]. The degradation of the Pt jeopardizes the kinetics of the oxygen reduction reaction (ORR) on the cathode and causes performance loss of a PEFC. A compromise between activity and durability of the Pt-based catalyst is always made. In the last decade, the degradation of Pt catalyst for PEFC has been intensively observed, and the complexity and lack of understanding remains the

main obstacles for move the activity-durability compromise.

1.2. Degradation of Pt in PEFCs

The model catalyst for the cathode is Pt nanoparticles (NPs) dispersed on high surface area carbon (Pt/C), and such catalyst is used as the standard for comparison with new-developed PEFC catalyst. As shown in **Fig. 1.5**, Meier et al. examined the degradation of Pt/C with identical location transmission electron microscopy (IL-TEM) [10]. They observed dissolution of Pt NPs, agglomeration of Pt NPs, and corrosion of carbon support on the Pt/C that experienced 10,000 simulated start-stop potential cycles (0.4-1.4 V_{RHE}). Similar degradation phenomena were also summarized by Ferreira et al. [11] and Shao-Horn et al. [12].

In an operating PEFC, the cathode sometimes exposes to potentials near 1.44 V during on-off cycles or H_2 starvations [13]. Such potential is much positive than the equilibrium potential of C/CO_2 which in aqueous solutions is about 0.2 V (Eq. 1.4) [14]. Thus, corrosion of the carbon support is inevitable in a sense, and has been observed in both PEFC cell and aqueous electrolytes after accelerated durability test (ADT) [15-19]. Carbon corrosion causes detachment of Pt NPs from the carbon support or sinking of the Pt NPs into the carbon agglomerate. Such phenomena are now visible, as shown by Hayashi et al. [20], using the combination of TEM and SEM, which allows both surface and transmitted images.

$$C + 2H_2O \rightarrow CO_2 + 4H^+ + 4e^- \qquad E^0 = 0.207\ V_{SHE} \quad [1.4]$$

For Pt NPs alone, the main degradation is the growth of their sizes [5, 11-12]. In

general, two mechanisms have been attributed for the size growth of the Pt NPs: agglomeration of Pt NPs through surface migration and dissolution-redeposition of Pt NPs.

1.2.1. Particle migration

Agglomeration of Pt NPs has been observed near 0.6 V_{SHE} [21]. As illustrated in **Fig. 1.6** the simplest case: two Pt NPs move towards each other on the carbon support and coalescence to form a larger Pt NP. The driving force comes from the trend to minimize the total surface energy of the Pt NPs, which declines with the growth of size. For this process, the mobility of NPs is critical, and a strategic way is to control such coalescence may be enlarging the inter-particle particle distance to about 10 nm [22], or replace the carbon with durable metal oxide [23-25] that binds the Pt NPs strongly.

1.2.2. Dissolution of Pt NPs

Besides particle migration, another mechanism of particle growth is the dissolution-redeposition process, which is referred as the Ostwald-ripening process in literature [11-12]. As illustrated in **Fig. 1.7**, tiny Pt NPs (d < 2 nm) dissolves and deposits on the nearby large Pt NP. Such process resulted evolution of the Pt NPs size distribution over potential cycles, as observed by et al. Myers et al. [26-27]. In addition, a fraction of dissolved platinum species (Pt^{n+}) diffuse into the membrane and get reduced by the crossover H_2 from the anode. Evidence supporting this mechanism is the observed Pt NPs, the Pt band, in the membrane after ADT of a PEFC cell [28-29]. Therefore, the dissolution of Pt NPs, a preliminary step that either leads to particle coarsening through Ostwald ripening or loss of Pt through precipitation in the membrane, is a major source of Pt degradation in

PEFC.

1.3. Pt dissolution in aqueous solutions

For understanding the nature of Pt dissolution, varying experiments were conducted in acidic aqueous solutions. The mostly used are 0.5 M H_2SO_4 and 0.1 M $HClO_4$ in recent years; the pH values of these two solutions are to mimic that in a PEFC. At equilibrium conditions, the Pourbaix diagram [30] of bulk Pt polycrystalline plate at 25 ^oC (**Fig. 1.8**) suggests that Pt dissolution (corrosion) occurs near 1.0 V_{SHE} in the pH region from 0 to −2. The rate determining step (rds) of the dissolution may be electrochemical (Eq. 1.5) or chemical (Eq. 1.6) reactions, depending on the electrolyte's pH and the electrode's potential.

$$Pt \rightarrow Pt^{2+} + 2e^- \quad [1.5]$$

$$PtO + 2H^+ \rightarrow Pt^{2+} + H_2O \quad [1.6]$$

The reported data, **Fig. 1.9**, differed from the thermodynamic prediction by the Pourbaix diagram, as generalized by Shao-Horn et al. in a recent review [12]. The measured solubility were higher than the calculated one from pourbaix diagram below 1.0 V, and decayed after 1.1 V, as highlighted by Wang et al. [31]. For Pt NPs, dissolution of Pt NPs was found to initiate from 0.6 to 0.9 V, a lower potential than that for bulky Pt. The downward shift of dissolution potential of the Pt NPs has been attributed to their nano sizes, as predicted by the Gibbs-Thomson effect (Eq. 1.7) [32]. The ab initio calculation suggested that the dissolution region on the pourbaix diagram expand for Pt NPs (**Fig. 1.10**).

$$\Delta E = -\Delta\mu/n \qquad [1.7]$$

Under potential cycles, Pt dissolution is found to be severer than that in the equilibrium conditions [26, 27, 33]. The enhancement was attributed to the repetition of formation and reduction of Pt oxide, but the mechanism is not fully understood. Even on bulk Pt sample, the Faradaic and non-Faradaic reactions (**Fig. 1.11**) need a retrospect, as pointed out by Jerkiewicz et al. [34]. The difficulty of understanding Pt dissolution is the lack of evidence. Only few technics like electrochemical quartz crystal microbalance (EQCM) [35-36] and inductively coupled plasma mass spectrometry (ICP-MS) [37-38] are available. Analysis by ICP-MS provides data of dissolution amount ($ngcm^{-2}$), but it is difficult to trace the dissolution rate upon the potential change that a PEFC requies. The EQCM presented mass change, but covered by other reactions.

In our group, a channel flow double electrode (CFDE) system, theoretically developed by Dr. Matsuda [39] and Dr. Aoki [40], was used for analyzing Pt dissolution under potential cycles by Dr. Yadav [41], Dr. Sugawara [42], and Dr. Shrestha [43]. The construction of the flow system and the CFDE cell are shown in **Fig. 1.12** and **Fig. 1.13**. In the double-electrode cell, which had a Pt working electrode (WE) and an Au collector electrode (CE), the dissolved Pt species (Pt^{n+}) from the WE precipitated on the CE that was set at 0.3 V (Eq. 1.). The precipitates of Pt on the CE after 2000 potential cycles was confirmed by electron probe micro-analyzer (EPMA) for a qualitative analysis. The results located the potential regions wherein Pt dissolution took place, and formed a preliminary mechanism of Pt dissolution, as proposed by Dr. Sugawara (**Fig. 1.14**) [33]. Later the precipitation current on the CE (I_{CE}) was analyzed by Dr. Shrestha discussed in his dissertation [43].

$$Pt^{n+} + ne^- \rightarrow Pt \quad [1.8]$$

1.4. Objective of this dissertation

The objective of this dissertation was to investigate Pt dissolution under a single potential cycle by using the in situ CFDE method. In detail, I wanted to understand valence of Pt species, influence of chloride, and dissolution behavior of carbon supported Pt nanoparticles.

1.5. Structure of this dissertation

I constructed this thesis with 6 chapters as shown in **Fig. 1.11**. Chapter 1 introduced the background of PEFC durability and reported data which are related to the topic of Pt dissolution. In chapter 2, I discussed the in situ CFDE method for analyzing Pt dissolution under potential cycling using bulk-like Pt in 0.5 M H_2SO_4. In Chapter 3, I investigated the effect of chloride on Pt dissolution with the help of a channel flow multi electrode setup. In Chapter 4, I tested commercial Pt fuel cell catalysts, and analyzed the dissolution of Pt PNs that were supported on high surface area carbon. In chapter 5, I discussed the findings from chapters 2 to 4, and distilled some new understanding of Pt dissolution. And chapter 6 summarized the dissertation.

References

1. M.K. Debe, *Nature*, **486**, 43 (2012).
2. Japanese Energy Basic Plan, (2014).
3. H.A. Gasteiger, S.S. Kocha, B. Sompalli, and F.T. Wagner, *Appl. Catal. B*, **56**, 9 (2005).
4. A. Rabis, P. Rodriguez, and T.J. Schmidt, *ACS Catal.*, **2**, 864 (2012).
5. R. Borup, J. Meyers, B. Pivovar, Y. S. Kim, R. Mukundan, N. Garland, D. Myers, M. Wilson, F. Garzon, D. Wood, P. Zelenay, K. More, K. Stroh, T. Zawodzinski, J. Boncella, J. E. McGrath, M. Inaba, K. Miyatake, M. Horii, K. Ota, Z. Ogumi, S. Miyata, A. Nishikata, Z. Shiroma, Y. Uchimoto, K. Yasuda, K. Kimijima, and N. Iwashita, *Chem. Rev.*, **107**, 3904 (2007).
6. H. Yano, M. Kataoka, H. Yamashita, H. Uchida, and M. Watanabe, *Langmuir*, **23**, 6438 (2007).
7. T. Toda, H. Igarashi, H. Uchida, and M. Watanabe, *J. Electrochem. Soc.*, **146**, 3750 (1999).
8. V.R. Stamenkovic, B. Fowler, B.S. Mun, G. Wang, P.N. Ross, C.A. Lucas, N.M. Markovic, *Science*, **315**, 493 (2007).
9. C. Chen, Y. Kang, J. Snyder, M. Mavrikakis, Y. Li, N.M. Markovic, G. Somorjai, Peidong Yang, V.R. Stamenkovic, *Science*, **343**, 1339 (2014).
10. J.C. Meier, C. Galeano, I. Katsounaros, A.A. Topalov, A. Kostka, F. Schuth, and K.J.J. Mayrhofer, *ACS Catal.*, 2 832 (2012).
11. P.J. Ferreira, G.J. la O', Y. Shao-Horn, D. Morgan, R. Makharia, S. Kocha, H.A. Gasteiger, *J. Electrochem. Soc.*, 152 (2005) A2256.
12. Y. Shao-Horn, W.C. Sheng, S. Chen, P.J. Ferreira, E.F. Holby, D. Morgan, *Top. Catal.*

46 (2007) 285.

13. C.A. Reiser, L. Bregoli, T.W. Patterson, J.S. Yi, J.D. Yang, M.L. Perry, T.D. Jarvi, *Electrochem. Solid-State Lett.*, 8 (2005) A273.
14. K. Kinoshita, *Carbon: Electrochemical and Physicochemical Properties, Wiley, New York, NY.*, 1988.
15. N. Takeuchi and T.F. Fuller, *J. Electrochem. Soc.*, **155**, B770 (2008).
16. A.P. Young, J. Stumper, and E. Gyenge, *J. Electrochem. Soc.*, **156**, B913 (2009).
17. Z.Y. Liu, J.L. Zhang, P.T. Yu, J.X. Zhang, R. Makharia, K.L. More, and E.A. Stach, *J. Electrochem. Soc.*, **157**, B906 (2010).
18. F. Wu, M. Wang, Q. Liu, H. Sun, S. Simonson, N. Ogbeifun, E.A. Stach, and J. Xie, *J. Electrochem. Soc.*, **157**, B1138 (2010).
19. M. Hara, M. Lee, C. Liu, B. Chen, Y. Yamashita, M. Uchida, H. Uchida, and M. Watanabe, *Electrochim. Acta*, **70**, 171 (2012).
20. A. Hayashi, M. Kitamura, Z. Noda, and K. Sasaki, International Fuel Cell Workshop 2015.
21. Q. Xu, T. He, and D.O. Wipf, *Langmuir*, **23**, 9098 (2007).
22. M. Watanabe, International Fuel Cell Workshop 2015.
23. K. Kakinuma, Y. Chino, Y. Senoo, M. Uchida, T. Kamino, H. Uchida, S. Deki, M. Watanabe, *Electrochim. Acta*, **110**, 316 (2013).
24. T. Daio, A. Staykov, L. Guo, J. Liu, M. Tanaka, S.M. Lyth, and K. Sasaki, *Sci. Rep.*, 5, 13126 (2015).
25. D. Takimoto, C. Chauvin, and W. Sugimoto, *J. Electrochem. Soc.*, **163**, F11 (2016).
26. J.A. Gilbert, N.N. Kariuki, R. Subbaraman, A.J. Kropf, M.C. Smith, E.F. Holby, D. Morgan, and D.J. Myers, *J. Am. Chem. Soc.*, **134** 14823 (2012).

27. R. K. Ahluwalia, S. Arisetty, X. Wang, X. Wang, R. Subbaraman, S. C. Ball, S. DeCrane, D. J. Myers, *J. Electrochem. Soc.*, 160 (7) (2013) F447.

28. E. Guilminot, A. Corcella, F. Charlot, F. Maillard, and M. Chatenet, *J. Electrochem. Soc.*, **154**, B96 (2007).

29. K. Yasuda, A. Taniguchi, T. Akita, T. Ioroi, and Z. Siroma, *Phys. Chem., Chem., Phys.*, **8**, 746 (2006).

30. M. Pourbaix, *Atlas of the Electrochemical Equilibria in Aqueous Solution, National Association of Corrosion Engineers, Houston*, 1974

31. X.P. Wang, R. Kumar, D.J. Myers, *Electrochem. Solid-State Lett.*, 9 (2006) A225-A227.

32. L. Tang, B. Han, K. Persson, C. Friesen, T. He, K. Sieradzki, and G. Ceder, *J. Am. Chem. Soc.*, **132** 596 (2010).

33. Y. Sugawara, T. Okayasu, A. P. Yadav, A. Nishikata, T. Tsuru, *J. Electrochem. Soc.*, 159 (11) (2012) F779.

34. L. Xing, M.A. Hossain, M. Tian, D. Beauchemin, K.T. Adjemian, G. Jerkiewicz, *Electrocatalysis*, **5**, 96 (2014).

35. A. P. Yadav, A. Nishikata, and T. Tsuru, *Electrochim. Acta*, 52, 7444 (2007).

36. G. Inzelt, B. Berkes, and A. Kriston, *Electrochim. Acta*, **55**, 4742 (2010).

37. A.A. Topalov, S. Cherevko, A.R. Zeradjanin, J.C. Meier, I. Katsounaros, and K.J.J. Mayrhofer, *Chem. Sci.*, **5**, 631 (2014).

38. P. Jovanovič, A. Pavlišič, V.S. Šelih, M. Šala, N. Hodnik, M. Bele, S. Hočevar, and M. Gaberšček, *ChemCatChem*, **6**, 449 (2014).

39. H. Matsuda, *J. Electroanal. Chem.*, **16**, 153 (1968).

40. K. Aoki, Doctoral dissertation, Tokyo Institute of Technology, 1978.

41. A.P. Yadav, A. Nishikata, T. Tsuru, *J. Electrochem. Soc.*, 156 (8) (2009) C253.

42. Y. Sugawara, Doctoral dissertation, Tokyo Institute of Technology, 2010.

43. B.R. Shrestha, Doctoral dissertation, Tokyo Institute of Technology, 2012.

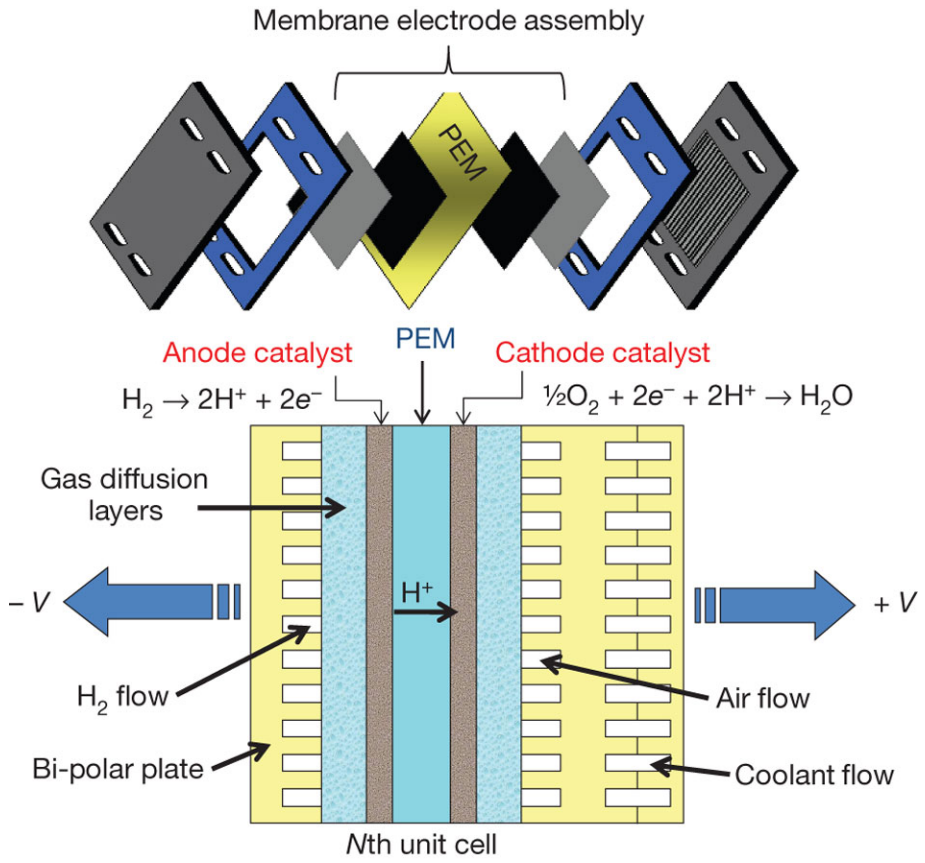

Fig. 1.1. A PEFC unit cell cross-section, showing the components of an expanded MEA [1].

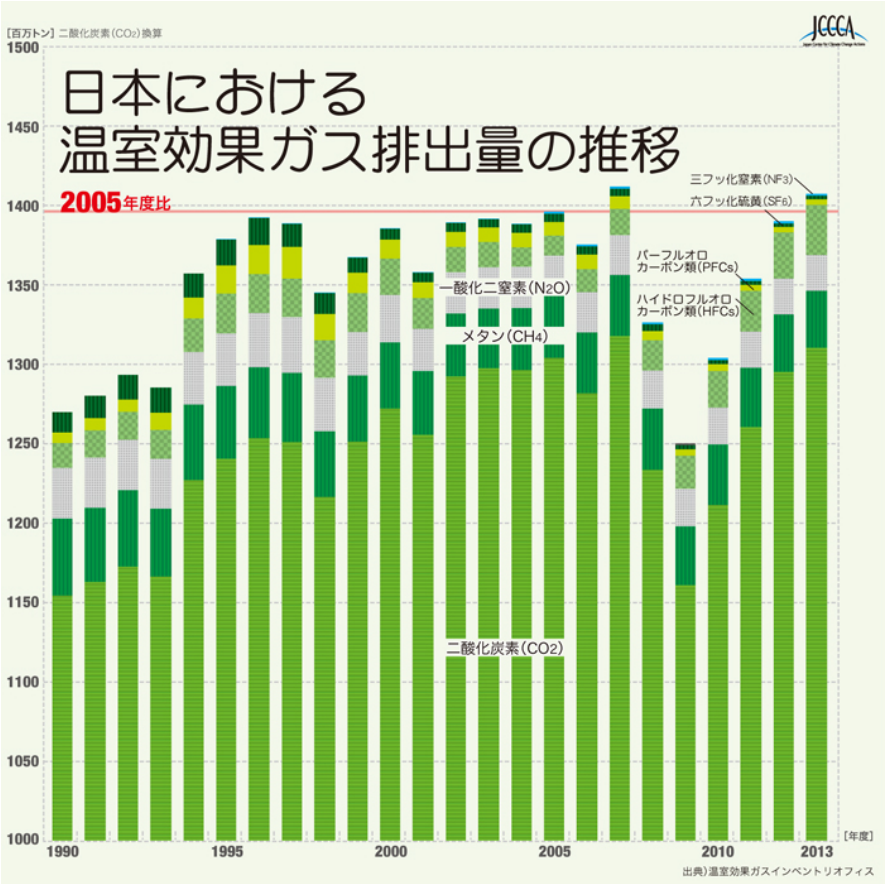

Fig. 1.2. Emissions of greenhouse gases in Japan subjected to Kyoto Protocol. Source: http://www.jccca.org/trend_japan/state/.

Fig. 1.3. A fuel cell stack from Honda. Source: http://www.car-revs-daily.com/2015/01/13/2015-honda-fcv-concept/.

Toyota Mirai

Tokyo-gas Enefarm

Fig. 1.4. Toyota's fuel cell vehicle Mirai, and Tokyo-gas's residential fuel cell unit Enefarm.
Source: (Mirai) http://toyota.jp/mirai/grade/,
(Enefarm) http://news.filehippo.com/2013/10/ene-farm-fuel-cell/.

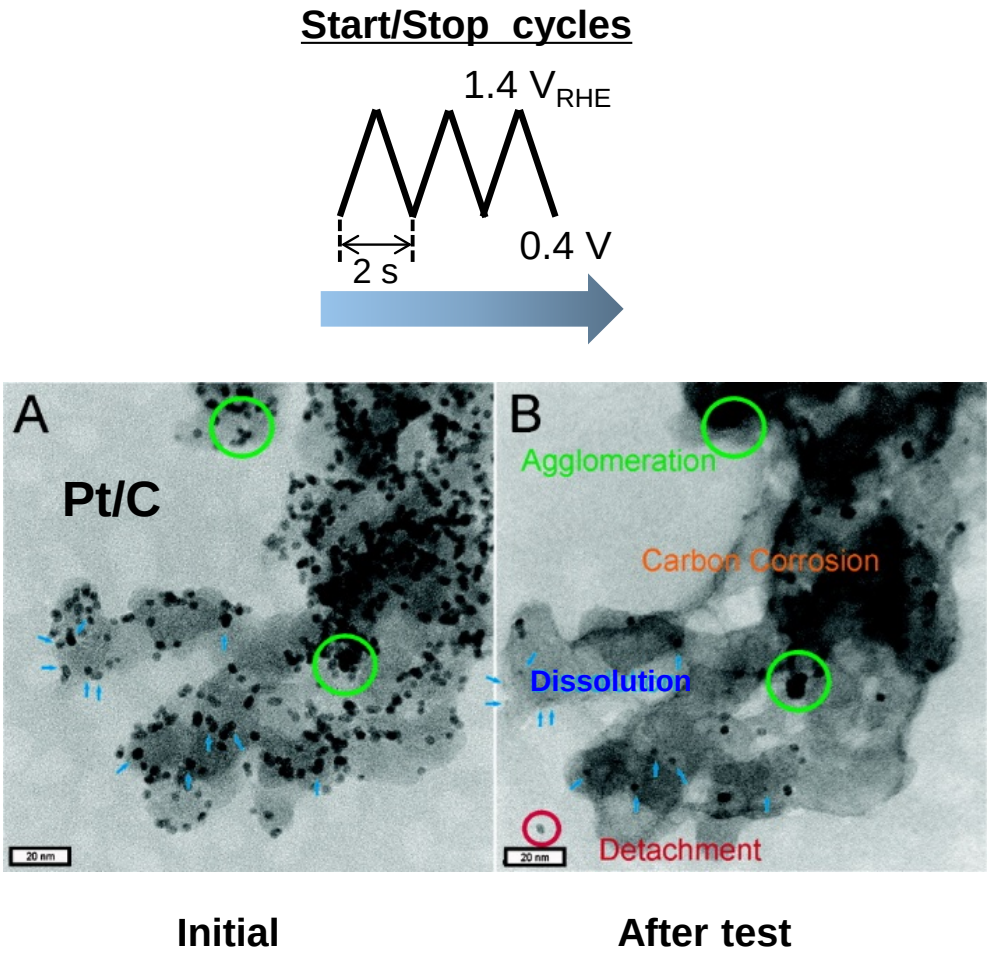

Fig. 1.5. Degradation of fuel cell catalyst under start-stop cycles examined by IL-TEM [10].

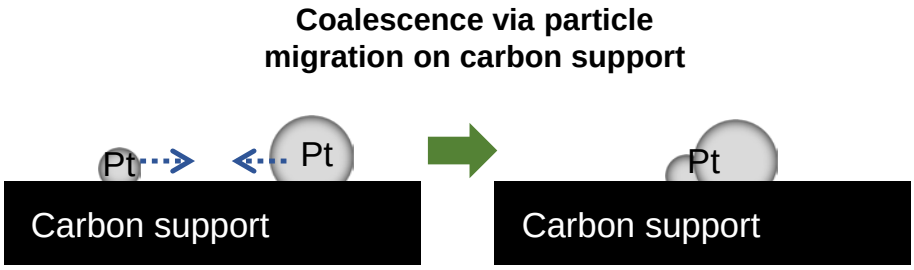

Fig. 1.6. Schematic of Pt/C degradation: coalescence of Pt NPs on the carbon support.

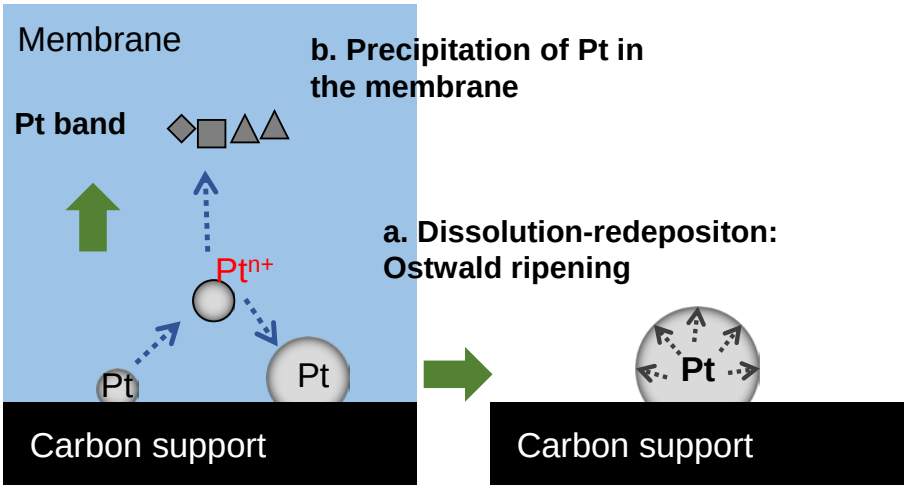

Fig. 1.7. Schematic of Pt/C degradation: dissolution of Pt NPs and redepositon on nearby Pt NPs (a), and precipitation in the membrane (b).

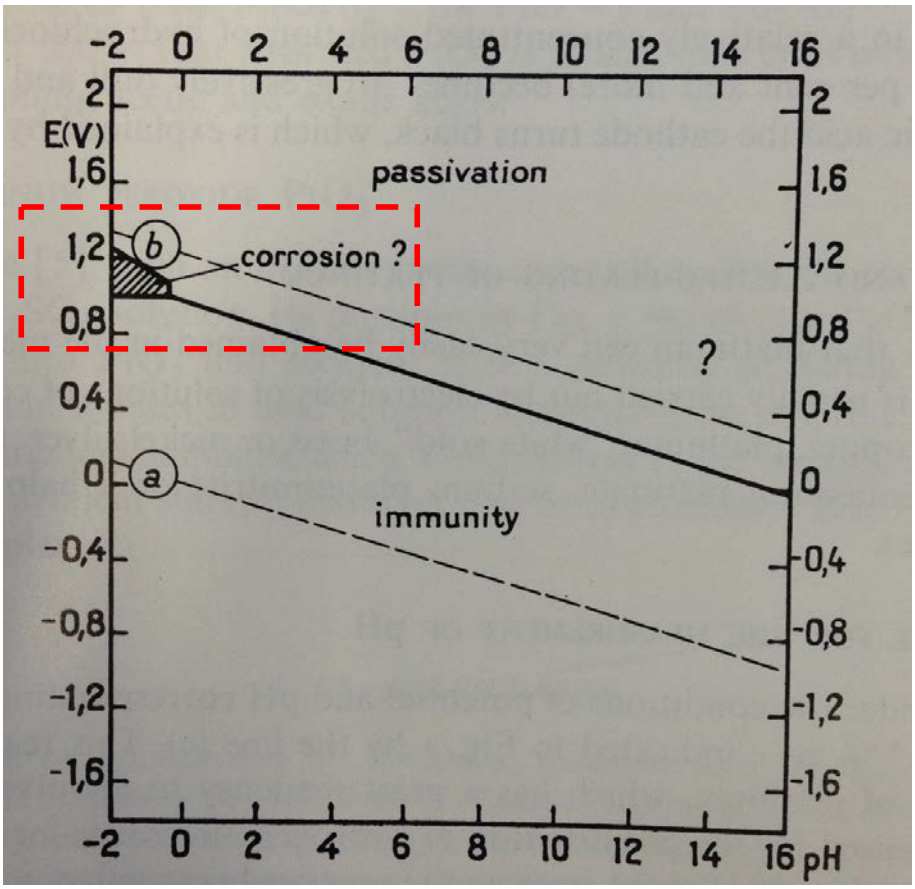

Fig. 1.8. Pourbaix diagram of bulk Pt at 25 ºC [30].

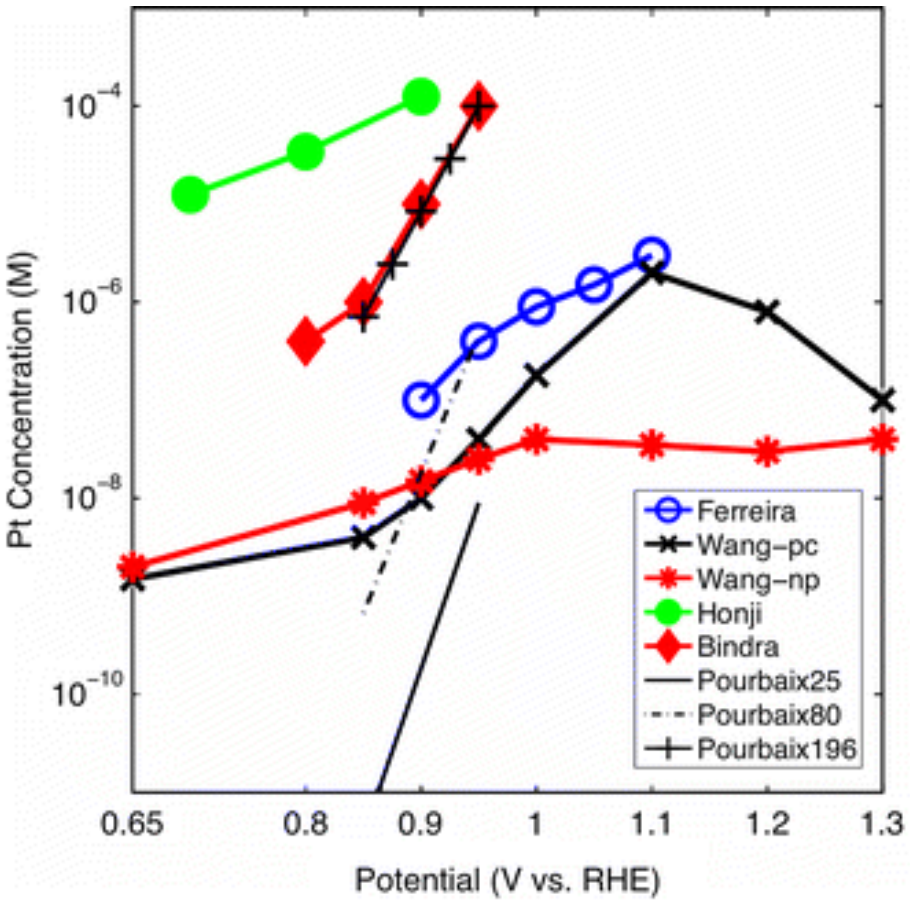

Fig. 1.9. The equilibrium dissolved Pt concentrations [12].

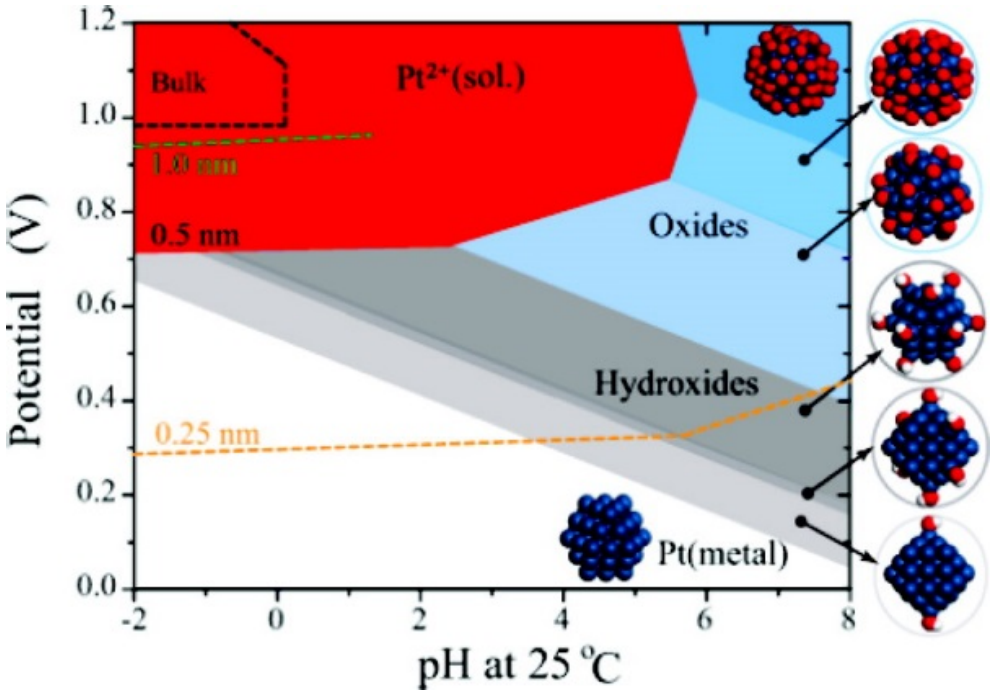

Fig. 1.10. Ab initio calculated Pourbaix diagram for a Pt particle with radius of 0.5 nm [32]. The stability region of Pt^{2+} in solution is shown in red.

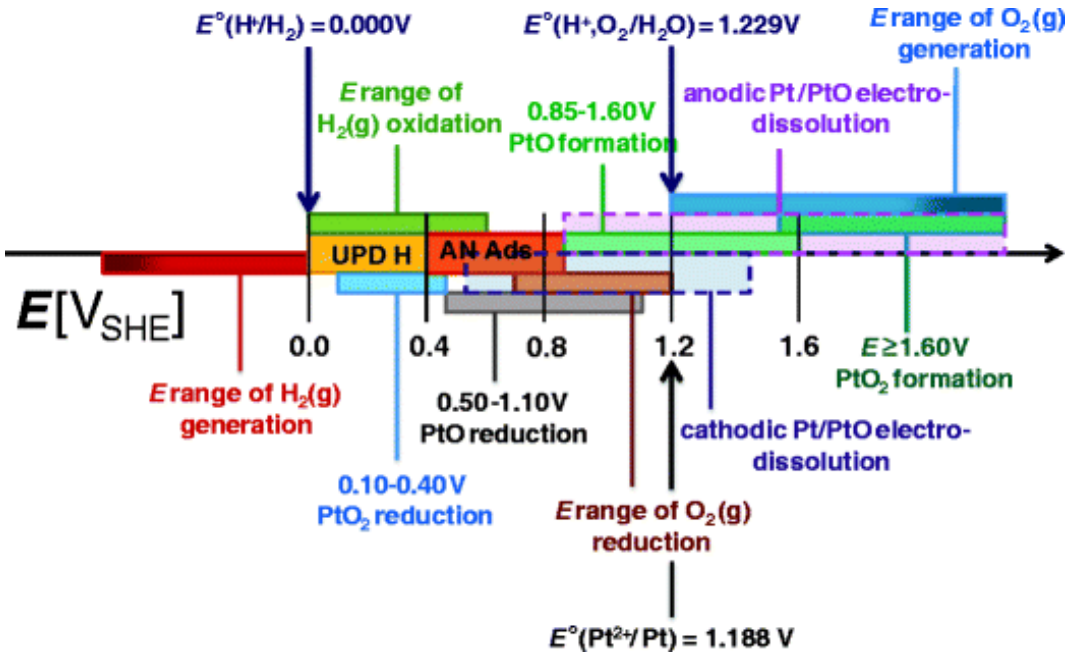

Fig. 1.11. Graphical representation of the main Faradaic and non-Faradaic reactions on Pt electrodes in an aqueous acidic electrolyte with an activity of H^+ equals to 1 [34].

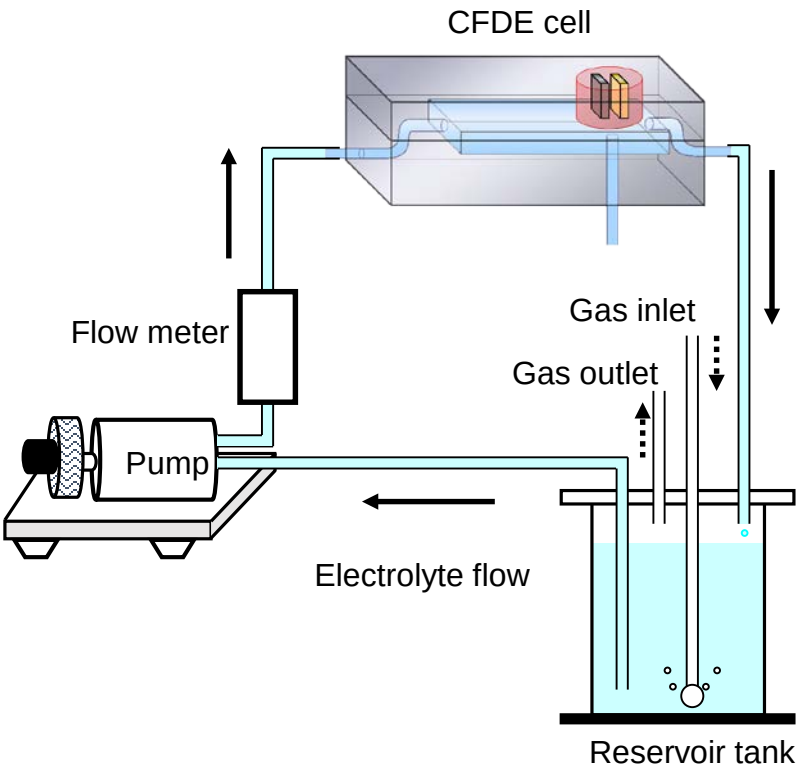

Fig. 1.12. Schematic of flow circuit for CFDE measurement [42].

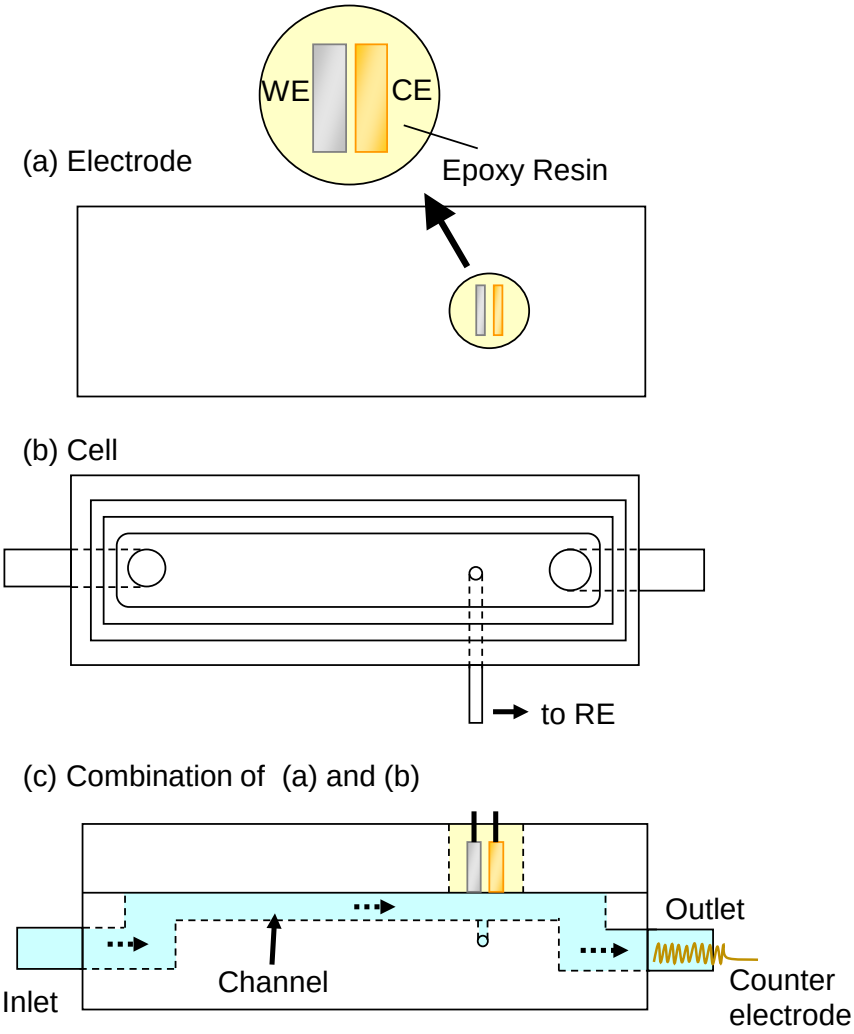

Fig. 1.13. Schematic of a CFDE Cell [42].

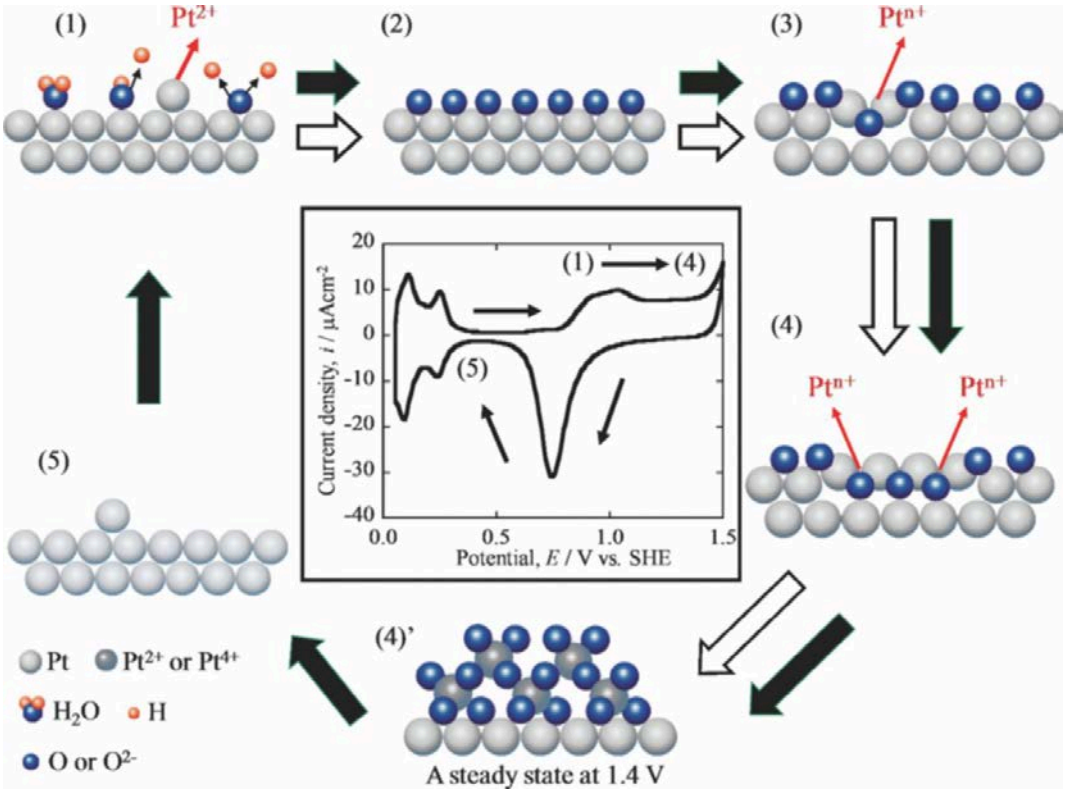

Fig. 1.14. A dissolution mechanism of bulk-like Pt under potential cycling proposed by Sugawara [33].

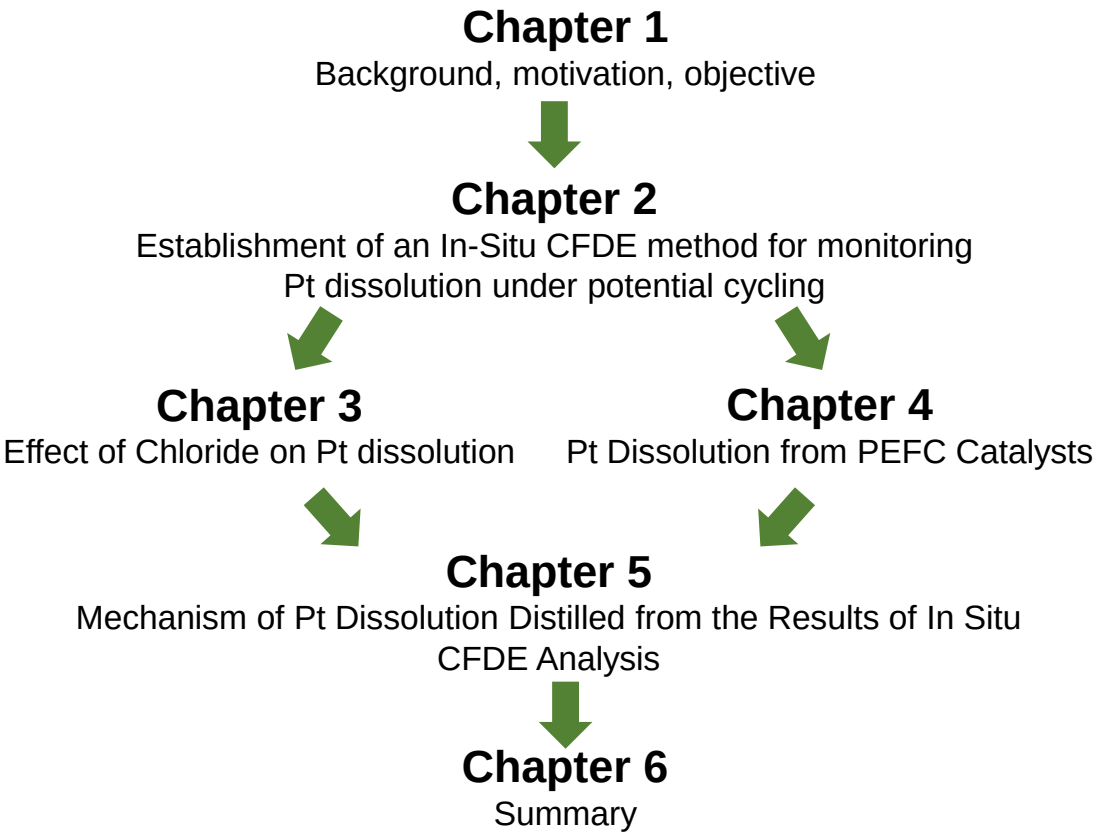

Fig. 1.15. Structure of this dissertation.

Chapter 2

Establishment of an In Situ CFDE Method for Monitoring Pt Dissolution under Potential Cycling

2.1. Introduction

In chapter 1, the role of Pt dissolution in the degradation of a PEFC was highlighted. In general, dissolution of Pt NPs resulted in the loss of electrochemical surface area (ECSA) for the cathode reaction ($1/2O_2 + 2H^+ + 2e^- \rightarrow H_2O$) [1-2]. A PEFC has to, in its lifetime, experience thousands of potential cycles, which accelerate Pt dissolution [3-5]. The potential conditions Pt experiences in a PEFC could be random. As recommended by the fuel cell commercialization conference of Japan (FCCJ), two standard waveforms are now used as protocols for testing the durability of a PEFC single cell (**Fig. 2.1**): a square wave between 0.6 and 1.0 V for the load changing cycle and a triangle wave between 1.0 and 1.5 V for the start/stop cycles [6]. Thus, to understand Pt dissolution in a PEFC, we have to make clear of its dependence on the changing potential. A way to get that answer is to obtain the real-time dissolution/potential behaviors within one potential cycle.

The first effort for such information was reported in 1970 by Johnson et al. [7]. They analyzed Pt dissolution on a bulk Pt electrode using a rotating ring-disk electrode (RRDE). Under potential cycling of the disk electrode, they observed some peaks in the ring current when it was set at certain potentials. As a conclusion, they highlighted the detection of Pt^{2+} from the electrochemical reduction of PtO_2. Similar results were also reported by Mitsushima et al. [8-9] and Meyers et al. [10].

In this chapter, I discuss a similar method for analyzing Pt dissolution under potential cycling using in situ CFDE. The CFDE system has a much lower noise level than the RRDE system [11], and its closed environment is more favorable for simulating the conditions of a PEFC [12]. Using the in situ CFDE, I discuss Pt dissolution under potential cycling with two upper potentials, E_U: 1.0 and 1.4 V corresponding to the two FCCJ protocols (**Fig. 2.1**). Both anodic and cathodic dissolution were covered, since

anodic Pt dissolution has also been reported elsewhere [13-18]. And formation of PtO_2 requires an upper potential limit (E_U) higher than 1.2 V [19-21]. To date, dissolution behavior under potential cycling below 1.0 V is unclear, though Pt dissolution under potentiostatic conditions in acidic solutions has been reported [15-16].

2.2. Experimental

Fig. 2.2 showed the geometry of a platinum working electrode (WE) and collector electrode (CE) of the CFDE employed for this chapter. These two electrodes (1 mm × 5 mm) were embedded in epoxy resin with a gap distance of 0.1 mm. The WE and CE were placed upstream and downstream, respectively.

In this dissertation, I considered only two oxidation states of Pt ions: 2^+ and 4^+, since they were the only stable states below 1.4 V, as reported by Beauchemin et al. [22]. The basic idea of in situ CFDE is that the dissolved Pt ions (Pt^{n+}) from the upstream electrode (Pt-WE) was detected at the downstream electrode (CE) using electrochemical reactions. For Pt^{2+}, it could be reduced to Pt by Eq. 2.2, or oxidized to Pt^{4+} by Eq. 2.3. For Pt^{4+}, it could be reduced to Pt^{2+} by Eq. 2.4, or to Pt by Eq. 2.5. As a result, the current on the CE (I_{CE}) served as a real-time signal for the dissolution rate on the WE.

$$Pt^{2+} + 2e^- \rightarrow Pt \quad [2.1]$$

$$Pt^{2+} \rightarrow Pt^{4+} + 2e^- \quad [2.2]$$

$$Pt^{4+} + 2e^- \rightarrow Pt^{2+} \quad [2.3]$$

$$Pt^{4+} + 4e^- \rightarrow Pt \quad [2.4]$$

From hydrodynamic analysis, the theoretical collection number (N) under a laminar flow condition was given by Eq. 2.1 [23].

$$N = 1 - F(\frac{\alpha}{\beta}) + \beta^{2/3}\{1-F(\alpha)\} - (1 + \alpha + \beta)^{2/3}[1 - F\{\frac{\alpha}{\beta}(1+ \alpha + \beta)\}] \qquad [2.5]$$

where

$$F(\theta) = \frac{3^{1/2}}{4\pi} ln\left\{\frac{\left(1+\theta^{1/3}\right)^3}{1+\theta}\right\} + \frac{3}{2\pi}\tan^{-1}\left(\frac{2\theta^{1/3}-1}{3^{1/2}}\right) + \frac{1}{4}$$

$$\alpha = \frac{x_2}{x_1} - 1 \quad \beta = \frac{x_3}{x_1} - \frac{x_2}{x_1}$$

N was independent of solution flow rate and was determined only by the dimensions of the electrodes. The N of the CFDE employed in this study was theoretically calculated to be 0.3, which meant that 30% of Pt ions from the WE were actually detected by the CE. This calculation was experimentally confirmed in a reversible system of $Fe(CN)_6^{4-}/Fe(CN)_6^{3-}$. The laminar flow condition was established under a flow rate from 10 to 60 cm/s. In this chapter, a flow rate of 10 cm/s was employed in all measurements to minimize consumption of the test solution.

Sulfuric acid (H_2SO_4) of 0.5 M was used as the test solution. It was deaerated with argon (Ar) gas for 24 h immediately prior to measurements being taken. The counter electrode was a gold (Au) wire placed at the downstream of the collector electrode (CE), and the reference electrode was a double-junction saturated silver/silver chloride electrode. The Luggin capillary of the reference electrode was placed 0.5 mm above the double electrode. All potentials in this study refer to the standard hydrogen electrode. Pt-NPs electrochemically deposited on an Au substrate were used as the WE [14], and a piece of glassy carbon (GC) or Au was used as the CE. All measurements were

performed at 25 °C on a multichannel potentiostat (PS-08, Toho Technical Research, Japan).

The detection potential, E_{CE} = 0.3 V, was determined from electric charges recorded on the CE polarized at various potentials when the Pt-WE underwent CV from 0.05 to 1.0 V at 20 mV/s. The validity was confirmed by ICP–MS as follows. The GC-CE was maintained at 0.3 V and the WE underwent 3000 cycles of CV between 0.05 and 1.0 V at 20 mV/s. After 3000 cycles, the CE was immersed in 10% aqua regia for 24 h to dissolve the collected Pt. The immersion solution was diluted to 5% and analyzed by ICP–MS (Agilent Technologies Inc., 7700x). The analysis is described in detail in the next section.

2.3. Results and discussion

2.3.1. Potentials for reduction of Pt^{2+} and Pt^{4+} aquo ions on GC

Fig. 2.3 showed the CV of Pt-NPs between 0.05 and 1.0 V in 0.5 M H_2SO_4 in a CFDE. In an anodic scan, Pt–O formation started at approximately 0.8 V. Up to 1.0 V, the coverage of Pt–O was estimated to be approximately 42% of a monolayer (ML) from the amount of the anodic charge. In a cathodic scan, reduction of Pt–O occurs from 1.0 to 0.6 V. Detailed surface oxide formation and reduction during potential cycling is discussed in the literature [19-21]. All CVs were performed between 0.05 and 1.0 V (or 1.4 V), and in subsequent figures, only the region above 0.4 V is plotted. The region below 0.4 V was related to hydrogen adsorption/desorption and was not immediately relevant, except for the calculation of the ECA.

Fig. 2.4 showed the changes in the I_{CE} on the GC-CE polarized at various potentials (E_{CE} = 0.8, 0.5, and 0.3 V) when the Pt-WE underwent CV between 0.05 and 1.0 V at 20 mV/s. When E_{CE} was higher than 0.5 V, the I_{CE} remained constant; it did not change with

the potential (E_{WE}) of the WE. This result indicates that, when E_{CE} > 0.5 V, no Pt ions (Pt^{2+}, Pt^{4+}) were reduced on the CE. When the potential of the collector electrode (E_{CE}) was held at 0.3 V, the collector current was constant when the potential of the WE is below 0.6 V. This cathodic current represented the reduction (Eq. 2.6) of residual O_2 and was regarded as the residual current ($I_{CE(R)}$) on the CE.

$$O_2 + 4H^+ + 4e^- \rightarrow 2H_2O \qquad [2.6]$$

The $I_{CE(R)}$ ranged from −5 to −10 nA in the sufficiently deaerated solution. In all the following plots, the I_{CE} was plotted after subtraction of the $I_{CE(R)}$. From 0.6 V, the I_{CE} started to increase cathodically and became constant at approximately 0.8 V. This cathodic increase of I_{CE} indicated reduction of Pt^{2+} and Pt^{4+} on the CE (Eqs. 2.2 and 2.3). The electric charge due to the reduction on CE was obtained by integration of the I_{CE} when WE was scanned from 0.4 to 1.0 V. The electric charges Q_C divided by ECA vs. E_C were plotted in **Fig. 2.5**. It can be seen that Pt ions were not detected above 0.6 V. The Q_C started to increase from E_{CE} = 0.5 V and became constant at approximately 0.3 V. On the basis of this result, we selected 0.3 V as the potential for reduction of Pt^{2+} and Pt^{4+} aquo ions on GC-CE. A similar result was obtained on an Au-CE.

Increase of the I_{CE} from 0.6 V (E_{CE} = 0.3 V in **Fig. 2.4b**) might have been caused not only by the detection of Pt ions, but also by a change in $I_{CE(R)}$ on the CE. The $I_{CE(R)}$ on the downstream electrode (CE) might be affected by oxygen reduction reaction (ORR) on the upstream electrode (WE). The $I_{CE(R)}$ on the downstream CE might be suppressed when the upstream WE is scanned in the potential range where oxygen reduction occurs on the WE because oxygen is consumed on the WE.

2.3.2. Comparison of collected Pt on the CE between CFDE and ICP–MS

To confirm the reliability of the I_{CE} as a detection parameter of Pt dissolution, the deposited Pt on the CE was examined by ex-situ ICP–MS after 3000 cycles of CV. In **Fig. 2.6**, CV of Pt-WE (a) and the I_{CE} of GC-CE (b) at 5th and 500th cycle are shown. In early cycles (< 20), the $I_{CE(R)}$ on the CE is constant; it does not change with E_{WE} from 0.4 to 0.6 V. However, after a large number of cycles, $I_{CE(R)}$ started to linearly increase with E_{WE}, as shown in **Fig. 2.6b**. The nature of this behavior was unclear. Technically, it did not affect the in-situ application of CFDE in which only five cycles of CV are performed. In this 3000-cycle experiment, nevertheless, when the Q_C was calculated by integrating the I_{CE} with time, it was assumed that $I_{CE(R)}$ on the CE linearly changes with E_W (**Fig. 2.6**). The I_{CE} for 3000 cycles was integrated and shown in **Fig. 2.7**. The Q_C of each cycle decreases with the number of cycles until 1500 cycles and then becomes constant. Assuming that Pt dissolves as Pt^{2+} in the potential from 0.6 to 1.0 V, the total amount of Pt collected on the CE was calculated to be 65 ng (2.9 ML) from the obtained Q_C. After collection of Pt^{2+} for 3000 cycles, the CE was immersed in aqua regia to dissolve the collected Pt for detection by ICP–MS. The amount of Pt detected by ICP–MS was 53 ng for 3000 cycles. The ICP–MS results at E_{CE} = 0.3 and 0.8 V were compared with the Q_C in **Table 2.1**. It can be seen that the amount (53 ng) detected by ICP–MS was in good agreement with the CFDE data (65 ng) at E_{CE} = 0.3 V. In addition, at E_{CE} = 0.8 V, it was confirmed by ICP–MS that Pt was not present on the CE. The consistency between CFDE and ICP–MS results indicates that the dissolution amount calculated from I_{CE} is reliable.

Table 2.1. Comparison of collected Pt on CE between CFDE and ICP–MS.

E_C	Cycles	ΔW_{CFDE} /ng	$\Delta W_{ICP\text{-}MC}$ /ng
0.3 V	3,000	65.0 (2.9 ML)	52.5 (2.3 ML)
0.8 V	1,000	0	0

ML: Monolayer

The amount of Pt dissolved from the WE per cycle was calculated from the integration of the I_{CE} in each cycle as Pt^{2+} dissolution. The calculation results and normalized ECA loss by the initial ECA (approximately 0.96 cm^2) vs. the cycle number are plotted in **Fig. 2.8**. The plots showed a trend similar to that observed for Pt collected on the CE, i.e., a decrease relative to cycle number in the first 1000 cycles and then almost constant. In the first 1000 cycles, the ECA of the Pt-WE decreased by approximately 50%.

Let us consider the case where the ECA loss was caused by dissolution of Pt-NPs. The employed Pt-WE produced by electroplating consisted of larger particles of several tens of nanometers and possibly finer particles less than 10 nm on the surface of the larger particles. Suppose, for instance, n pieces of Pt-NPs with radius r completely dissolve out in the first 1000 cycles. The mass ΔW_{1000} of dissolved Pt in the first 1000 cycles is given by Eq. 2.7.

$$\Delta W_{1000} = nVd = n(4\pi r^3/3)d \qquad [2.7]$$

where V is the volume of a particle and d is the density of Pt. The ECA loss ΔECA due to dissolution of these Pt-NPs is given by

$$\Delta ECA = n(4\pi r^2). \quad [2.8]$$

By substituting Eq. 2.7 into Eq. 2.8, we can obtain ΔECA as follows:

$$\Delta ECA = \Delta W_{1000} / (r/3)d. \quad [2.9]$$

The amount of Pt dissolution during the first 1000 cycles is obtained as ΔW_{1000} = 109.57 ng by integration of the data shown in **Fig. 2.8**. By Eq. 2.9, ΔECA is calculated to be approximately 0.15 cm^2 for $r = 10^{-7}$ cm (1 nm). The calculated ΔECA from the amount of Pt dissolution is much smaller than the obtained ECA loss (approximately 0.48 cm^2). It seems that the coarsening of Pt-NPs, described in chapter 1, was caused by dissolved Pt ions from finer particles, which are primarily being redeposited on larger particle surfaces or by surface diffusion of Pt atoms induced by potential cycling.

2.3.3. Specification of Pt^{2+} and Pt^{4+} dissolved in one cycle of CV

In an operating PEFC, the cathode is inevitably exposed to high potentials (1.44 V) during on–off cycles or when fuel starvation occurs [24]. Pt dissolution increases with the upper potential E_U of potential cycling, particularly above 1.2 V [17-18, 25-26]. The possible mechanism of this enhancement is that adsorbed O penetrates into the Pt lattice and forms a three-dimensional (3-D) oxide that induces Pt dissolution [18]. In this section, Pt dissolution in the potential range up to 1.4 V is discussed. In **Fig. 2.9**, both Pt^{2+} and Pt^{4+} ions are detected by the reduction reactions shown in Eqs. 2.2 and 2.3 on Au-CE at E_{CE} = 0.3 V. **Fig. 2.10** indicates detection of only Pt^{4+} by the reduction reaction shown in Eq. 2.5 on Au-CE at 0.5, 0.7, and 0.9 V. In **Fig. 2.11**, only Pt^{2+} is collected by the oxidation reaction shown in Eq. 2.4 on Au-CE at 1.3 and 1.4 V.

In **Fig. 2.9**, the I_{CE} starts to increase at 0.6 V, becomes constant at 0.8 V, and remains constant until 1.2 V. This indicates that dissolution of Pt^{2+} starts at

approximately 0.6 V and increases with potential until 0.8 V where Pt–O formation starts. From 0.8 to 1.2 V, Pt^{2+} dissolution occurs in parallel with Pt–O growth. From 1.2 V, the I_{CE} starts to dramatically increase, and this increase of the I_{CE} is also identified as dissolution of Pt^{4+} by setting the CE at 0.7 V (**Fig. 2.10**). At E_{CE} = 0.7 V, Pt^{4+} is reduced to Pt^{2+} on the CE (Eq. 2.5). When the CE was maintained at 0.7 V, no Pt deposition was observed on the CE after 2000 cycles of CV from 0.00 to 1.4 V [14],which proves that neither Pt^{4+} nor Pt^{2+} are reduced to Pt at 0.7 V. When the CE is set at 0.7 V (**Fig. 2.10**), the I_{CE} remains constant when E_{WE} < 1.2 V; no Pt^{4+} is detected. This result confirms that Pt dissolves as Pt^{2+} below 1.2 V, as detected on a CE polarized at 0.3 V (**Fig. 2.9**). From 1.2 V, this increase of the I_{CE} (**Fig. 2.10**) indicates detection of Pt^{4+} on the CE (Eq. 2.5). The charge integrated above 1.2 V (both anodic and cathodic scans) at E_{CE} = 0.7 V is 48% of that at E_{CE} = 0.3 V. This percentage of charge implies that, at E_{CE} = 0.7 V, Pt^{4+} is reduced to Pt^{2+} by a two-electron reduction (Eq. 2.5), whereas at E_{CE} = 0.3 V, Pt^{4+} is reduced to Pt by a four-electron reduction (Eq. 2.3). When E_{CE} is 0.9 V (**Fig. 2.10**), detection of Pt^{4+} above 1.2 V on the CE is smaller than that at 0.7 V, whereas the detection at 0.5 V is approximately equal to that at 0.7 V. This result indicates that 0.7 V was suitable to detect Pt^{4+} by reduction of Pt^{4+} to Pt^{2+}.

The above results showed that Pt dissolution is not suppressed by a full ML of Pt–O formed at approximately 1.2 V under CV.As the potential increases, penetration of O into the Pt lattice forms 3-D PtO_2 and triggers Pt^{4+} dissolution. In addition, the dissolution of Pt^{4+} increases with potential. Moreover, the I_{CE} at both E_{CE} = 0.7 and 0.3 V indicates that Pt^{4+} dissolution continues in cathodic scan from 1.4 V to 1.2 V before the main reduction of PtO_2.

In cathodic scan, as reduction of PtO_2 starts, dissolution of Pt^{2+} occurs [7-10]. The I_{CE} at E_{CE} = 0.3 V (**Fig. 2.9**) shows that Pt^{2+} dissolution occurs in the cathodic scan. Furthermore, Pt^{2+} dissolution in cathodic scan is detected when the CE is polarized at E_{CE} = 1.4 V (**Fig. 2.11**), where Pt^{2+} is oxidized to Pt^{4+} (Eq. 2.4). When E_{CE} = 1.4 V, the I_{CE} remains constant above 1.2 V in CV; however, no Pt^{2+} is detected. Thus, Pt dissolves only as Pt^{4+} above 1.2 V. In the cathodic scan, an anodic peak in the I_{CE} from 1.1 to 0.7 V indicates the detection of Pt^{2+} (**Fig. 11**) when the CE was set at 1.4 V, whereas at 1.3 V no peak was observed. This result was similar to those reported on an RRDE [7] and indicates that Pt^{2+} is oxidized at 1.4 V. The amount of Pt^{2+} dissolution in the cathodic scan detected at 1.4 and 0.3 V are in agreement (**Table 2.2**). This agreement implies that Pt dissolves as Pt^{2+} in the cathodic scan below 1.2 V from the reduction of PtO_2, and that Pt^{2+} can be detected either by reduction (at 0.3 V) or further oxidation (at 1.4 V); both detections are reliable.

In the cathodic scan, dissolution of Pt^{2+} terminates before the surface oxide is completely reduced (**Fig. 2.11**). This result implies that the surface oxide form in the anodic scan consists of a layer of PtO_2 at the top and a layer of PtO at the bottom. In the cathodic scan, most of the PtO_2 is reduced to Pt (Eq. 2.10), whereas a small fraction of PtO_2 is reduced to Pt^{2+} (Eq. 2.11), which dissolves from the Pt-WE. After the reduction of PtO_2 terminates, reduction of PtO (Eq. 2.12) starts.

$$PtO_2 + 4H^+ + 4e^- \rightarrow Pt + 2H_2O \qquad [2.10]$$

$$PtO_2 + 4H^+ + 2e^- \rightarrow Pt^{2+} + 2H_2O \qquad [2.11]$$

$$PtO + 2H^+ + 2e^- \rightarrow Pt + H_2O \qquad [2.12]$$

In this study, the expected anodic peak in I_{CE} during anodic scan from 0.6 to 1.2 V at E_C = 0.7 V that represents the detection of Pt^{2+} did not appear; the I_R on the Au-CE is affected by some unknown side reactions on the WE and CE. Nevertheless, dissolution of Pt^{2+} below 1.2 V is quantified by I_{CE} when the CE is polarized at 0.3 V. Thus, dissolution of Pt^{2+} and Pt^{4+} in one cycle of CV is specified. The amount of Pt^{2+} and Pt^{4+} dissolved in different potential regions within one cycle is calculated by the I_{CE} and N and is summarized in **Table 2.2**. As a result, 1.2 V is distinguished as a transient potential where Pt^{2+} dissolution changes to Pt^{4+} dissolution. This transition could be caused by the formation of 3-D PtO_2 through the place exchange of Pt and O. This result indicates that Pt dissolution is not suppressed by coverage of one ML of Pt–O under CV. Formation of 3-D PtO_2 triggers dissolution of Pt^{4+}, which increased with potential. A comparison of Pt^{2+}/Pt^{4+} and anodic/cathodic in **Fig. 2.12**.

2.3.4. Effect of scan rate

Under potential cycling, the repeated oxidation and reduction cycles of the Pt surface facilitate dissolution [25-27]. In particular, the scan rate (ν) of potential cycling proved to be of interest for studying the mechanism of Pt dissolution.

Jerkiewicz et al. showed that the average amount of Pt dissolution per cycle increased when ν decreased from 500 to 25 mV/s [26]. However, this dependence was reversed when the dissolved amount was normalized against time. Topalov et al. observed similar trends in an electrochemical flow cell [27]. In addition, they confirmed the occurrence of anodic dissolution above ca. 1.1 V during oxide formation and that of cathodic dissolution in parallel with the oxide reduction. Previous studies using a CFDE identified Pt^{4+} and Pt^{2+} as anodic and cathodic dissolution products. The anodic

dissolution results from the interfacial place exchange between the adsorbed O atoms and the topmost Pt atoms. On the other hand, the cathodic dissolution correlates with the reduction of unstable PtO_2. These two dissolutions govern the electrochemical surface area loss of Pt during potential cycling for an upper potential limit exceeding 1.4 V, which often occurs on the PEFC cathode during Start/Stop cycles [24]. The influence of scan rate on these dissolutions needs to be studied in detail for a deeper understanding of the Pt dissolution mechanism.

In this chapter, the instantaneous dissolution behavior of a Pt thin film was examined by in situ analysis using a CFDE. The study focused on the ν-dependence of this dissolution for values ranging between 200 and 0.5 mV/s. Both anodic and cathodic dissolution were discussed.

The WE underwent potential cycling between 0.05 and 1.4 V at scan rates of 0.5, 5, 20, 100, and 200 mV/s. The Pt dissolution was detected by setting the CE potentials. To detect Pt^{n+} ions, the CE potential was set at 0.3 V, where Pt^{n+} was reduced to Pt (Eq. 2.1). The dissolution of Pt^{4+} was detected when CE was set at 0.7 V because of the reduction of Pt^{4+} to Pt^{2+} (Eq. 2). On the other hand, the dissolution of Pt^{2+} was detected at the CE set at 1.4 V, which corresponds to the oxidation of Pt^{2+} to Pt^{4+} (Eq. 3).

The CVs of the Pt-WE measured in the CFDE system are shown in **Fig. 2.13**. Surface oxidation and reduction rates decreased when ν decreased from 100 to 5 mV/s (**Fig. 2.13a**). When the Pt surface was scanned at extremely slow speed, steady-state reactions occurred instead of transient reactions. The CV of the Pt-WE showed a very small hysteresis between anodic and cathodic scans at 0.5 mV/s (**Fig. 2.13b**), which is typical of a quasi-steady-state behavior. The oxidation of Pt proceeded at a very slow rate in the high-potential region and residual oxygen underwent reduction on the WE

electrode in the low potential region. The peak corresponding to oxide reduction was indistinguishable in the cathodic scan. These two dissolutions differ and their dependence on ν is discussed in the following sections.

2.3.4.1 Effect of scan rate on anodic dissolution

Pt dissolution during oxide formation in anodic scans has previously been reported by Topalov et al. [25] and Gaberšček et al. [27]. The dissolved species was detected as Pt^{4+} in our CFDE system on a CE set at 0.7 V. **Fig. 2.14** shows CE (I_{CE}) and WE currents (I_{WE}) during anodic scans. This anodic Pt^{4+} dissolution may proceed by reaction of PtO with H^+ (Eq. 4) [18]. However, its influence on I_{WE} was indistinguishable (**Fig. 2.14a**) because of the large difference between I_{WE} and I_{CE}.

$$PtO + 2H^+ \rightarrow Pt^{4+} + H_2O + 2e^- \qquad [2.13]$$

This anodic dissolution [17-18] may stem from the interfacial place exchange between adsorbed oxygen atoms (O_{ad}) and topmost Pt atoms [20] because its onset potential is close to that of the place exchange. After place exchange, PtO_2 appeared to develop (Eq. 5), consistent with previous reports suggesting that PtO_2 forms under extensive potential holding at high potentials such as at 1.4 V [19, 21, 28-29].

$$PtO + H_2O \rightarrow PtO_2 + 2H^+ + 2e^- \qquad [2.14]$$

The I_{CE} in **Fig. 2.14b**, recorded on a CE at 0.7 V, traced dissolution of Pt^{4+} on the WE in anodic scans. The I_{CE} remains at its base current in low potential region, and starts

increasing at a high potential (onset potential, E_{onset}), indicating reduction of Pt^{4+} to Pt^{2+} (Eq. 2) on the CE. It can be seen from the I_{CE} that changing the ν did not cause significant difference (e.g. 10 times) in the instantaneous dissolution; the I_{CE} values were on a similar level considering the reproducibility of the data.

However, the I_{CE} showed two characteristic changes below 20 mV/s regarding the initiation and inhibition of the anodic Pt^{4+} dissolution. First, concomitant with an increase in I_{CE}, E_{onset} shifted towards a more negative value when ν decreased from 20 to 0.5 mV/s (**Fig. 2.15**). At 0.5 mV/s, a negligible increase of I_{CE} from 0.5 to 0.8 V may be caused by the steady-state reactions on the WE, Pt^{4+} dissolution was not likely to occur in this region [18, 25]. This shift of Pt^{4+} dissolution initiation below 20 mV/s suggests that the place exchange process, described by Jerkiewicz et al. [20] and sugawara et al. [18], may be affected by the ν.

Second, the anodic Pt^{4+} dissolution increased with increasing potential at high ν but stopped in the high potential region at low ν. Specifically, I_{CE} rose steadily when the potential increased from 1.2 V until the end of the anodic scan at 20 mV/s. On the other hand, at 0.5 mV/s, I_{CE} increased when the potential increased from 1.05 to ca. 1.13 V but retrieved afterwards. The suppression of this dissolution at 0.5 mV/s originates from the presence of stable oxides, such as β-PtO_2, which may develop after place exchange. The formation of β-PtO_2-like oxides has previously been detected by Imai et al. on a Pt surface kept at 1.4 V for more than 100 s [19]. The inhibitory effect of this oxide on Pt dissolution has been also observed under potentiostatic conditions [15-16, 18], where the dissolution only occurred at the very beginning of the polarization but was quickly suppressed to a great extent upon oxide formation. Above 20 mV/s, the Pt^{4+} dissolution

increases with potential until the end of anodic scan. Inhibition of dissolution by surface oxide is trivial, suggesting that stable oxide is yet developed in this potential region.

2.3.4.2. Effect of scan rate on cathodic dissolution

In a cathodic scan, Pt dissolution occurred mostly in parallel with the reduction of Pt oxide and produced Pt^{2+} on a CE set at 1.4 V (**Fig. 2.16**). The dependence of this cathodic dissolution on ν was evaluated by comparing I_{CE} trends at 5, 20, and 200 mV/s (**Fig. 2.16b**). The nature of this reduction-related dissolution is unclear, although electrochemical (Eq. 6) [7] and chemical dissolutions (Eq. 7) [26] have been proposed to explain this phenomenon.

Below 20 mV/s, I_{CE} showed a peak between 1.05 and 0.7 V before reaching a plateau up to 0.3 V (**Fig. 2.16b**). These two features merged at 200 mV/s. The peak may be attributed to Pt^{2+} formed by electrochemical dissolution (Eq. 6) because its potential range corresponded to that of oxide reduction (**Fig. 2.16a**). In this potential region, I_{WE} and I_{CE} increased with increasing ν. In particular, I_{WE}, which represents the rate of oxide reduction (Eqs. 8 and 9), was proportional to ν. For example, at 0.75 V, its value at 200 mV/s was ca. 35 times that measured at 5 mV/s. In contrast, I_{CE} exhibited a weaker dependence on ν than I_{WE}. At 0.75 V, its value at 200 mV/s was ca. 4 times that at 5 mV/s (**Fig. 2.17**).

The plateau may correspond to H_2O_2 produced by the reduction of residual O_2, consistent with previous reports identifying H_2O_2 in a similar potential range during oxygen reduction [30-31]. When ν increases, the cathodic dissolution shifts to lower potentials and overlaps with H_2O_2 generation, producing higher I_{CE} values at 200 mV/s than at 5 or 20 mV/s in the plateau region.

2.4. Conclusions

In this chapter, I discussed the applicability of is situ CFDE for monitoring Pt dissolution of under potential cycling. The following conclusions are highlighted:

1. In an anodic scan, Pt^{2+} dissolution starts near 0.6 V and increases with potential until 0.8 V. From 0.8 V, Pt^{2+} dissolution continues in parallel with $Pt–O_{ad}$ formation until 1.2 V, where one ML of $Pt–O_{ad}$ is formed. From 1.2 V, a place exchange between Pt and O starts. As O penetrates into the Pt lattice, 3-D PtO_2 forms and triggers dissolution of Pt^{4+}, which increases with potential.
2. In a cathodic scan, Pt^{4+} dissolution continues in the cathodic scan from 1.4 to 1.2 V before reduction of PtO_2. During reduction of PtO_2, most is reduced to Pt, whereas a small fraction is reduced to Pt^{2+} and dissolves from the Pt-WE.
3. Dissolution during oxide formation and reduction has different dependence on ν. During oxide formation, ν affects the initiation and inhibition of Pt dissolution. Slow scans induce Pt dissolution earlier, but soon suppress it. The extent of dissolution, however, does not show significant changes like the oxide development does when changing the ν. During oxide reduction, the predominant dissolution occurs, and it depends on ν. Increasing the ν not only enhance the cathodic Pt^{2+} dissolution, but also slightly shifts the dissolution region towards the native direction.

References

1. P.J. Ferreira, G.J. la O', Y. Shao-Horn, D. Morgan, R. Makharia, S. Kocha, H.A. Gasteiger, *J. Electrochem. Soc.*, **152**, A2256 (2005).
2. Y. Shao-Horn, W.C. Sheng, S. Chen, P.J. Ferreira, E.F. Holby, D. Morgan, *Top. Catal.*, **46**, 285 (2007).
3. K. Yasuda, A. Taniguchi, T. Akita, T. Ioroi, Z. Siroma, *Phys. Chem. Chem. Phys.*, **8**, 746 (2006).
4. C.H. Paik, G.S. Saloka, G.W. Graham, *Electrochem. Solid-State Lett.*, **10**, B39 (2007).
5. B. Merzougui, S. Swathirajan, *J. Electrochem. Soc.*, **153**, A2220 (2006).
6. FCCJ Durability Test protocols, 2010.
7. D.C. Johnson, D.T. Napp, S. Bruckenstein, *Electrochim. Acta.*, **15**, 1493 (1970).
8. S. Kawahara, S. Mitsushima, K. Ota, N. Kamiya, *ECS Trans.*, **3**, 625 (2006).
9. S. Mitsushima, S. Kawahara, K. Ota, N. Kamiya, *J. Electrochem. Soc.*, **154**, B153 (2007).
10. S. Kim, J.P. Meyers, *Electrochim. Acta*, **56**, 8387 (2011).
11. T. Tsuru, *Mater. Sci. Eng.*, **A146**, 1-14 (1991).
12. M. Lee, M. Uchida, H. Yano, D.A. Tryk, H. Uchida, M. Watanabe, *Electrochim. Acta*, **55**, 8504 (2010).
13. R.M. Darling, J.P. Meyers, *J. Electrochem. Soc.*, **150,** A1523 (2003).
14. A.P. Yadav, A. Nishikata, T. Tsuru, *J. Electrochem. Soc.*, **156**, C253 (2009).
15. X.P. Wang, R. Kumar, D.J. Myers, *Electrochem. Solid-State Lett.*, **9**, A225 (2006).
16. R.K. Ahluwalia, S. Arisetty, X. Wang, X. Wang, R. Subbaraman, S.C. Ball, S. DeCrane, D.J. Myers, *J. Electrochem. Soc.*, **160**, F447 (2013).

17. B.R. Shrestha, A.P. Yadav, A. Nishikata, T. Tsuru, *Electrochim. Acta.*, **56**, 9714 (2011).

18. Y. Sugawara, T. Okayasu, A.P. Yadav, A. Nishikata, T. Tsuru, *J. Electrochem. Soc.*, **159**, F779 (2012).

19. H. Imai, K. Izumi, M. Matsumoto, Y. Kubo, K. Kato, Y. Imai, *J. Am. Chem. Soc.*, **131**, 6293 (2009).

20. G. Jerkiewicz, G. Vatankhah, J. Lessard, M.P. Soriaga, Y.S. Park, *Electrochim. Acta.*, **49**, 1451 (2004).

21. A. Sun, J. Franc, D.D. Macdonald, *J. Electrochem. Soc.*, **153**, B260 (2006).

22. L. Xing, G. Jerkiewicz, D. Beauchemin, *Analytica Chimica Acta*, **785**, 16 (2013).

23. H. Matsuda, *J. Electroanal. Chem.*, **16**, 153 (1968).

24. C.A. Reiser, L. Bregoli, T.W. Patterson, J.S. Yi, J.D. Yang, M.L. Perry, T.D. Jarvi, *Electrochem. Solid-State Lett.*, **8**, A273 (2005).

25. A.A. Topalov, S. Cherevko, A.R. Zeradjanin, J.C. Meier, I. Katsounaros, K.J.J. Mayrhofer, *Chem. Sci.*, **5**, 631 (2014).

26. L. Xing, M.A. Hossain, M. Tian, D. Beauchemin, K.T. Adjemian, G. Jerkiewicz, *Electrocatalysis*, **5**, 96 (2014).

27. P. Jovanovič, A. Pavlišič, V.S. Šelih, M. Šala, N. Hodnik, M. Bele, S. Hočevar, M. Gaberšček, *ChemCatChem*, **6**, 449 (2014).

28. E.L. Redmond, B.P. Setzler, F.M. Alamgir, T.F. Fuller, *Phys. Chem. Chem. Phys.*, **16**, 5301 (2014).

29. L. R. Merte, F. Behafarid, D. J. Miller, D. Friebel, S. Cho, F. Mbuga, D. Sokaras, R. Alonso-Mori, T. Weng, D. Nordlund, A. Nilsson, B. R. Cuenya, *ACS Catal.*, **2**, 2371 (2012).

30. U.A. Paulus, T.J. Schmidt, H.A. Gasteiger, R.J. Behm, *J. Electroanal. Chem.*, **495**, 134 (2001).

31. V. Stamenkovic, N.M. Markovic, P.N. Ross Jr., *J. Electroanal. Chem.*, **500,** 44 (2001).

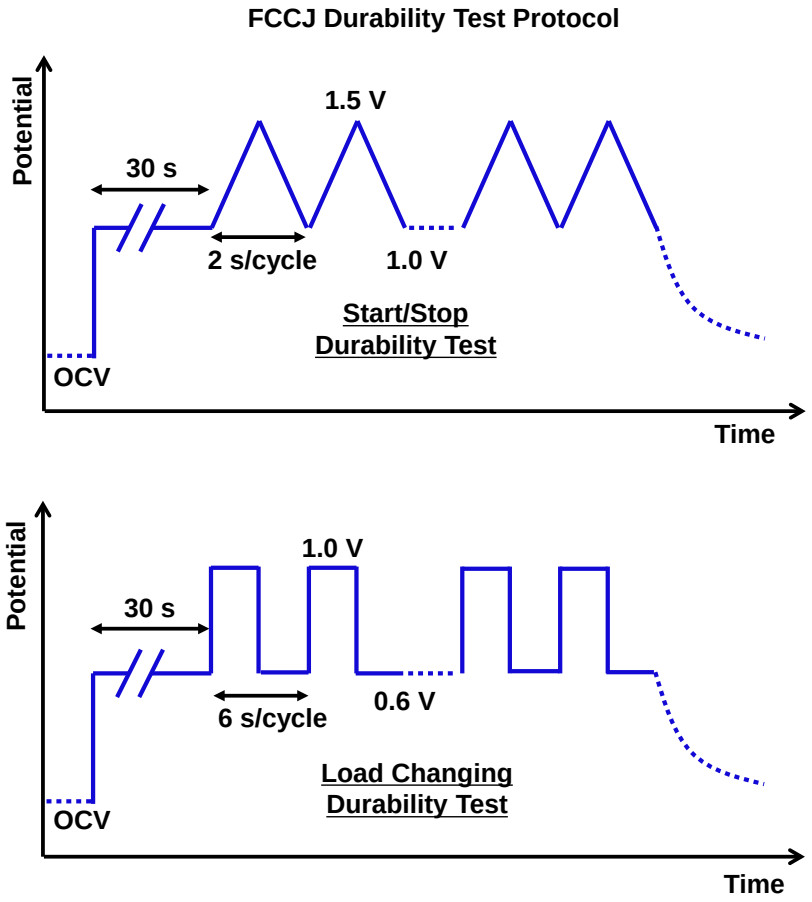

Fig. 2.1. Durability test protocol for PEFC cell recommended by Fuel Cell Commercialization Conference of Japan [3].

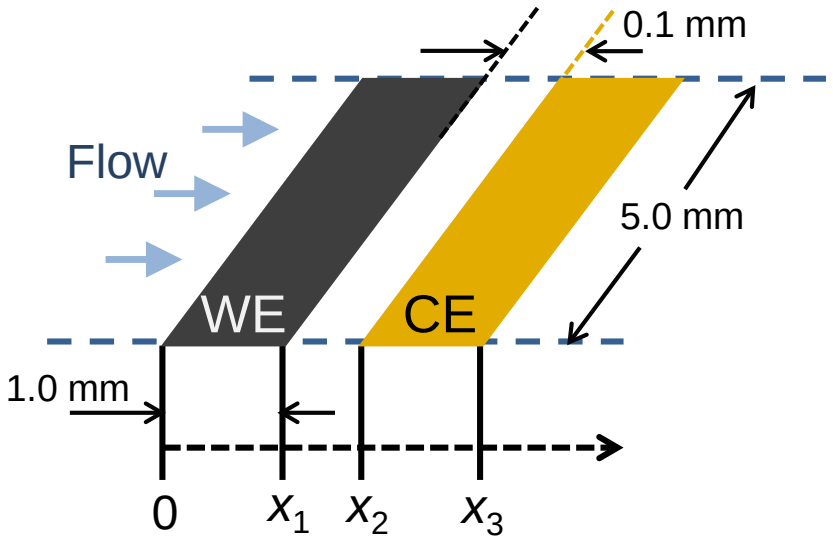

Fig. 2.2. Schematic of electrodes and geometry of WE and CE in CFDE.

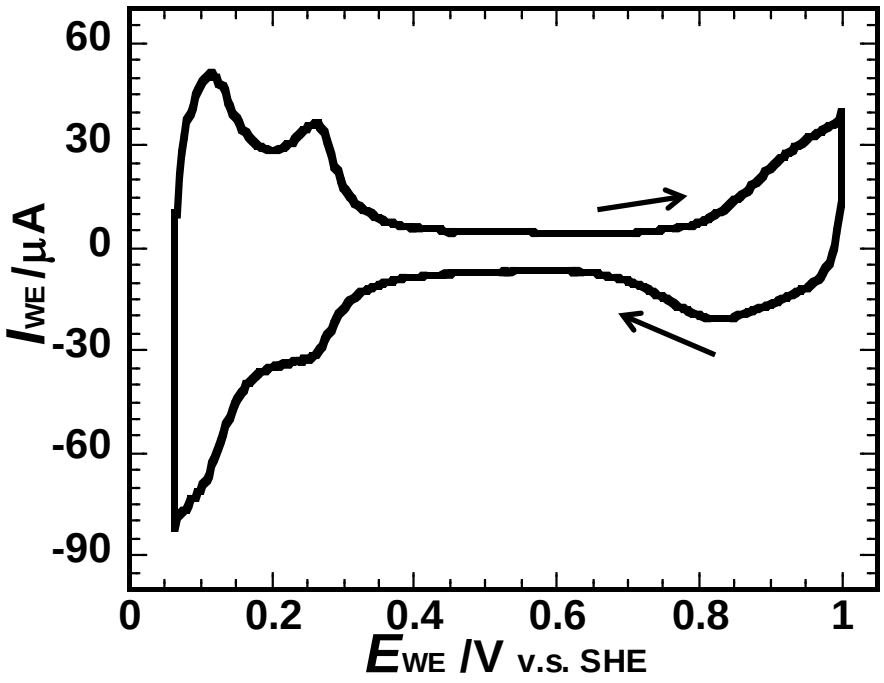

Fig. 2.3. CV of Pt at 20 mV/s in 0.5 M H_2SO_4 measured in CFDE. The solution flow rate was 10 cm/s.

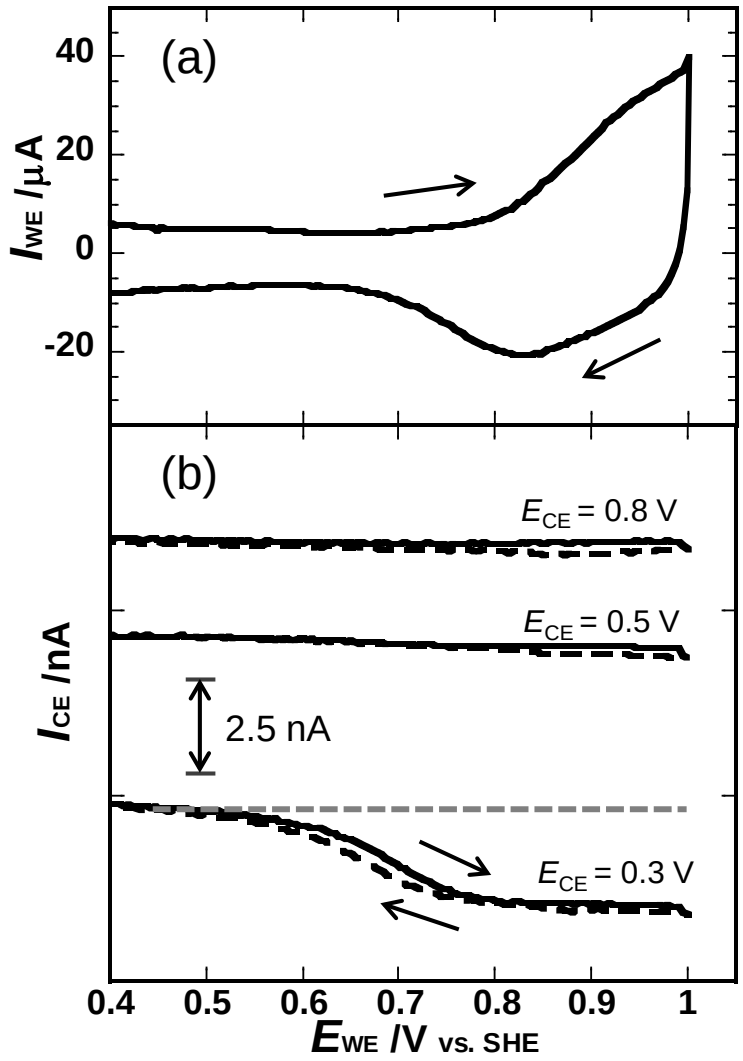

Fig. 2.4. CVs between 0.05 and 1.0 V of the Pt-WE at 20 mV/s (a), and I_C on the GC-CE at 0.3, 0.5, and 0.8 V (b).

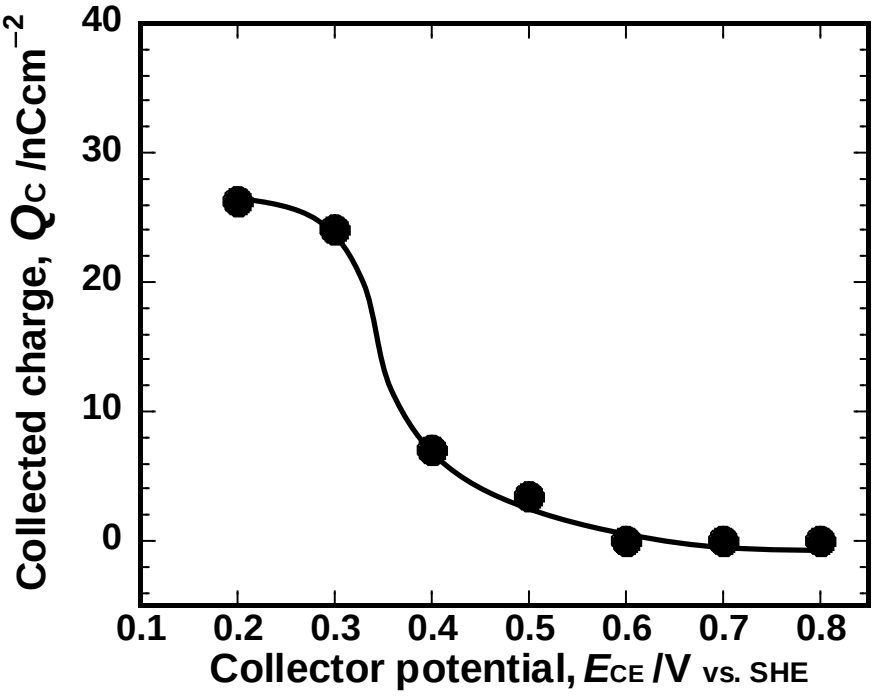

Fig. 2.5. Electric charges collected on the GC-CE set at different collector potentials.

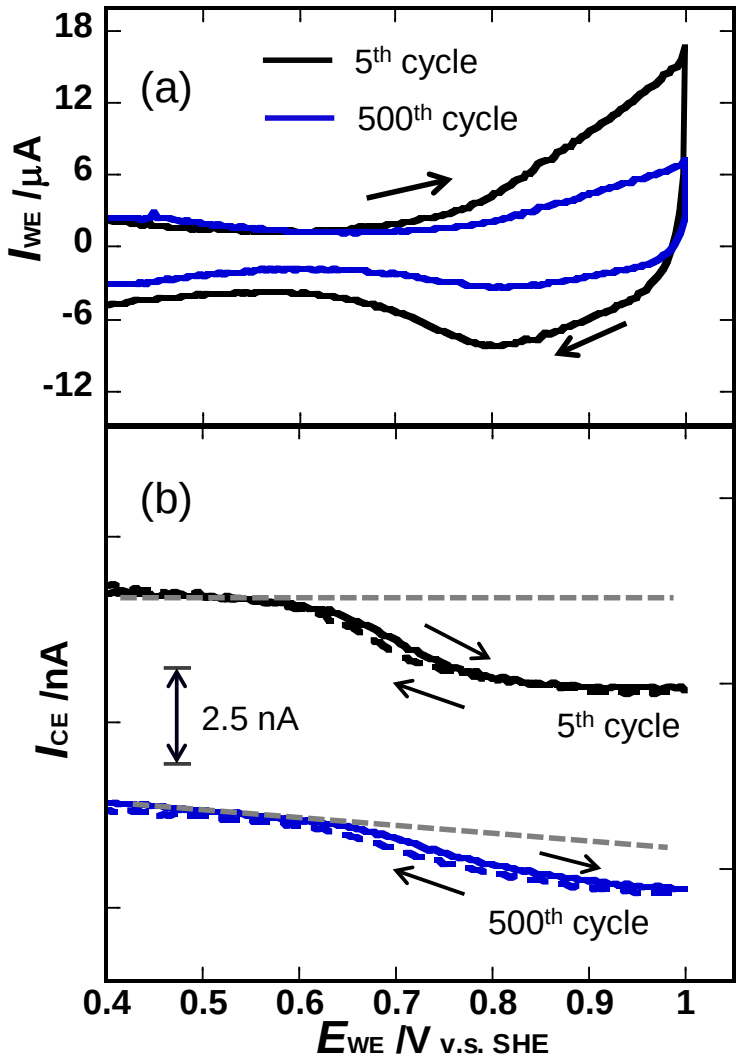

Fig. 2.6. CVs between 0.05 and 1.0 V of the Pt-WE (a), and I_{CE} on the GC-CE at 0.3 V (b). The 5th and 500th cycles in a 3000-cycle test are shown.

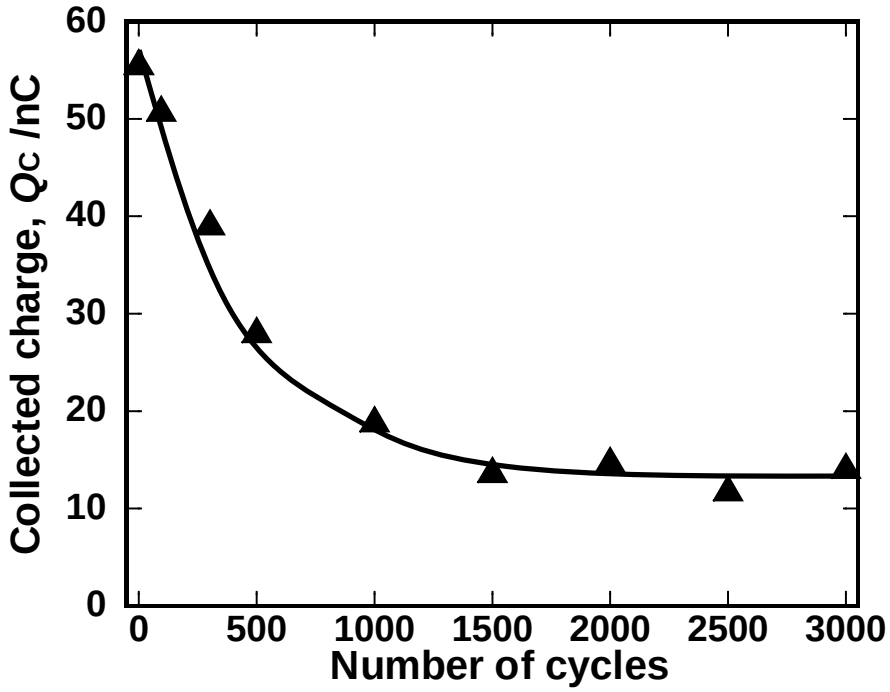

Fig. 2.7. Electric charges collected on the GC-CE in 3000 cycles.

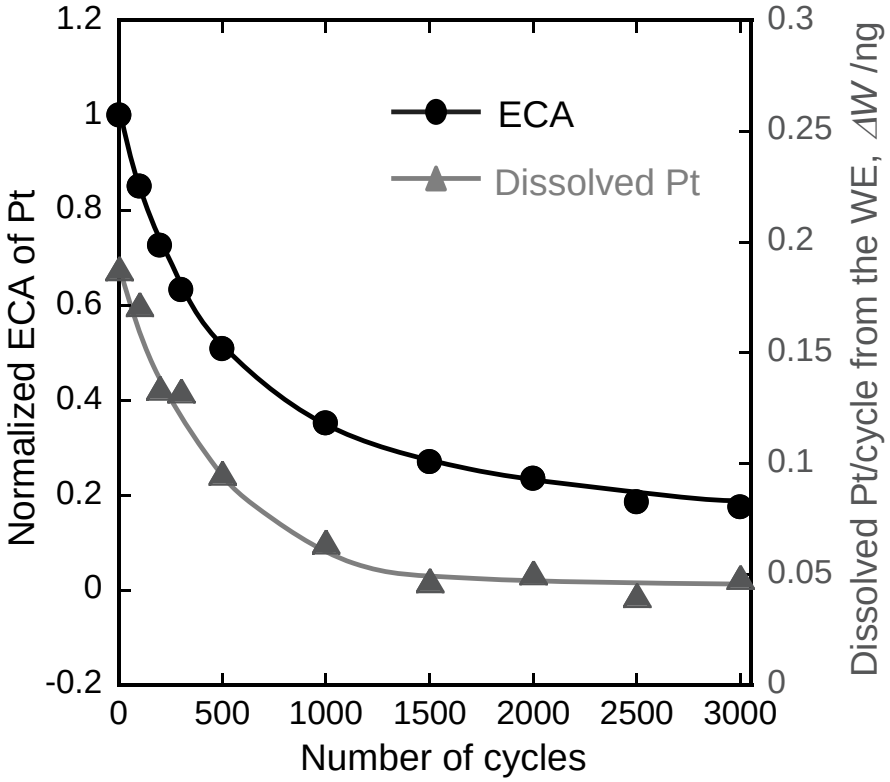

Fig. 2.8. Dissolved Pt from the WE in each cycle and ECA loss of Pt in 3000 cycles of CV from 0.05 to 1.0 V.

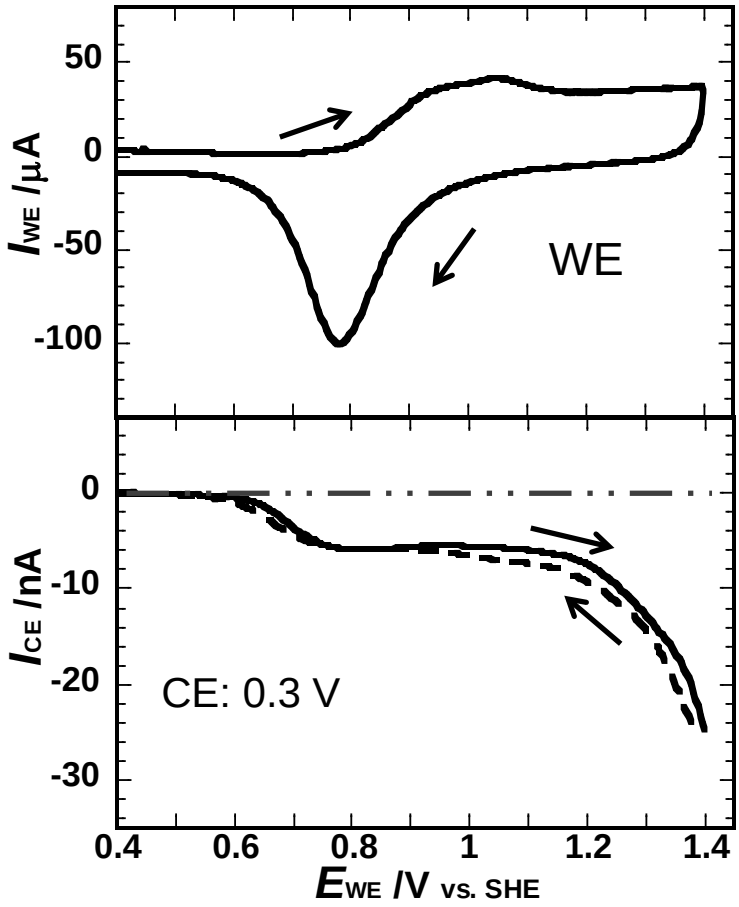

Fig. 2.9. CV between 0.05 and 1.4 V of Pt-WE at 20 mV/s (a), and I_{CE} on the Au-CE at 0.3 V (b).

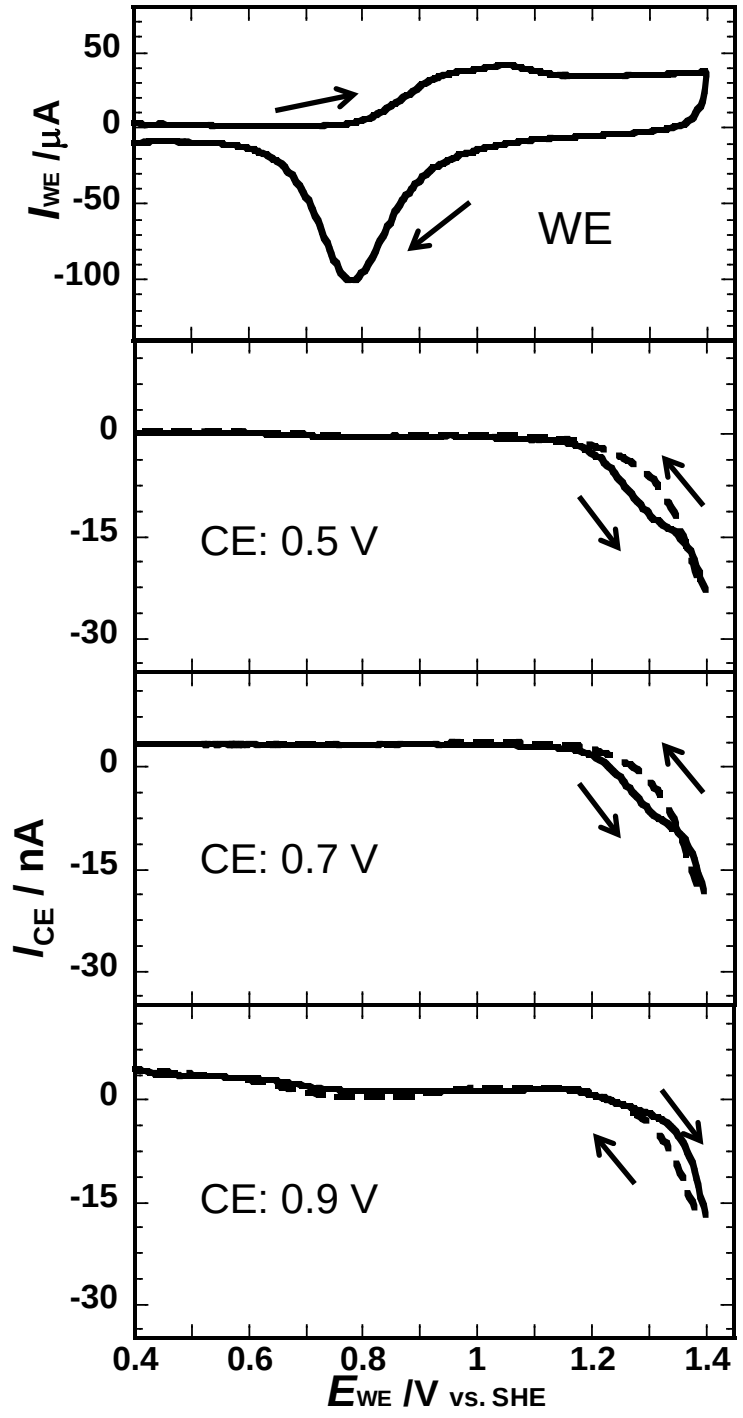

Fig. 2.10. CV between 0.05 and 1.4 V of the Pt-WE at 20 mV/s (a), and I_{CE} on the Au-CE at 0.5, 0.7, and 0.9 V (b).

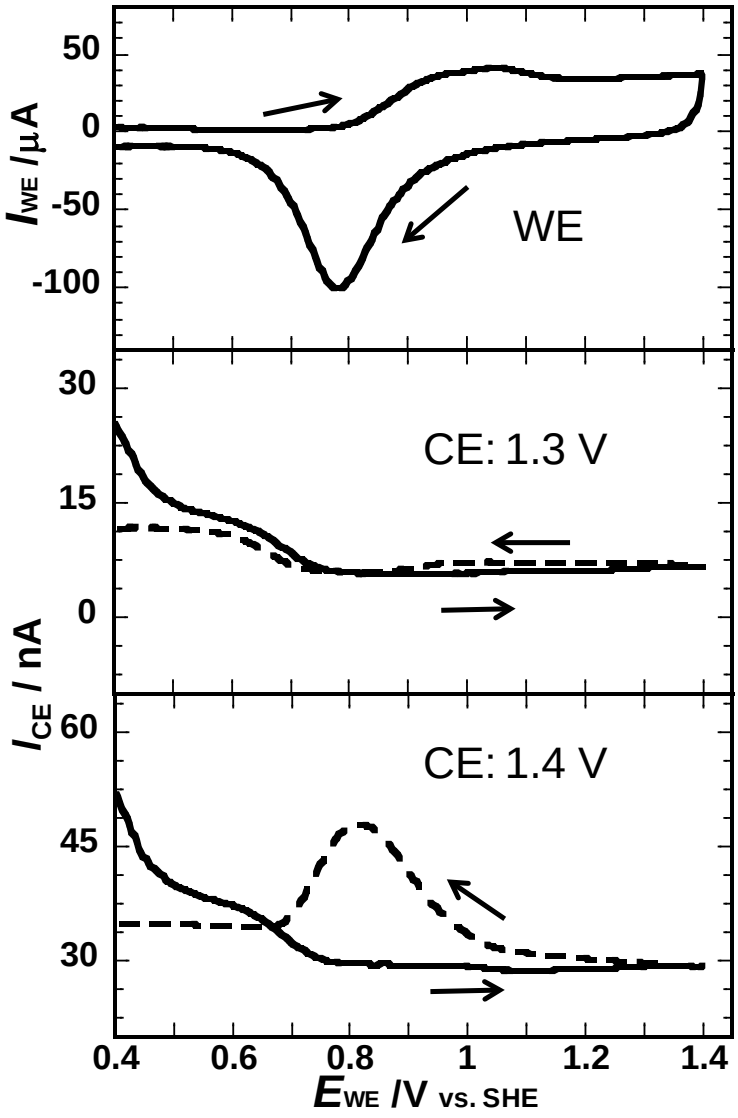

Fig. 2.11. CV between 0.05 and 1.4 V of the Pt-WE at 20 mV/s (a), and I_{CE} on the Au-CE at 1.3 and 1.4 V (b).

Table 2. Dissolved Pt^{2+} and Pt^{4+} per unit ECA of the Pt-WE (ng cm^{-2}) in one cycle of CV.

	Anodic		Cathodic	
	0.6→1.2 V	1.2→1.4 V	1.4→1.2 V	1.2→0.6 V
0.3 V	0.25 (Pt^{2+})	0.12 (Pt^{4+})	0.14 (Pt^{4+})	0.29 (Pt^{2+})
0.7 V	No detection	0.13 (Pt^{4+})	0.11 (Pt^{4+})	No detection
1.4 V	–	No detection	No detection	0.31 (Pt^{2+})

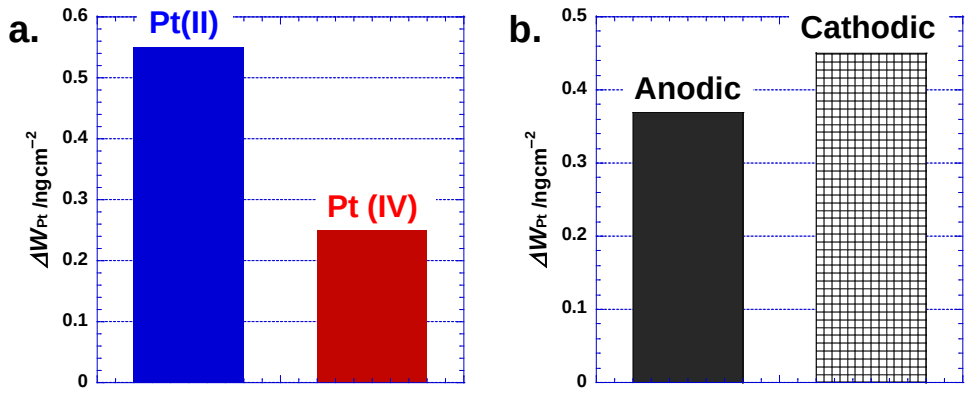

Fig. 2.12. Comparisons of Pt^{2+}/Pt^{4+} (a) and anodic/cathodic (b) dissolutions.

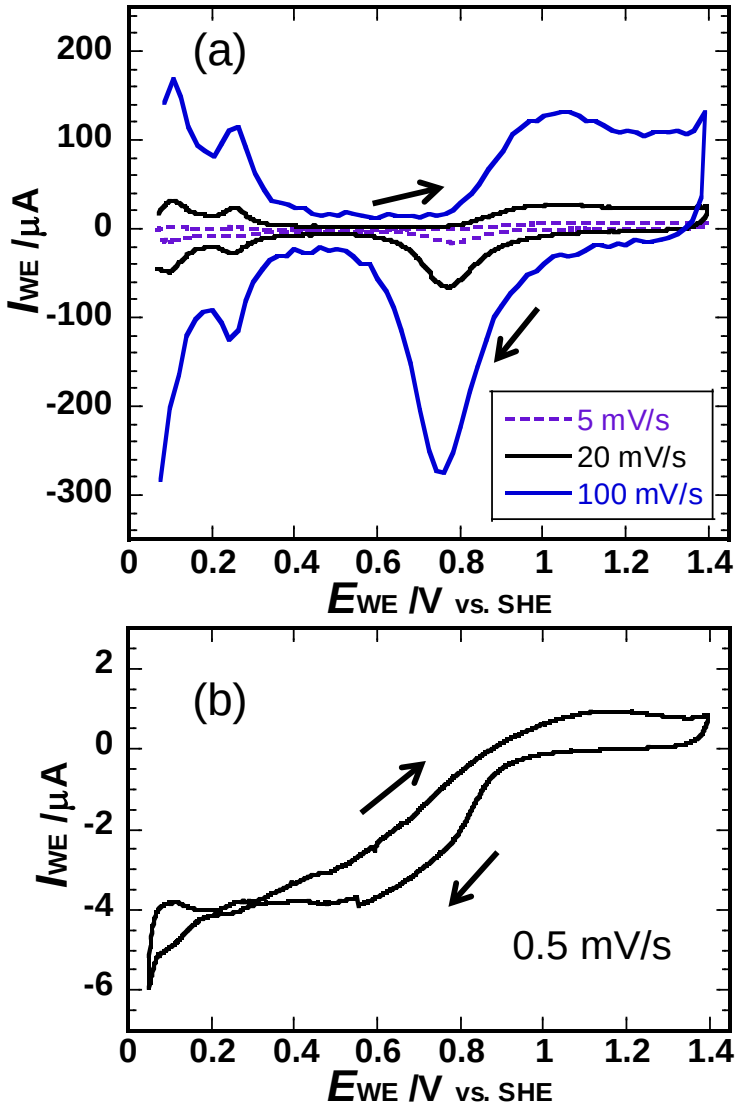

Fig. 2.13. CVs of the Pt-WE recorded at 5, 20, and 100 mV/s (a), and at 0.5 mV/s (b), in 0.5 M H_2SO_4 in a CFDE system.

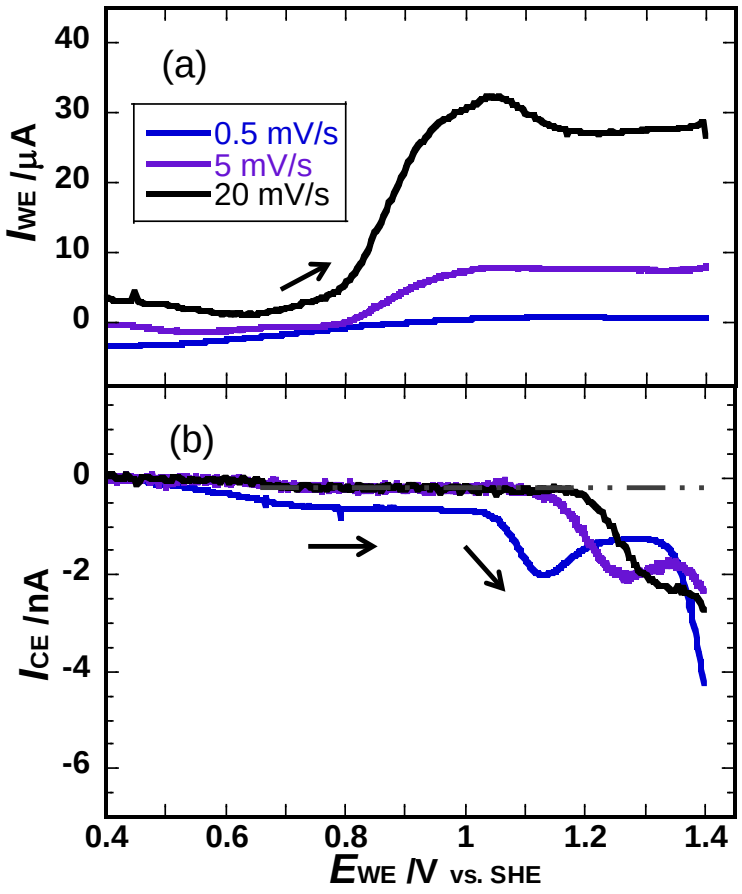

Fig. 2.14. CVs of the Pt-WE in an anodic scan from 0.4 to 1.4 V (a), and the I_{CE} on an Au-CE at 0.7 V for detection of Pt^{4+} (b).

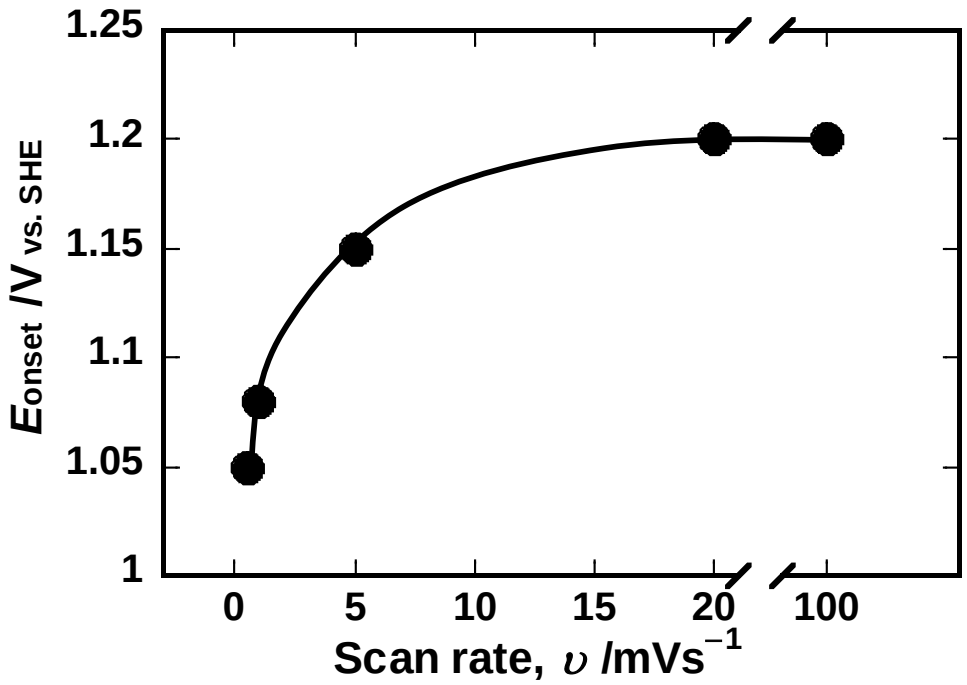

Fig. 2.15. Dependence of the onset potential (E_{onset}) for the anodic Pt^{4+} dissolution on scan rate.

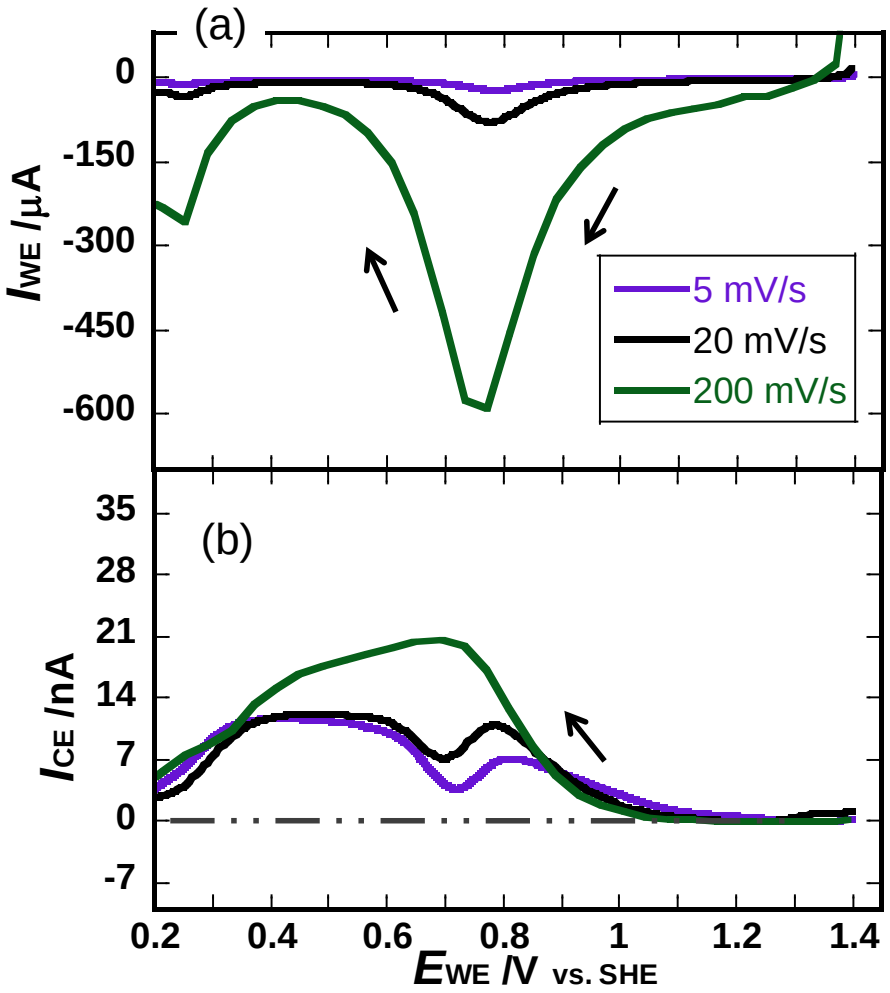

Fig. 2.16. I_{WE} of the Pt-WE in a cathodic scan from 1.4 to 0.2 V (a), the I_{CE} on a Au-CE at 1.4 V for detection of Pt^{2+} (b), and the I_{CE} on a CE at 0.7 V for detection of Pt^{4+} (c).

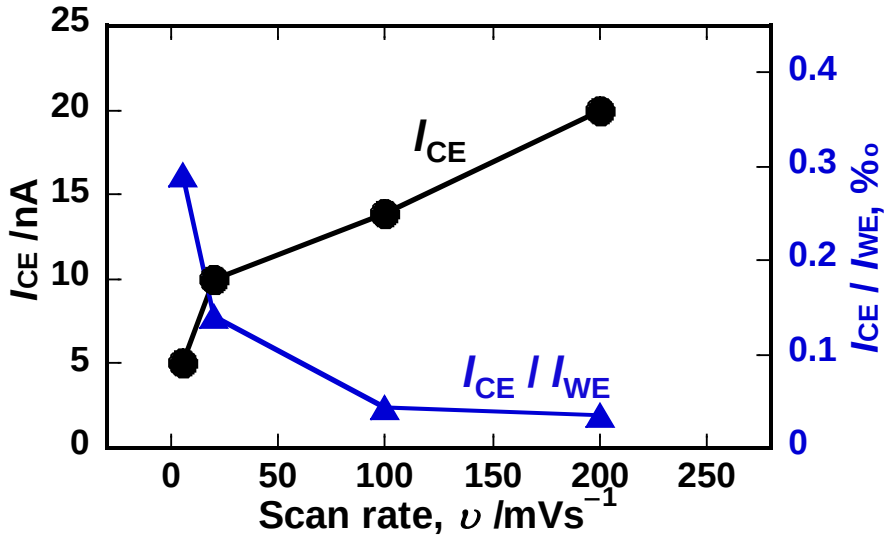

Fig. 2.17. Dependence of the I_{CE} values on the scan rate when E_{WE} was 0.75 V in a cathodic scan. The Au-CE was set at 1.4 V

Chapter 3

Effect of Chloride on Pt Dissolution Studied by a Channel Flow Multi Electrode System

3.1. Introduction

In chapter 2, I discussed the applicability of the in situ CFDE method for tracing Pt dissolution under potential cycling. In this chapter, on the basis of chapter 2, I studies the effect of chloride (Cl^-) on Pt dissolution in the same 0.5 M H_2SO_4 solution at 25 ^oC.

Cl^- is a major fuel cell contaminant [1] that can be introduced into the cell through airborne salts. Moreover, the Pt-based catalysts may also contain a trace of Cl^- that is not completely removed after synthesis using chloride-containing precursors [2]. The Cl^- impurity is detrimental to the performance of proton exchange membrane fuel cells (PEFCs) [3-5]. The presence of Cl^- enhances platinum (Pt) dissolution [6-8], which accelerates the degradation of the Pt/C catalyst [9-11]. In spite of significant evidence of this effect [6-8], the mechanism remains unclear, especially in the potential region in which PEFC cathodes operate (<1.0 V vs. standard hydrogen electrode, SHE). Therefore, investigating the effect of Cl^- on Pt dissolution is important for the development of PEFCs.

Recent data on the effect of Cl^- on Pt dissolution were primarily obtained from electrochemical quartz crystal microbalance (EQCM) measurements [6-8]. Lam *et al.* reported a dramatic loss of ECA under cyclic voltammetry (CV) conditions in presence of 1000 mg/L Cl^- [6]. Yadav *et al.* reported significant mass loss due to Pt dissolution above 1.2 V in a CV anodic scan in the presence of 100 mg/L Cl^- [7]. Below 1.2 V, the adsorption of oxygen (O) and Pt–O formation on the Pt surface resulted in a continuous mass increase; mass loss caused by Pt dissolution could not be distinguished. Under potentiostatic conditions at 1.2 V, Ofstad *et al.* reported enhanced Pt loss in presence of 10 mg/L Cl^- over a 24-hour period [8]. The Pt loss increased with increasing Cl^- concentration. Mitsushima *et al.* also reported increased Pt/PtO solubility in 1.0 M

H_2SO_4 in the presence of Cl^- [12]. Recently, Pavlišič et al reported that Pt dissolution was enhanced by Cl^- in both anodic and cathodic scans [13], using an electrochemical flow cell [14-15]. Dissolution of Pt were quantified by in-situ ICP-MS measurement. Their findings suggested that the dissolution mechanism changes in chloride electrolyte. To investigate the mechanism of Pt dissolution in presence of Cl^-, knowledge of the valences of the dissolved species would be instrumental, as stated by Xing et al [16].

In chapter 1, we established an in situ electrochemical system based on a CFDE and elucidated the nature of Pt dissolution under potential cycling in 0.5 M H_2SO_4 using a Pt thin film electroplated onto a gold substrate. In this system, Pt^{2+} and Pt^{4+} dissolved from the working electrode (WE) upstream of a laminar flow were detected on the downstream collector electrode (CE). The CE was polarized at different potentials for the detection of these species. The amounts of Pt^{2+} and Pt^{4+} dissolved in one CV cycle were quantified using the current responses on the CE (CE currents, I_{CE}).

To now study the effect of Cl^- on Pt dissolution, we added a silver electrode (Ag-E) upstream of the WE to store Cl^-. The Cl^- was later released to contaminate the WE surface. Pt dissolution under Cl^- contamination conditions was detected downstream on the CE. This method of Cl^- storage and release is similar to that of the liquid-phase ion gun used by Fushimi *et al.* for achieving the local breakdown of passive films [17-18]. It avoids the Cl^- contamination of the entire system. Pt dissolution as Pt^{2+} was detected by setting the CE at 1.4 V, the potential at which dissolved Pt^{2+} is oxidized to Pt^{4+}. Pt^{4+} was detected by reducing it to Pt^{2+} on the CE polarized at 0.7 V. In this study, we investigate the effect of Cl^- on Pt dissolution under both potentiostatic and potential cycling conditions and discuss the dissolution mechanism.

3.2. Experimental

Fig. 3.1 shows a schematic of the channel-flow multi-electrode (CFME) system. The WE was a Pt thin film electroplated onto a gold (Au) substrate [19]. The CE was glassy carbon (GC). The theoretical collection number (N) of the double electrode (WE and CE) was calculated to be 0.3 [20] using the geometries shown in **Fig. 3.1**. A solution of 0.5 M H_2SO_4, deaerated with argon gas, was pumped through the system at an average flow rate of 100 mm s^{-1}. The counter electrode was an Au wire, and the reference electrode was a double-junction KCl-saturated Ag/AgCl electrode. All potentials in this study refer to SHE. The WE and CE potentials were measured at 25°C using a multichannel potentiostat (PS-08, TOHO Technical Research, Japan).

For the study of the effect of Cl^- on Pt dissolution, a silver electrode (Ag-E) was placed upstream of the WE (**Fig. 3.1**). Prior to CFDE measurements, silver chloride (AgCl) was galvanostatically deposited on the Ag-E surface at 40 μA for 600 s in a 0.1 M HCl solution (Eq. 3.1) using a stationary three-electrode cell.

$$Ag + Cl^- \rightarrow AgCl + e^- \qquad [3.1]$$

Under potentiostatic conditions, a single potential step was applied to the WE (**Fig. 3.2**). After holding at 0.45 V for 300 s for the removal of oxide on the surface formed by air, the WE was held at a constant potential (E_W) [21]. Once the WE (I_{WE}) and CE (I_{CE}) currents stabilized, Cl^- was released from the Ag-E (Eq. 3.2) by a constant cathodic current (I_{Cl}) for 40 s (**Fig. 3.2**). The polarization of the Ag-E was controlled by another similar potentiostat using a separate counter and reference electrode pair.

$$AgCl + e^- \rightarrow Ag + Cl^- \quad [3.2]$$

Under potential cycling conditions, the WE was cycled from 0.35 to 1.4 V at 20 mV s^{-1} for 10 cycles. Cl^- was released at the end of the fourth cycle by applying an I_{Cl} on the Ag-E at −120 μA for 200 s (Eq. 3.2). The WE in the third cycle was therefore free of Cl^-, and in the fifth cycle, it was under Cl^- contamination. The I_W and I_C of these two cycles were compared. Under both conditions, the CE was set at 1.4 V for the detection of Pt^{2+} (Eq. 3.3) and at 0.7 V for Pt^{4+} (Eq. 3.4), as discussed in Chapter 1.

$$Pt^{2+} \rightarrow Pt^{4+} + 2e^- \quad [3.3]$$

$$Pt^{4+} + 2e^- \rightarrow Pt^{2+} \quad [3.4]$$

3.3. Results and Discussion

3.3.1. Pt dissolution under potentiostatic conditions in the presence of Cl^-

The WE potential was stepped from 0.45 V to nine different potentials (E_{WE}), 0.6, 0.7, 0.8, 0.9, 1.0, 1.1, 1.2, 1.3 and 1.4 V, and the response currents were recorded at a sampling time of 0.2 s. As an example, the transient current on the WE when its potential steps from 0.45 to 1.3 V is shown in **Fig. 3.3**. A relatively stable I_W is obtained after 400 s. The other potentials show the similar trends. The extents of Pt–O coverage on the WE held at the respective potentials for 400 s, before the release of Cl^-, were estimated from the electric charge and are inserted in **Fig. 3.3**. Sugawara *et al*. studied Pt dissolution under potentiostatic conditions in pure 0.5 M H_2SO_4 [19] and reported

that dissolution above 1.2 V in a 24 h test was suppressed by Pt–O formation (Eq. 3.5). Similar trends were reported in a 0.57 M $HClO_4$ solution [22, 23].

$$Pt + H_2O \rightarrow Pt\text{–}O + 2e^- + 2H^+ \quad [3.5]$$

In the presence of Cl^-, Pt dissolution on the WE is enhanced, despite 60% coverage of its surface by Pt–O at 1.3 V. Both Pt^{2+} and Pt^{4+} complexes were detected on the CE during 40 s of Cl^- contamination: the I_{CE} shows responses for both Pt^{2+} by Eq. 3.3 (**Fig. 3.4 (b)**) and Pt^{4+} by Eq. 3.4 (**Fig. 3.4 (c)**). The I_{CE} simultaneously gives dissolution rates of each species on the WE. The dissolution amount of each species can be calculated from the collected charges (Q_C) on the CE by integrating the I_{CE} shadowed areas in **Fig. 3.4**. It can be seen that the dissolution of Pt as Pt^{4+} is much higher than as Pt^{2+} at 1.3 V in the presence of Cl^-.

The enhancement of Pt dissolution by Cl^- is similarly observed when the WE is held at other potentials (0.6–1.4 V). **Fig. 3.5** generalizes the potential dependence of Pt dissolution in the presence of Cl^- under potentiostatic conditions. The dissolution amount was calculated by integrating the charge from the I_{CE} responses after the subtraction of the residual current. Before each measurement, the WE was cycled from 0 to 1.4 V at 100 mV s^{-1} until a reproducible ECA (~ 5.7 cm^2) was obtained. **Fig. 3.5** shows that Cl^- even enhances Pt^{2+} dissolution below 1.0 V. The dissolution rate in this region, although relatively smaller than that above 1.2 V, is significant compared with that in Cl^--free environments [19].

The I_C and I_W responses are related by Eq. 3.6: [20] n_W and n_C are the electron numbers for reactions on the WE and CE, respectively, and N is the collection number.

In this study, n_C is 2 and N is 0.3. Thus, Eq. 3.6 can be converted to Eq. 3.7.

$$N = (\Delta I_{CE}/n_{CE}) / (\Delta I_{WE}/n_{WE}) \quad [3.6]$$

$$\Delta I_{WE} = \Delta I_{CE} * n_{WE} / 0.6 \quad [3.7]$$

The ΔI_{CE} in **Fig. 3.4c**, reducing Pt^{4+} to Pt^{2+}, is around 105 nA. According to Eq. 3.7, the value of ΔI_{WE} should be approximately 700 nA for a direct four-electron dissolution by Eq. 3.8 or 350 nA for a two-electron dissolution by Eq. 3.9. Because a ΔI_{WE} of approximately 500 nA (**Fig. 3.4a**) is obtained, Eq. 8 is unlikely to occur, even in high potential regions. Furthermore, Eq. 3.9 consumes Pt–O, so an anodic I_{WE} response for rebuilding the Pt–O layer would be expected to appear in **Fig. 3.4a** when Cl^- contamination ceases. Instead, the I_{WE} recovers instantly, indicating that the surface Pt–O is relatively stable, even in presence of Cl^-.

$$Pt + 6Cl^- \rightarrow PtCl_6^{2-} + 4e^- \quad [3.8]$$

$$Pt–O + 6Cl^- + 2H^+ \rightarrow PtCl_6^{2-} + H_2O + 2e^- \quad [3.9]$$

The dissolution of Pt as Pt^{4+} may proceed through a two-step anodic dissolution given by Eqs. 3.5 and 3.9 (**Fig. 3.6**). In some regions, Pt–O may be oxidized to $PtCl_6^{2-}$. As $PtCl_6^{2-}$ detaches from the WE, the Pt atom beneath the dissolution site quickly oxidizes to Pt–O (Eq. 3.5), which may later dissolve as $PtCl_6^{2-}$ by reaction with Cl^-. The two-step dissolution process in **Fig. 3.6** is controlled by Eq. 3.9, which ceases below 1.2 V. When the WE is held at 1.1 V, Pt^{4+} dissolution is not detected. The I_{CE} on the CE held at 0.7 V remains constant even when the release rate of Cl^- is doubled (**Fig. 3.7**). In the

I_{CE} plots, a spike (one data point) at the beginning of the Cl^- contamination period is omitted.

Unlike the complex process of Pt^{4+} dissolution, Pt^{2+} dissolution seems to occur simply through Eq. 10. It is affected by the potential and Pt–O coverage on the WE. There is a decrease of Pt^{2+} dissolution from 1.0 to 1.1 V (**Fig. 3.5**), which is probably caused by an increase in Pt–O coverage (inset of **Fig. 3.3**).

$$Pt + 4Cl^- \rightarrow PtCl_4^{2-} + 2e^- \qquad [3.10]$$

Below 1.0 V, O atoms (or OH) may only adsorb on Pt (Eq. 11) [23]; thus, the dissolution of Pt^{2+} decreases on lowering the WE potential.

$$Pt + H_2O \rightarrow 2H^+ + Pt\text{–}O_{ad} + 2e^- \qquad [3.11]$$

The I_C responses in **Fig. 3.8**, indicating the detection of Pt^{2+} on the CE at 1.4 V, decline consistently as the potential on the WE (E_{WE}) decreases from 1.0 to 0.6 V. At 0.6 V, the dissolution rate is almost negligible. Pt^{2+} dissolution (Eq. 10) also increases with Cl^- concentration: the I_{CE} responses in **Fig. 3.9** increase with the I_{Cl} when the WE is held at 0.9 V. The Cl^- concentration near the WE surface, although difficult to quantify, should be proportional to I_{Cl}. Eq. 10 mainly consumes the unstable Pt atoms [19] that may be present at defect sites. A decreasing dissolution rate is therefore observed at high Cl^- concentrations, as the I_{CE} decreases with time. At low Cl^- concentrations, the dissolution rate remains almost constant.

In a PEFC, Cl^- is expected to enhance Pt dissolution more severely than observed

in this study because smaller Pt nanoparticles are more unstable [24, 25]. The fine nanoparticles (< 3 nm) in the supported Pt/C catalyst are easier to dissolve in the presence of Cl^- than the larger particles of this study or bulky Pt plate.

3.3.2. Effect of Cl^- on Pt dissolution under potential cycling

Under potential cycling, Cl^- inhibits the formation of Pt–O but enhances Pt dissolution. **Fig. 3.10** compares CVs of the WE and CE currents (I_{CE}) of the Cl^--free and Cl^--contaminated cycles. The hydrogen adsorption (H_{ad}) and desorption (H_{de}) peaks were affected by Cl^-, and the trend observed in this study was similar to the squeezing effect reported by Zolfaghari *et al* [26].

In the anodic scan, Cl^- delays the onset of Pt–O formation from 0.8 V to about 1.0 V. The competitive adsorption of Cl^- on the Pt surface partially blocks the active sites for Pt–O formation in the potential range from 0.8 to 1.2 V. This blocking and competitive co-adsorption of Cl^- with O on Pt is discussed by Zolfaghari *et al* [26].

The CVs in the range 1.2 to 1.4 V (**Fig. 3.10a**) indicate that later-stage Pt oxide formation, coupled with positional exchange between the O and Pt atoms [27], is immune to the presence of Cl^-. However, Cl^- enhances Pt^{4+} dissolution: the I_{CE} of the Cl^- cycle on a CE set at 0.7 V dramatically increases from 1.2 V, indicating accelerated Pt^{4+} dissolution on the WE. Below 1.2 V, the I_{CE} (**Fig. 3.10b**) remains constant in the Cl^- and Cl^--free cycles (inset). Cl^- does not trigger Pt^{4+} dissolution below 1.2 V under potential cycling conditions.

The Pt^{4+} dissolution above 1.2 V may mainly proceed through Eqs. 3.5 and 3.9, although its influence on the CV curve cannot be distinguished because of the large current difference between I_{WE} and I_{CE}. Chemical dissolution through Eq. 3.12 may also

occur. The oxide growth mechanism on Pt surface under potential cycling seems yet inconclusive. A recent study by Redmond et al. [28] provides insights which may lead to the further understanding of Pt oxide growth. Besides, some reported cathodic dissolution data [29-31] also suggests that PtO_2 might form during potential cycling in a high potential region.

$$PtO_2 + 4H^+ + 6Cl^- \rightarrow PtCl_6^{2-} + 2H_2O \qquad [3.12]$$

In the Cl^- cycle, an I_{CE} anodic peak in **Fig. 3.10c** appears as the WE (E_{WE}) potential is scanned from 1.2 to 1.4 V. This peak corresponds to the disproportionation reaction of Eq. 3.13, which leads to Pt^{2+} dissolution. No such peak is observed in the I_{CE} of the Cl^--free cycle.

$$Pt + PtCl_6^{2-} + 2Cl^- \rightarrow 2PtCl_4^{2-} \qquad [3.13]$$

In the cathodic scan, Pt^{4+} dissolution continues until 1.2 V, as represented by the I_{CE} in **Fig. 3.10b**. From 1.1 V, the cathodic dissolution of Pt^{2+} (Eq. 3.14) during PtO_2 reduction is also accelerated by Cl^- (**Fig. 3.10c**). The anodic peaks (dotted lines in **Fig. 3.10c)** indicate Pt^{2+} dissolution on the WE. Cathodic Pt^{2+} dissolution is much more severe in the presence of Cl^-, although less Pt oxide is formed and then reduced. An study by Breiter et al. also showed the dissolution of a Pt oxide layer from 1.0 to 0.7 V during a cathodic scan in chloride-containing acid solutions [32].

$$PtO_2 + 4H^+ + 4Cl^- + 2e^- \rightarrow PtCl_4^{2-} + 2H_2O \qquad [3.14]$$

The amounts of Pt^{2+} and Pt^{4+} dissolved in the Cl^- and Cl^--free cycles are calculated from the I_{CE} in **Fig. 3.10** and generalized in **Table 3.1**. On average, Cl^- (−120 μA) enhances Pt dissolution by a factor of approximately 20. And in **Fig. 3.11**, dissolution of Pt^{2+} and Pt^{4+} Cl^- complexes and the amount of anodic and cathodic dissolutions were compared.

The expected enhancement of Pt^{2+} dissolution by Cl^- in an anodic scan from 0.6 to 1.2 V cannot be distinguished by the I_{CE} on a CE held at 1.4 V. In a Cl^--free solution, Pt^{2+} dissolution from 0.6 V is quantified by setting the CE at 0.3 V, where Pt^{2+} is reduced to Pt. In repeated experiments, however, Cl^- is found to destabilize the I_{CE} when the CE is set at 0.3 V, making it difficult to precisely detect Pt^{2+} using this method. Because the potentiostatic data prove that Cl^- enhances Pt^{2+} dissolution below 1.0 V (**Fig. 3.5**), we think that, under potential cycling, Pt^{2+} dissolution from 0.6 to 1.2 V may be enhanced by Cl^-.

3.4. Conclusions

The enhancement of Pt dissolution by Cl^- under both potentiostatic and potential cycling conditions is studied. The following conclusions are highlighted from the in situ analysis using a CFME system.

1. Under potentiostatic conditions, Cl^- enhances Pt dissolution by forming $PtCl_4^{2-}$ below 1.0 V and $PtCl_6^{2-}$ above 1.2 V.
2. Under potential cycling, Cl^- accelerates Pt dissolution above 1.2 V by significant formation of both $PtCl_6^{2-}$ and $PtCl_4^{2-}$. The cathodic dissolution of Pt^{2+} during PtO_2 reduction is also enhanced by Cl^-.

References

1. R. Borup, J. Meyers, B. Pivovar, Y. S. Kim, R. Mukundan, N. Garl, D. Myers, M. Wilson, F. Garzon, D. Wood, P. Zelenay, K. More, K. Stroh, T. Zawodzinski, J. Boncella, J. E. McGrath, M. Inaba, K. Miyatake, M. Hori, K. Ota, Z. Ogumi, S. Miyata, A. Nishikata, Z. Siroma, Y. Uchimoto, K. Yasuda, K.-I. Kimijima, and N. Iwashita, *Chem. Rev.*, **107**, 3904 (2007).

2. T.J. Schmidt, U.A. Paulus, H.A. Gasteiger, R.J. Behm, *J. Electroanal. Chem*, **508**, 41 (2001).

3. A. J. Steinbach, C. V. Hamilton Jr., and M. K. Debe, *ECS Trans.*, **11**(1), 889 (2007).

4. K. Matsuoka, S. Sakamoto, K. Nakato, A. Hamada, and Y. Itoh, *J. Power Sources*, **179**, 560 (2008).

5. H. Li, H. Wang, W. Qian, S. Zhang, S. Wessel, T. T. H. Cheng, J. Shen, and S. Wu, *J. Power Sources*, **196**, 6249 (2011).

6. A. Lam, H. Li, S. Zhang, H. Wang, D. P. Wilkinson, S. Wessel, and T. T. H. Cheng, *J. Power Sources*, **205**, 235 (2012).

7. A. P. Yadav, A. Nishikata, and T. Tsuru, *Electrochim. Acta*, **52**, 7444 (2007).

8. A. B. Ofstad, M. S. Thomassen, J. L. Gomez de la Fuente, F. Seland, S. Moller-Holst, and S. Sunde, *J. Electrochem. Soc.*, **157**, B621 (2010).

9. P. J. Ferreira, G. J. la O', Y. Shao-Horn, D. Morgan, R. Makharia, S. Kocha, and H. A. Gasteiger, *J. Electrochem. Soc.*, **152**, A2256 (2005).

10. Y. Shao-Horn, W. C. Sheng, S. Chen, P. J. Ferreira, E. F. Holby, and D. Morgan, *Top. Catal.*, **46**, 285 (2007).

11. B. Merzougui and S. Swathirajan, *J. Electrochem. Soc.*, **153**, A2220 (2006).

12. S. Mitsushima, Y. Koizumi, S. Uzuka, and K.-I. Ota, *Electrochim. Acta*, **54**, 455

(2008).

13. A. Pavlišič, P. Jovanovič, V.S. Šelih, M. Šala, N. Hodnik, S. Hočevar, and M. Gaberšček, *Chem. Commun.*, **50**, 3732 (2014).

14. S. O. Klemm, A. A. Topalov, C. A. Laska and K. J. J. Mayrhofer, *Electrochem. Commun.*, **13**, 1533 (2011).

15. A. A. Topalov, S. Cherevko, A. R. Zeradjanin, J. C. Meier, I. Katsounaros, and K. J. J. Mayrhofer, *Chem. Sci.*, **5**, 631(2014).

16. L. Xing, G. Jerkiewicz, and D. Beauchemin, Analytica Chimica Acta, 785 16 (2013).

17. K. Fushimi, K. Azumi, and M. Seo, *J. Electrochem. Soc.*, **147**(2), 552 (2000).

18. K. Fushimi and M. Seo, *J. Electrochem. Soc.*, **148**(11), B450 (2001).

19. Y. Sugawara, T. Okayasu, A. P. Yadav, A. Nishikata, and T. Tsuru, *J. Electrochem. Soc.*, **159**(11), F779 (2012).

20. H. Matsuda, *J. Electroanal. Chem.*, **16**, 153 (1968).

21. X. P. Wang, R. Kumar, and D. J. Myers, *Electrochem. Solid-State Lett.*, **9**(5), A225 (2006).

22. R. K. Ahluwalia, S. Arisetty, X. P. Wang, X. H. Wang, R. Subbaraman, S. C. Ball, S. DeCrane, and D. J. Myers, *J. Electrochem. Soc.*, **160**, F447 (2013).

23. L. R. Merte, F. Behafarid, D. J. Miller, D. Friebel, S. Cho, F. Mbuga, D. Sokaras, R. Alonso-Mori, T. Weng, D. Nordlund, A. Nilsson, and B. R. Cuenya, *ACS Catal.*, **2**, 2371 (2012).

24. L. Tang, B. Han, K. Persson, C. Friesen, T. He, K. Sieradzki, and G. Ceder, *J. Am. Chem. Soc.*, **132**, 596 (2009).

25. Z. Yang, S. Ball, D. Condit, and M. Gummalla, *J. Electrochem. Soc.*, **158**, B1439

(2011).

26. A. Zolfaghari, B. E. Conway, W. G. Pell, and G. Jerkiewicz, *Electrochim. Acta*, **47**, 1173 (2002).

27. G. Jerkiewicz, G. Vatankhah, J. Lessard, M. P. Soriaga, and Y. S. Park, *Electrochim. Acta*, **49**, 1451 (2004).

28. E.L. Redmond, B.P. Setzler, F.M. Alamgir, and T.F. Fuller, *Phys. Chem. Chem. Phys.*, **16**, 5301 (2014).

29. D. C. Johnson, D. T. Napp, and S. Bruckenstein, *Electrochim. Acta*, **15**, 1493 (1970).

30. S. Kawahara, S. Mitsushima, K. Ota, and N. Kamiya, *ECS Trans.*, **3**(1), 625 (2006).

31. S. Kim and J. P. Meyers, *Electrochim. Acta*, **56**, 8387 (2011).

32. M.W. Breiter and J.L. Weiniger, *J. Electrochem. Soc.*, **12**, 1135 (1962).

33. K. Jayasayee, J.A.R. Van Veen, E.J.M. Hensen, F.A. de Bruijn, *Electrochim. Acta*, **56**, 7235 (2011).

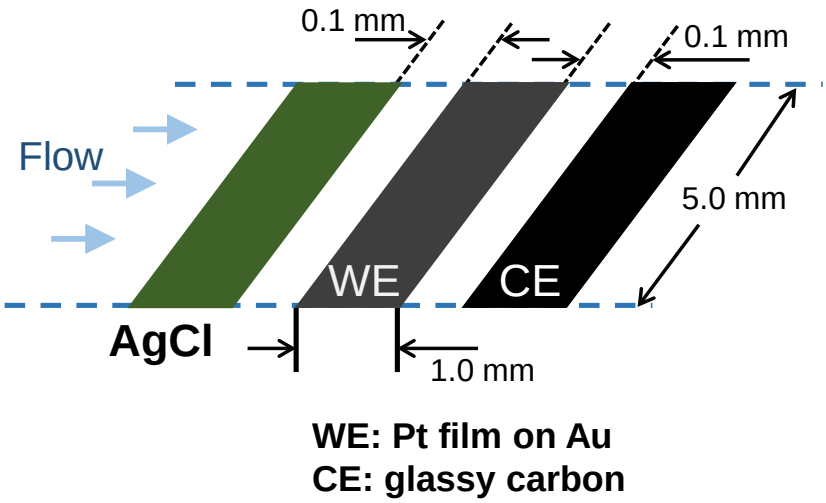

Fig. 3.1. Schematic of a channel flow multi electrode system: a silver electrode (Ag-E), a working electrode (WE), and a collector electrode (CE).

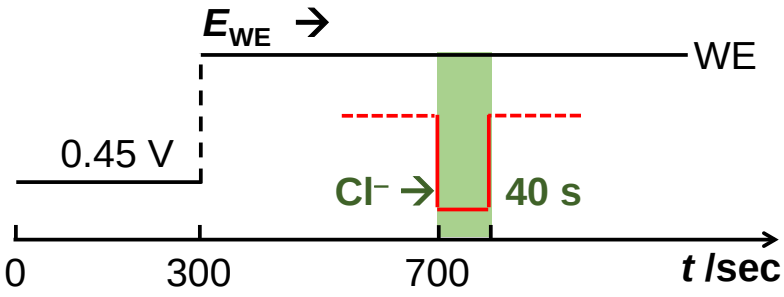

Fig. 3.2. Profile of a single potential step applied on the WE (E_W) and a 40-sec constant cathodic current (I_{Cl}) applied on the Ag-E for release of Cl^-.

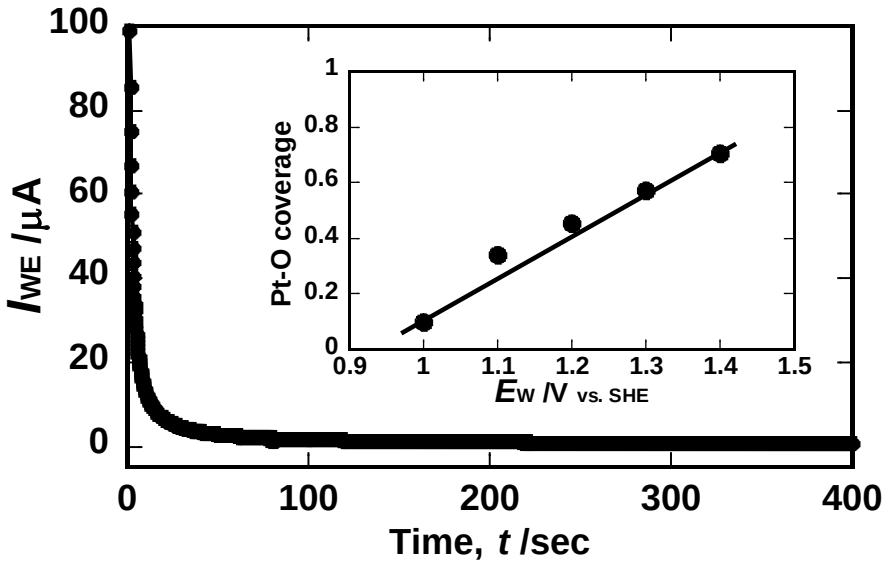

Fig. 3.3. Current transient on the WE when the potential steps from 0.45 V to 1.3 V. The inset is the coverage of Pt-O on the WE after being held at a potential (E_{WE}) for 400 sec.

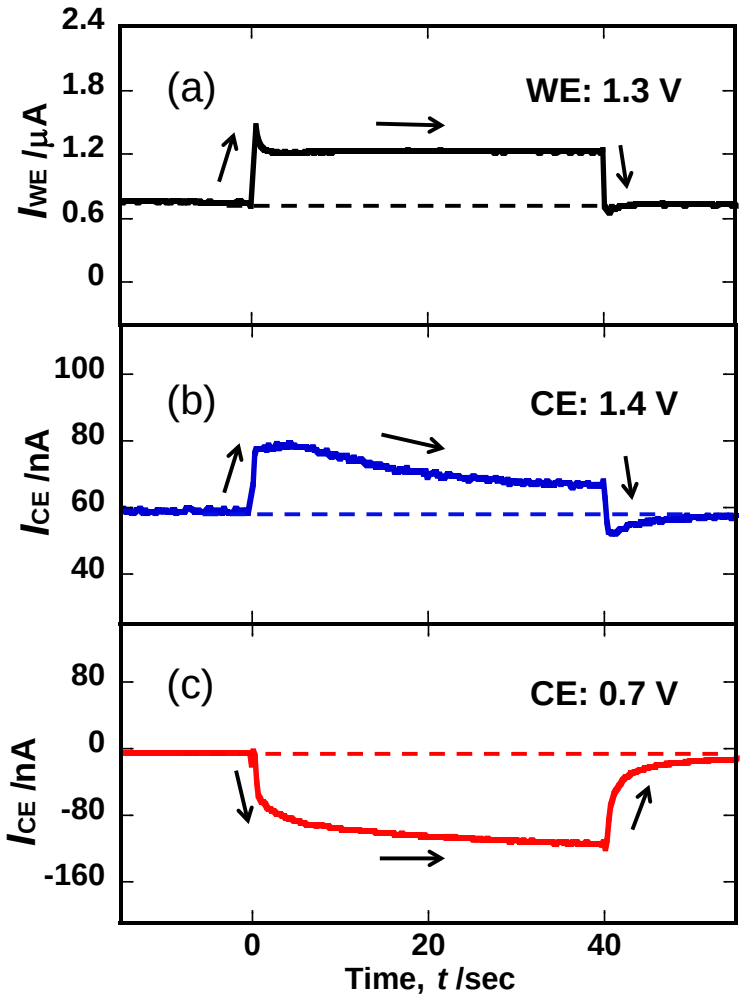

Fig. 3.4. Current responses on the WE (I_{WE}) and the CE (I_{CE}) under Cl^- contamination. The WE is held at 1.3 V (a); the CE is set at 1.4 V for detection of Pt^{2+} (b), and at 0.7 V for Pt^{4+} (c) in separated experiments.

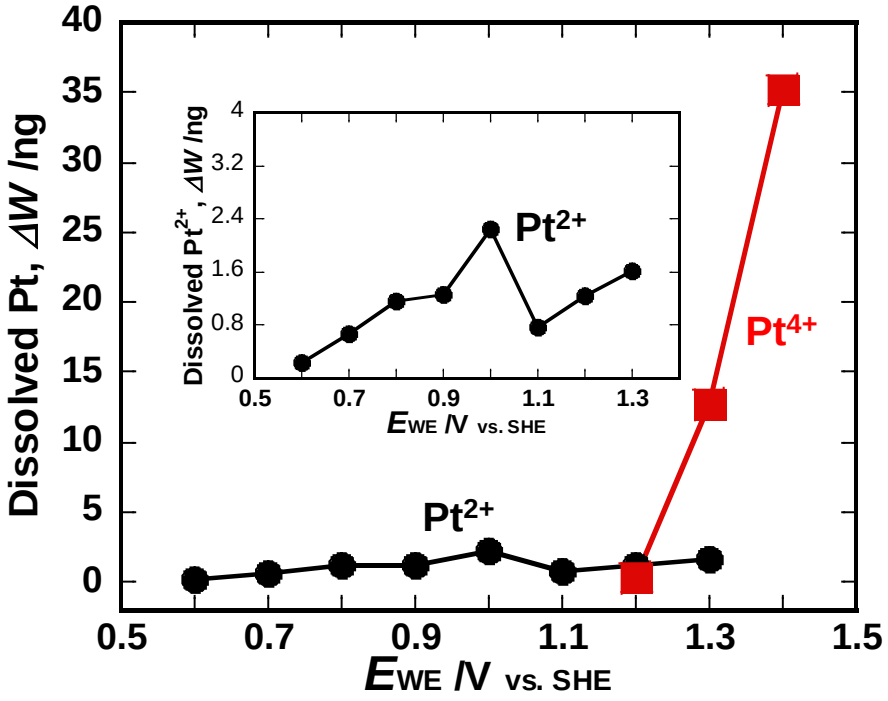

Fig. 3.5. Cl^--enhanced Pt (Pt^{2+} and Pt^{4+}) dissolution with holding potentials. The inset is the plot of dissolved Pt^{2+} on a magnified scale. Cl^- is released by an I_{Cl} of −120 μA for 40 sec.

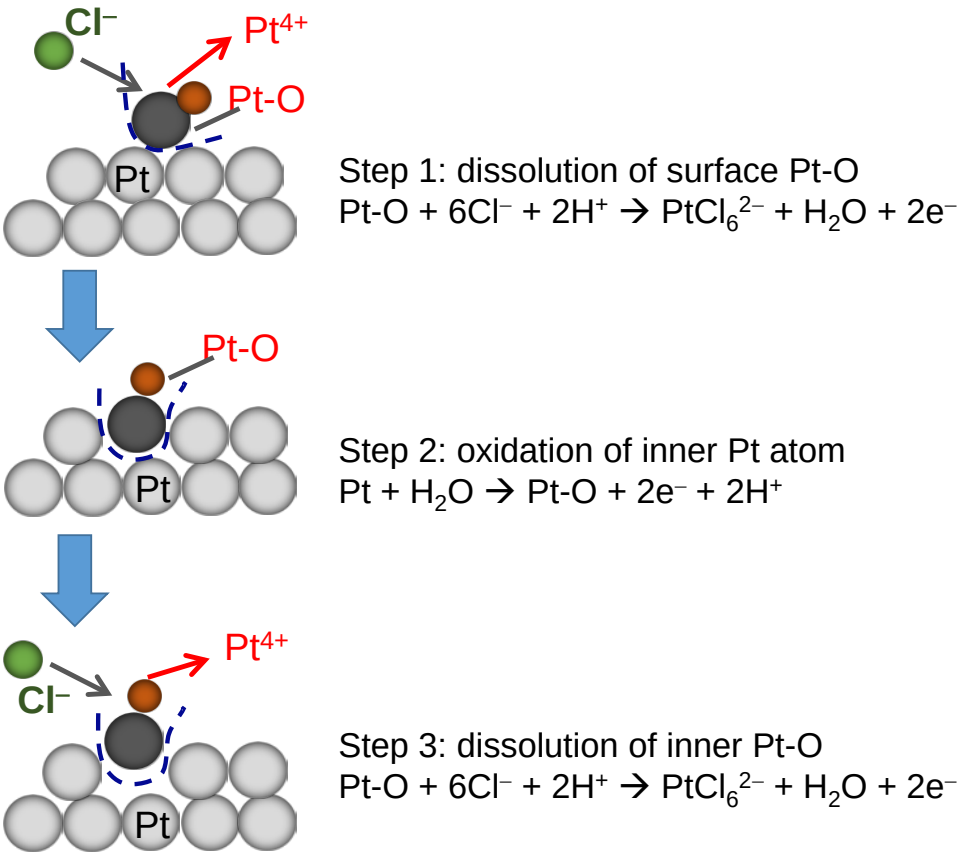

Fig. 3.6. Dissolution mechanism of Pt^{4+} in presence of Cl^- under potential static condition.

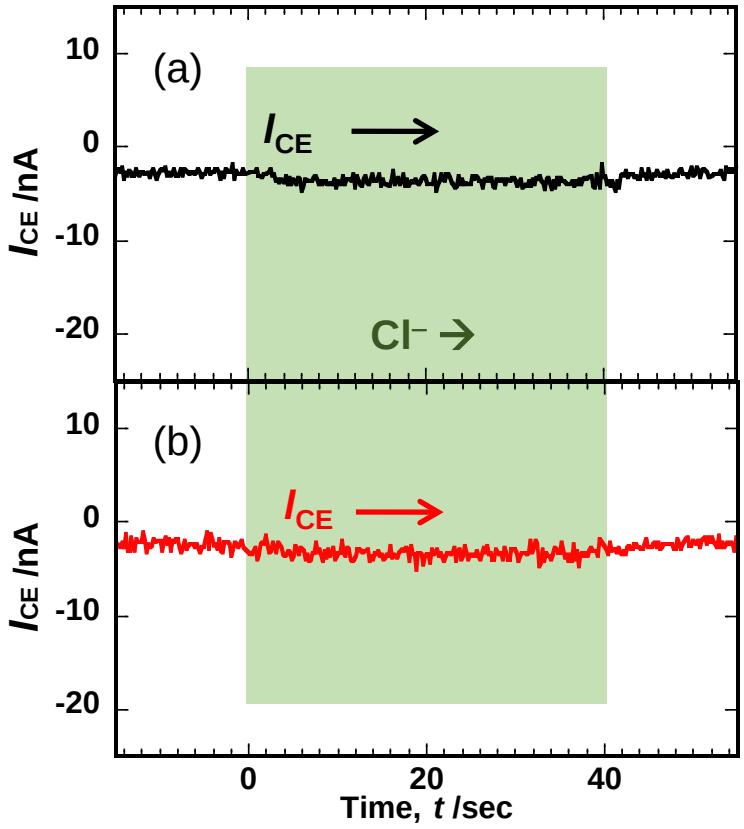

Fig. 3.7. Collector currents (I_{CE}) on the CE set at 0.7 V for detection of Pt^{4+}. WE was held at 1.1 V. I_{Cl} was −120 μA in (a) and −240 μA in (b).

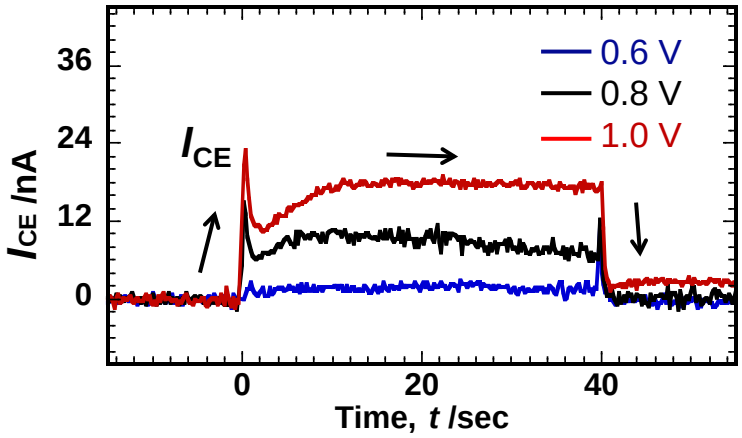

Fig. 3.8. Current responses on the CE (I_{CE}) set at 1.4 V for detection of Pt^{2+} under Cl^- contamination when the WE is held at 0.6 V, 0.8 V, and 1.0 V in separated experiments. I_{Cl} is −120 μA.

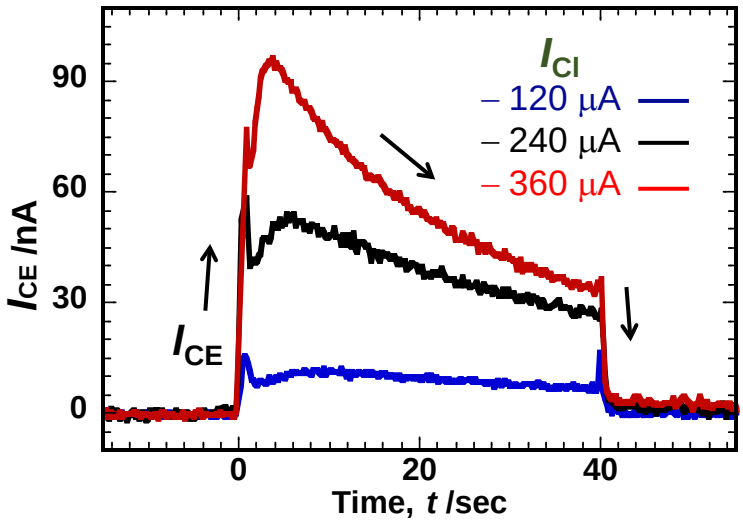

Fig. 3.9. Current responses on the CE (I_{CE}) set at 1.4 V when I_{Cl} was −120, −240, and −360 μA. The WE was held at 0.9 V.

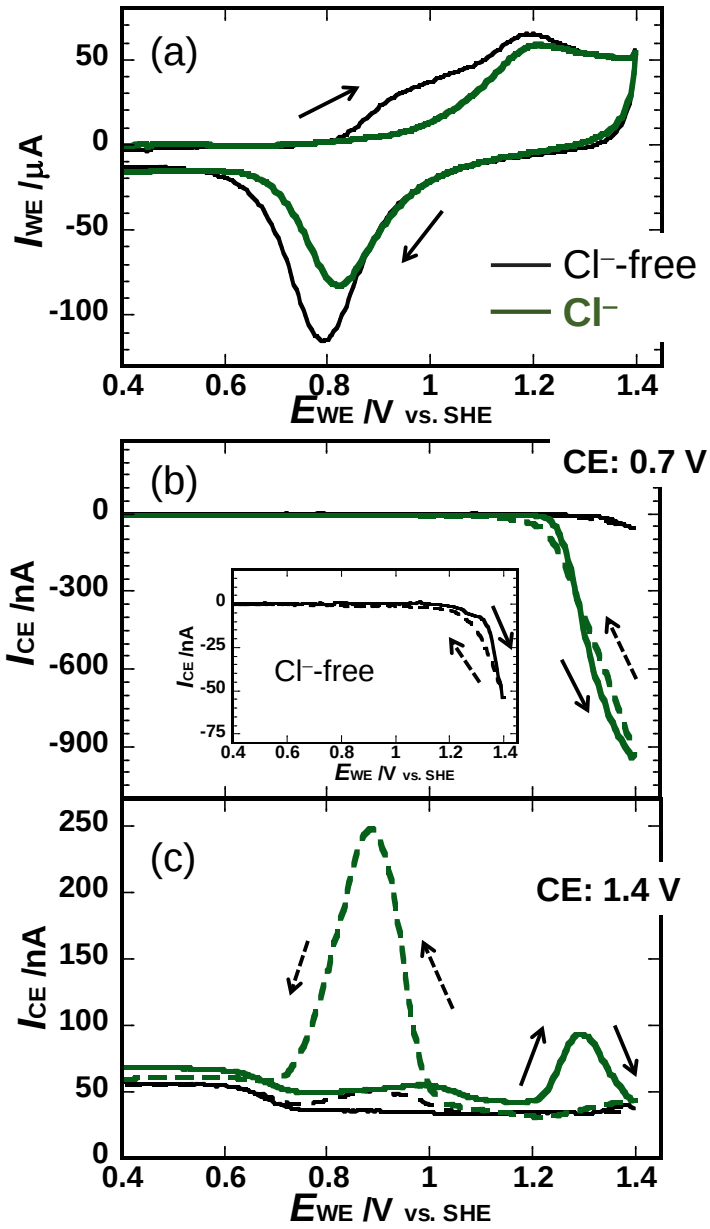

Fig. 3.10. CVs of the WE (a) and current responses on the CE (I_C) measured in Cl^--free and Cl^--contamination cycles. The CE is set at 0.7 V for detection of Pt^{4+} (b) and at 1.4 V for Pt^{2+} (c) in separated experiments.

TABLE 3.1 Mass of Pt (ΔW_{Pt} / **ng cycle^{-1}**) dissolved from the WE in the Cl^--free and Cl^--contaminated cycles under potential cycling between 0.35 and 1.4 V at 20 mV s^{-1}, calculated by I_C and N.

Condition	Mass of platinum dissolved (**ng**)				
	Anodic scan		Cathodic scan		Total
	0.6 to 1.2 V	1.2 to 1.4 V	1.4 to 1.2 V	1.2 to 0.6 V	
Cl^--free	–	0.46	0.67	0.52	**1.65**
Cl^--contaminated	–	15.06	13.55	5.31	**33.92**

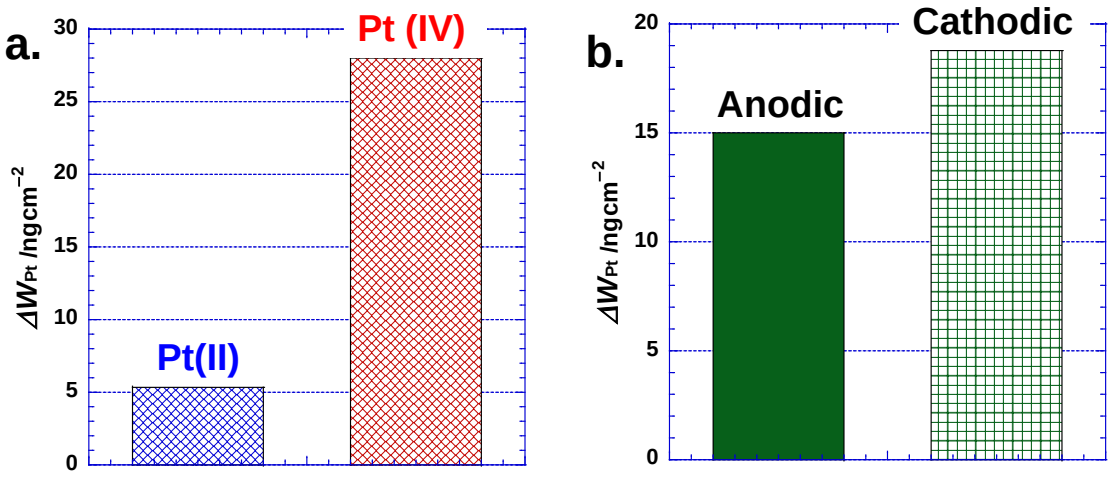

Fig. 3.11. Comparisons of Pt^{2+}/Pt^{4+} and anodic/cathodic Pt dissolutions in Cl^--contaminated 0.5 H_2SO_4 solution.

Chapter 4

Pt Dissolution from PEFC Catalysts

4.1. Introduction

In Chapters II and III, an electroplated Pt sample was used as a model electrode for analyzing Pt dissolution in pure and Cl^--contaminated 0.5 M H_2SO_4 electrolytes. The data obtained from this sample revealed the dissolution behaviors of unsupported Pt under potential dynamic cycles at 25 ^oC. For PEFC, the current fuel cell catalysts are in the form of Pt nanoparticles supported on high surface area carbon (Pt/C). As described in Chapter I, The dissolution of these Pt NPs from the cathode of a PEFC is critical to the durability of the cathode catalyst layer [1-3]. Knowledge of the dissolution mechanism not only helps to better understand the degradation process, but also provides strategic insights for stabilizing the supported nanoparticles. Thus, in this chapter, I tested a commercial fuel cell catalyst, which is produced by Tanaka Kikinzoku Kyogyo (TKK, Japan) and used as a world-standard model catalyst for evaluating properties of new catalysts.

The stability of Pt NPs is important, because pathways to reduce Pt loading is making the Pt NPs smaller. By reducing the size of the Pt NPs, a larger surface could be obtained from the same amount of Pt, as argued by Watanabe et al [4]: an ECSA of 28 m^2/g is obtained from Pt NPs of a mean diameter (d_{Pt}) of 10 nm, while on the 3 nm, the value boosted to 93 m^2/g. However, the durability of smaller Pt NPs is not optimistic. Yang et al. showed that Pt/C with a smaller d_{Pt} exhibited a quicker decay of ECSA over potential cycling [5], similar trend was found by Shao-Horn et al. [6]. Moreover, Tang et al. reported that smaller Pt NPs tended to dissolve at more negative potentials than the bulk materials from their in-situ STM observation [7].

Besides, the experiments in Chapters II and III were conducted at 25 ^oC for the sake of simplicity, and so are the majority of the data in literature [8-10]. And amount them, works by Gaberscek et al. [9] and Myers et al. [10] should be qualified, for their data on

Pt/C provided good comparison to that present in this chapter. To mimic the condition of PEFCs under operation, the temperature needs to be 60 ~ 80 ^{o}C. The degradation of the Pt/C at such temperature was reported much severer than that at room temperature, as examined by post-mortem cell analysis [11-12].

The aim of this Chapter was to know whether the supported Pt NPs could be analyzed in CFDE using the in-situ method described in chapter II, and if possible, the dissolution behaviors of the Pt NPs at 65 ^{o}C.

Out of the purpose, I tested the Pt/Cs in a CFDE under at 65 ^{o}C. In addition, to assess the reliability of the CFDE analysis, I evaluated the amount of Pt dissolution from the Pt/C by ex-situ ICP-MS and compared the data of both methods. The ICP-MS data evaluated the overall amount of Pt dissolution, and the CFDE data provided details of the dissolution behaviors against potential. Using both data, Pt dissolutions from the Pt/Cs was discussed.

4.2. Experimental

4.2.1. Pt/C sample and loading in CFDE

The majority of the experiments in this chapter were conducted on a TKK Pt/C sample with a trade number TEC10E50E. This sample had a Pt loading of 46 wt% and a mean d_{Pt} of 2.2 nm; it was used as a world-standard PEFC catalyst for comparison of ORR activity with other new catalysts. The carbon support in this sample was Ketjenblack EC. The as-received sample were characterized by field-emission transmission electron microscope (FE-TEM) and the image was shown in **Fig. 1a**, together with its particle size distribution (PSD) in **Fig. 1b**. The CFDE operation was same as that in Chapter II, except that the WE substrate was a glassy carbon for loading Pt/C. Besides, the CFDE cell and

solution tank were confined in a thermal chamber set as 65 ^{o}C, while the SSE was separated outside in the ambient environment.

To avoid causing turbulence in the laminar flow of CFDE (**Fig. 1c**), the thickness of the Pt/C layer, difficult to measure, was controlled thin by preparing inks without Nafion. For each sample, I mixed about 10 ~ 15 mg Pt/C with 3.8 ml H_2O and 1.8 ml isopropyl alcohol (IPA), and sonicated the mixture in an ice bath for 1 hour. After obtaining a homogeneous suspension, I loaded 0.6 μl ink on the mirror-polished WE. The geometric surface area of the WE was ca. 0.05 cm^{-2}. The Pt/C-loaded WE was then dried under an ambient atmosphere for 2 hours.

Before dissolution tests, WE was cycled between 0.05 and 1.2 V (vs. SHE) in 0.5 M H_2SO_4 for about 30 times. This pretreatment was an activation that helped to remove organic adsorbents. Then, a reproducible CV shape could be obtained, and from the last cycle an ECSA was calculated. This ECSA, referred as the initial ECSA, was used for normalizing the amount of Pt dissolution.

4.2.2. Polarization of WE and CE in CFDE

The CFDE analysis was to understand the Pt dissolution behavior in a single cycle. The WE underwent potential cycling at 100 mV/s between 0.4 and 1.2 V or 1.4 V for 3 cycles, while the CE (Au) was set at 1.4 V for detecting Pt^{2+} (Eq. 4.1). The data of the 3nd cycle were used. The data recorded on CE when it was held at 0.7 V for detection of Pt^{4+} were premature to be analyzed at this stage due to the complication caused by carbon corrosion in the similar potential region. Nevertheless, more than 80% of Pt species was Pt^{2+} in Cl^{-}-free electrolytes, as reported elsewhere by Beauchemin et al. [13]. The detection of Pt^{2+} should be representative for the whole profile of Pt dissolution.

$$Pt^{2+} \rightarrow Pt^{4+} + 2e^{-} \quad [4.1]$$

4.2.3. Ex-situ ICP-MS analysis

In addition to CFDE analysis, I conducted potential cycling of the Pt/Cs in a stationary cell (SC). An Au wire served as the counter electrode and was placed in a separate cell for avoiding redeposition of Pt onto it. The reference electrode was an Ag/AgCl electrode (SSE) with a double junction. The solution was 0.5 M H_2SO_4 deaerated with argon gas. For each test, I conducted 300 cycles between 0.4 ~ 1.4 V at 100 mV/s. After potential cycling, the testing solution was analyzed by ICP-MS.

4.3. Results and Discussion

4.3.1. In-situ analysis by CFDE

The CV of the WE loaded with TEC10E50E in 0.5 M H_2SO_4 at 65 ^{o}C was shown in **Fig. 4.2**. The CV was taken in CFDE at an average flow rate of 20 cm/s. Typical Pt-related features like H desorption/adsorption and Pt oxidation/reduction were distinguished from the CV, indicating that the Pt/C was stable on the WE without Nafion. The ECSA of Pt was estimated to be 0.86 cm^{-2} by integrating the charge of H adsorption from **Fig. 4.2**.

The current on the WE (I_{WE}) during the potential cycling and that simultaneously recorded on the CE (I_{CE}) were plotted in **Fig. 4.3** against time. The WE experienced three regions: double layer, oxidation and reduction. The I_{CE} showed two peaks representing detection of Pt^{2+}: peak I in the anodic scan and peak II in the cathodic scan. An exact value of base current for the I_{CE} was difficult to determine; the value in the double layer region (0.4 to 0.8 V), which usually serves as the base current, was decreasing along with potential

on the WE. Nonetheless, from the amplitude of the two peaks, we can qualitatively see that peak II was much larger than peak I. In the following two subsections, the behaviors of these two dissolutions against potential are discussed.

4.3.1.1. Anodic dissolution

For analyzing the dissolution behaviors upon potential, the I_{WE} and I_{CE} in the anodic scan were plotted against E_{WE} in **Fig. 4.4**. On the WE, the anodic current I_{WE} (**Fig. 4.4a**) indicated oxidation H_2O on the Pt surface (Eq. 4.2) followed by formation of Pt oxide (Eqs. 4.3 and 4.4). The transformation from Pt-O_{ad} to Pt oxide proceeded along with a place exchange process [14] that usually occurred near 1.1 V. Yet, the composition and structure of the Pt oxide is unclear so far, a mixture of PtO and PtO_2 it is only reported as [15, 16].

$$Pt + H_2O \rightarrow Pt\text{-}O_{ad} + 2H^+ + 2e^- \quad [4.2]$$

$$Pt + H_2O \rightarrow PtO + 2H^+ + 2e^- \quad [4.3]$$

$$PtO + H_2O \rightarrow PtO_2 + 2H^+ + 2e^- \quad [4.4]$$

On the CE (**Fig. 4.4b**), the I_{CE} increased from 0.85 V to 1.1 V and decreased afterwards. This result suggest that initiation of anodic dissolution from Pt/C took place near 0.85 V and the dissolution increased along with potential from 0.85 to 1.1 V. The decrease of the I_{CE} from 1.1 V suggested that the dissolution was inhibited regardless of the increase of the potential. This inhibition of anodic dissolution was probably due to block of Pt site by adsorbed O atoms or the coverage of Pt oxide. By integrating the I_{CE} against time, we can calculated that 70 pg Pt was dissolved from unit ECSA during the anodic scan. The I_{CE} value at 0.85 V was used as the base current.

4.3.1.2. Cathodic dissolution

In the cathodic scan, similarly**,** I_{WE} and I_{CE} against E_{WE} were plotted in **Fig. 4.5**. On the WE (**Fig. 4.4a**), reduction peak covered the wide potential range from 1.1 to 0.4 V. The reduction of Pt oxide may be though Eqs. 4.5 and 4.6.

$$PtO + 2H^+ + 2e^- \rightarrow Pt + H_2O \quad [4.5]$$

$$PtO_2 + 4H^+ + 4e^- \rightarrow Pt + 2H_2O \quad [4.6]$$

$$PtO_2 + 4H^+ + 2e^- \rightarrow Pt^{2+} + 2H_2O \quad [4.7]$$

$$Pt\text{-}O + 2H^+ \rightarrow Pt^{2+} + H_2O \quad [4.8]$$

On the CE (**Fig. 4.5b**), the I_{CE} showed that the cathodic dissolution took place from 1.1 to 0.65 V. The maximum dissolution rate occurred at around 0.9 V. By integrating the I_{CE} against time, the amount of cathodic dissolution was calculated to be 570 **pgcm^{-2}**. The value at 1.1 V was used as the base current. As generalized in **Table 4.1**, the cathodic dissolution is 8 times higher than the anodic one.

For explanation of the cathodic dissolution, Johnson et al. proposed a hypothesis that the cathodic dissolution was Pt^{2+} produced from reduction of PtO_2 through Eq. 4.7 [17]. The upper potential limit in their work was ca. 1.45 V. To attribute the cathodic dissolution in **Fig. 4.5b** to Eq. 4.7 is still premature, since evidence of PtO_2 formation in necessary. Reported recently by Redmond et al., formation of PtO_2 within 1.2 V_{RHE} was possible, and the PtO_2 was converted from early oxide like PtO or PtOH [15].

In an additional experiment, the same WE was held at 1.2 V for 30 mins after a jump from 0.4 V. Such extended polarization resulted thicker Pt oxide layer. As shown in **Fig.**

4.6, both the reduction peak and dissolution peak were enlarged. The amount of cathodic dissolution increased to 2000 **pgcm^{-2}** (**Table 4.1**).

Moreover, both reduction peak and dissolution peak shifted to negative potential. However, for each case, the dissolution proceeded in the early stage of the reduction. However, the equilibrium potentials for Eqs. 4.5 and 4.6 and suggest that the reduction of PtO should took place prior to that of PtO_2. This finding urges re-examination on the oxidation and reduction processes of Pt in aqueous electrolytes. Besides, the repeated formation and reduction of oxide on the Pt was also critical to the d_{Pt} evolution over potential cycles as suggested by Myers et al. [18].

Table 4.1. Cathodic Pt dissolution and reduction charge (pgcm^{-2}cycle^{-1})

	anodic	cathodic	q_{OX} (μCcm^{-2})
CV	70	570	280
30min @ 1.2 V	–	2000	430

4.3.2. Effect of temperature

To check the effect of temperature on Pt dissolution, I tested the Pt/C in CFDE at 25 ^{o}C and compared the data with that at 65 ^{o}C. The upper potential limit was increased to 1.4 V to mimic the start/stop condition in a PEFC. The CVs at both temperatures were shown in **Fig. 4.6**. It can be seen that both oxidation and reduction current densities at 65 ^{o}C were larger than those at 25 ^{o}C. As a result, Pt dissolution at 65 ^{o}C was much severer than that at 25 ^{o}C, as indicated by the I_{CE} in **Fig. 4.7**. At 65 ^{o}C, two discernable peaks I and II were observed for anodic and cathodic dissolution, while at 25 ^{o}C, both peaks shrank, especially the peak I which was only discernable on magnified scale. This result confirmed that both anodic and cathodic dissolutions were affected by temperature. The findings here agreed

with the result reported by Inzelt et al. using electrochemical quartz crystal microbalance (EQCM) [19].

4.3.3. Comparison between samples

In addition to TEC10E50E, I also tested another sample with a trade number TEC10E30A and a 29 wt% Pt loading. **Fig. 4.9** showed the TEM image of this sample and compared its PSD with that of the TEC10E50E. The d_{Pt} for both samples located within 1 to 4 nm, except/excluding the presence of some agglomerate. Specifically, particles smaller than 2 nm in TEC10E30A was more abundant than in TEC10E50E. The average inter-particle distance in TEC10E30A, though difficult to measure the exact value, was also larger than that in TEC10E50E. The ECSA of Pt for the TEC10E30A loaded WE was 0.41 cm, about 1/2 of that for TEC10E50E, since similar volume of ink was used. The difference of Pt-to-C ratio also resulted a little discrepancy in the oxidation and reduction currents, as shown in **Fig. 4.10**.

The I_{CE} for both sample were plotted in **Fig. 4.11**. For both samples under an upper potential of 1.4 V, anodic and cathodic dissolutions were observed, and the cathodic dissolution were much larger that the anodic one. The anodic dissolutions of the two samples were on a similar level, and the cathodic dissolution on the TEC10E30A was severer. By integrating the I_{CE} against time, the amount of dissolution of each sample was calculated; the values were generalized in **Table 4.2** together with the data obtained at 25 ^{o}C from both Pt/C samples and that from a polycrystalline Pt plate at 65 ^{o}C. The values were normalized by ESCA of Pt for comparison.

At 65 ^{o}C, the anodic dissolution (0.4 to 1.4 V) on TEC10E50E was about twice as that from TEC10E30A, while its cathodic dissolution was only 1/3 of that from TEC10E30A.

Totally, Pt dissolution from TEC10E30A was about 2.5 folds of that on the TEC10E50E. From this result, inter-particle distance had no influence on Pt dissolution. On the same Pt/C sample, dissolution at 65 ^{o}C is much 5 times of that at 25 ^{o}C. Interestingly, dissolution on a Pt plate was in between the two Pt/C samples. The bulk sample showed a much weaker anodic dissolution but a similar-level cathodic dissolution comparing to the supported nano-particles.

To assess the reliability of the calculations by I_{CE}, I also evaluated the overall amount of Pt dissolution by ICP-MS at both 25 and 65 ^{o}C. After 300 cycles, Pt dissolution from the Pt/Cs were confirmed by ICP-MS. The amount of dissolved Pt were normalized by the initial ECSAs were also generalized in **Table 4.2**. For example, at 65 ^{o}C, an average value of 1250 pg/cycle was estimated on the TEC10E50E sample by ICP-MS analysis, while the amount of Pt^{2+} dissolution from CFDE detection was ca. 2500 pg/cycle. Considering the decay of ECSA during the 300 cycles, the value 1250 pg/cycle was underestimated. As illustrated in **Fig. 4.12**, the Pt dissolution boosted from 25 to 65 ^{o}C. And the bulk Pt showed a severer cathodic dissolution than the TEC10E50E. The CVs in **Fig. 4.13** showed the shrinkage of the Pt oxidation/reduction peaks at 65 ^{o}C. Thus, the CFDE data relatively fitted with the ICP-MS data; analysis by the CFDE was reliable in a sense. In **Fig. 4.13**, besides the decay of redox peaks, a peak near 0.6 V appeared on the CV of the 300th cycle. This peak indicated the formation of hydroquinone/quinone (HQ/Q) redox peaks, as shown by Speder et al. in a recent study [20], which related to carbon oxidation.

4.4. Conclusions

In this chapter, I evaluated Pt dissolution from commercial Pt/Cs under potential cycling. On Pt/Cs, the cathodic dissolution dominated at an E_U of 1.2 and 1.4 V, and

enhancement of both anodic and cathodic dissolution of Pt^{2+} by increasing temperature was confirmed. The data in this chapter showed that the CFDE is applicable to dissolution tests using supported nanoparticles. Thus, the in situ CFDE is expected to be used for testing other new developed PEFC catalysts.

References

1. P.J. Ferreira, G.J. la O', Y. Shao-Horn, D. Morgan, R. Makharia, S. Kocha, and H. A. Gasteiger, *J. Electrochem. Soc.*, **152**, A2256 (2005).
2. J.C. Meier, C. Galeano, I. Katsounaros, A.A. Topalov, A. Kostka, F. Schuth, and K.J.J. Mayrhofer, *ACS Catal.*, **2** 832 (2012).
3. Y. Park, K. Kakinuma, M. Uchida, H. Uchida, and M. Watanabe, *Electrochim. Acta*, **123**, 84 (2014).
4. M. Watanabe, *Development of advanced materials for the next generation FCVs*, IFCW2015.
5. Z. Yang, S. Ball, D. Condit, and M. Gummalla, *J. Electrochem. Soc.*, **158**, B1439 (2011).
6. W. Sheng, S. Chen, E. Vescovo, and Y. Shao-Horn, *J. Electrochem. Soc.*, **159**, B96 (2012).
7. L. Tang, B. Han, K. Persson, C. Friesen, T. He, K. Sieradzki, and G. Ceder, *J. Am. Chem. Soc.*, **132** 596 (2010).
8. A.A. Topalov, S. Cherevko, A.R. Zeradjanin, J.C. Meier, I. Katsounaros, and K.J.J. Mayrhofer, *Chem. Sci.*, **5**, 631 (2014).
9. P. Jovanovič, A. Pavlišič, V.S. Šelih, M. Šala, N. Hodnik, M. Bele, S. Hočevar, and M. Gaberšček, *ChemCatChem*, **6**, 449 (2014).
10. R.K. Ahluwalia, S. Arisetty, X.P. Wang, X.H. Wang, R. Subbaraman, S.C. Ball, S. DeCrane, and D.J. Myers, *J. Electrochem. Soc.*, **160**, F447 (2013).
11. W. Bi and T.F. Fuller, *J. Electrochem. Soc.*, **155**, B215 (2008).
12. S.R. Dhanushkodi, S. Kundu, M.W. Fowler, and M.D. Pritzker, *J. Power Sources*, **245** 1035 (2014).

13. L. Xing, G. Jerkiewicz, and D. Beauchemin, *Analytica Chimica Acta*, **785**, 16 (2013).
14. G. Jerkiewicz, G. Vatankhah, J. Lessard, M.P. Soriaga, Y. Park, *Electrochim. Acta*, **49**, 1451 (2004).
15. L. R. Merte, F. Behafarid, D. J. Miller, D. Friebel, S. Cho, F. Mbuga, D. Sokaras, R. Alonso-Mori, T. Weng, D. Nordlund, A. Nilsson, and B. R. Cuenya, *ACS Catal.*, **2** 2371 (2012).
16. E.L. Redmond, B.P. Setzler, F.M. Alamgir, and T.F. Fuller, *Phys. Chem. Chem. Phys.*, **16** 5301 (2014).
17. D.C. Johnson, D.T. Napp, and S. Bruckenstein, *Electrochim. Acta*, **15**, 1493 (1970).
18. J.A. Gilbert, N.N. Kariuki, R. Subbaraman, A.J. Kropf, M.C. Smith, E.F. Holby, D. Morgan, and D.J. Myers, *J. Am. Chem. Soc.*, **134** 14823 (2012).
19. G. Inzelt, B. Berkes, and A. Kriston, *Electrochim. Acta*, **55**, 4742 (2010).
20. J. Speder, A. Zana, I. Spanos, J.J.K. Kirkensgaard, K. Mortensen, and M. Arenz, *Electrochem. Comm.*, **34** 153 (2013).

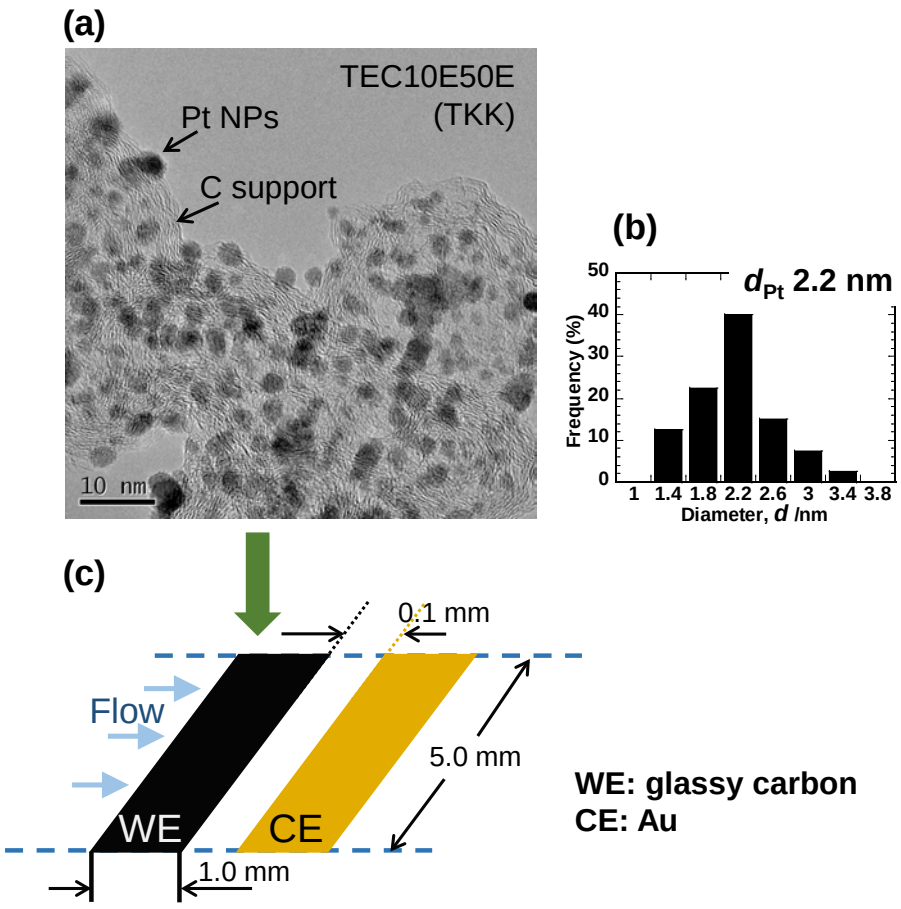

Fig. 4.1. TEM image of an as-received TEC10E50E Pt/C sample from TKK (a), Pt particle size (d_{Pt}) distribution (b), and schematic of a CFDE (c).

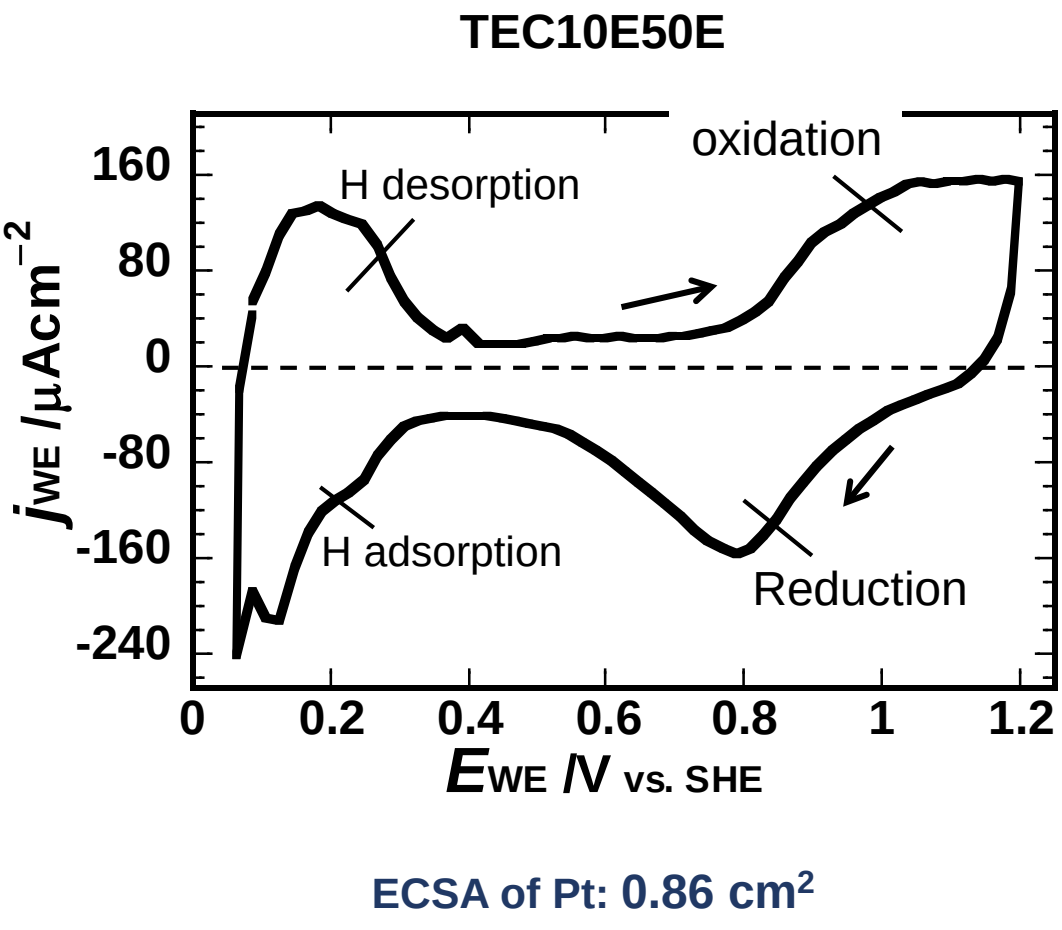

Fig. 4.2. CV of the Pt/C-loaded WE in 0.5 M H_2SO_4 at 65 ^oC in a CFDE. The scan rate was 100 mV/s.

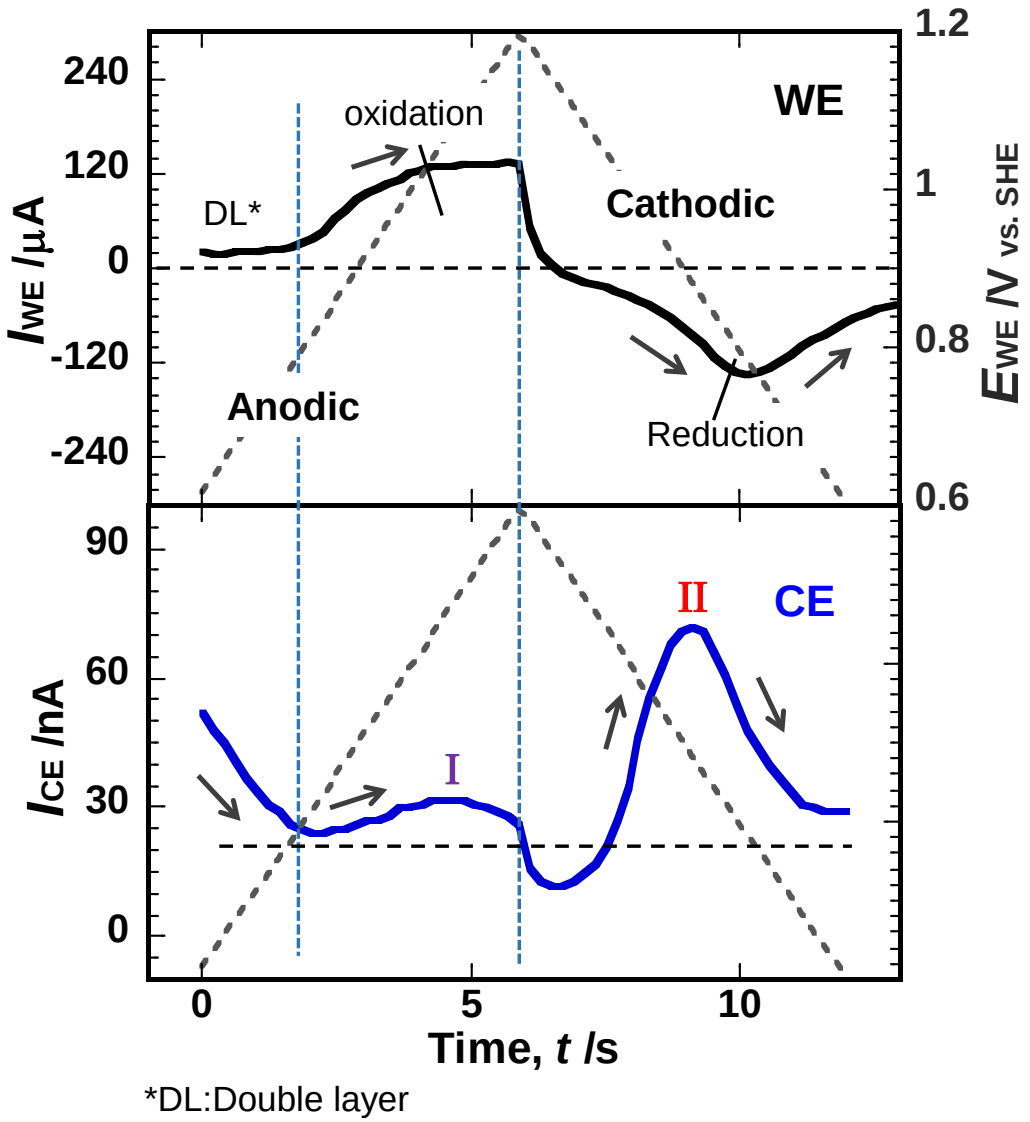

Fig. 4.3. The I_{WE} plotted against time and I_{CE} recorded on a CE set at 1.4 V. The WE (loaded with TEC10E50E) underwent CV @ 100 mV/s from 0.4 and 1.2 V 65 ºC.

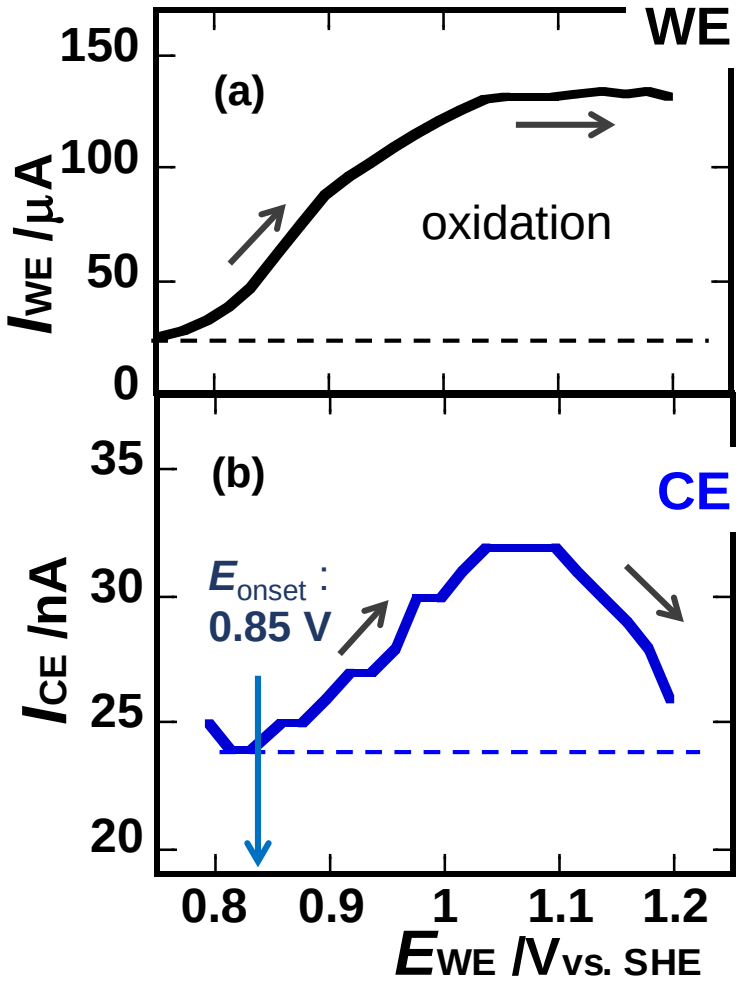

Fig. 4.4. I_{WE} plotted against E_{WE} during an anodic scan (a), and the I_{CE} on the CE (b). The temperature was 65 ^{o}C.

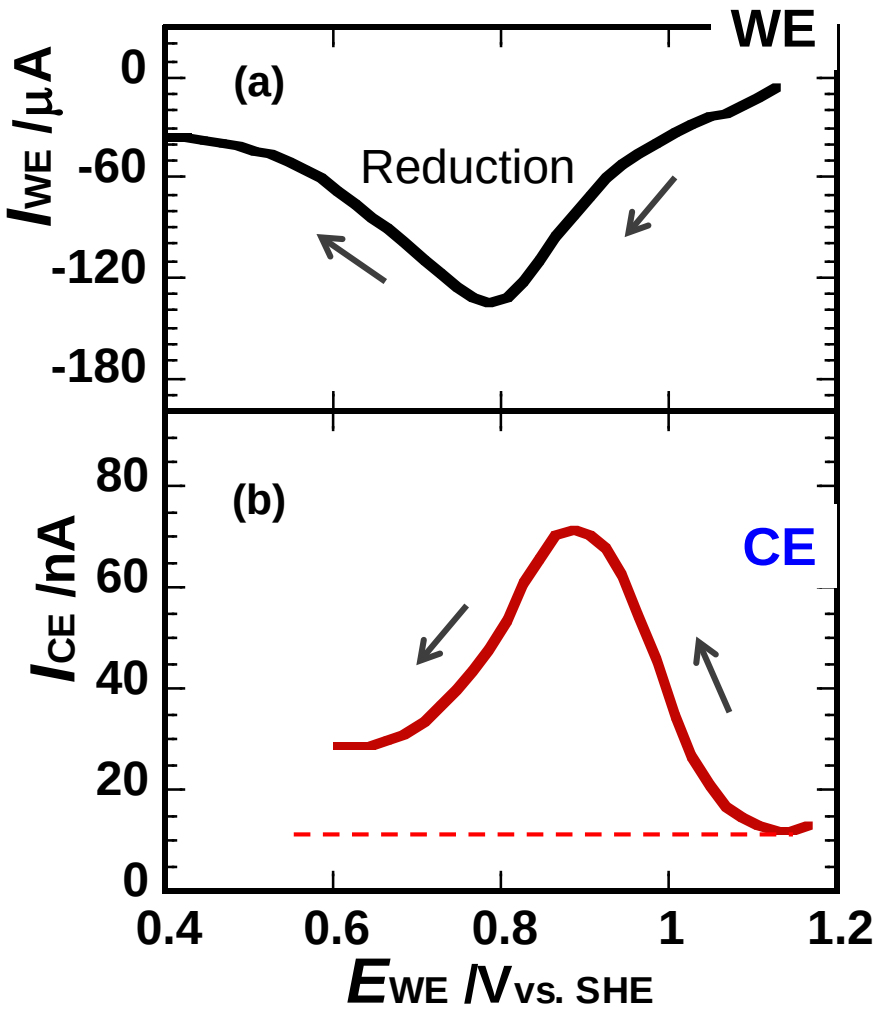

Fig. 4.5. I_{WE} plotted against E_{WE} during a cathodic scan (a), and the I_{CE} on the CE (b). The temperature was 65 °C.

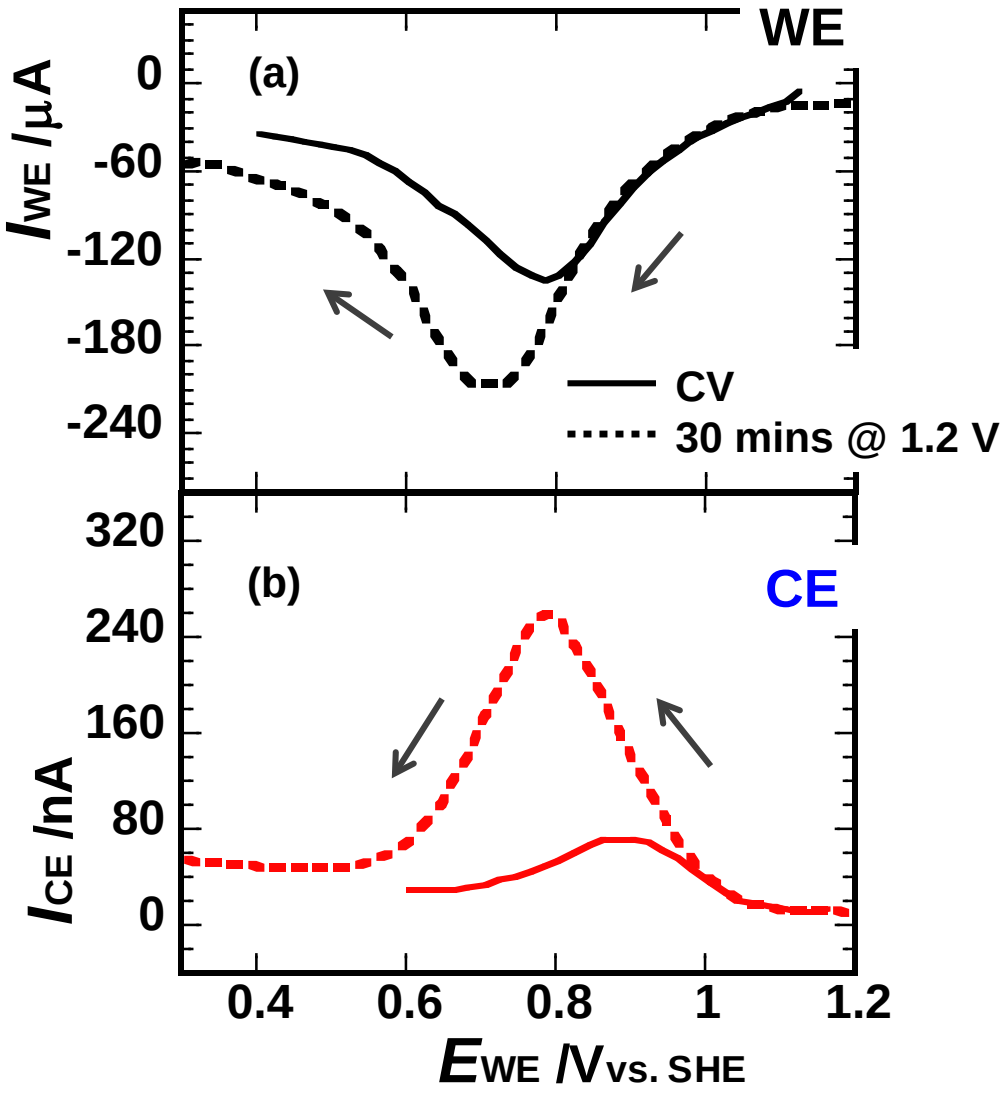

Fig. 4.6. Comparison of I_{WE} and I_{CE} in cathodic scans after 1.) the WE underwent anodic scan from 0.4 to 1.2 V (Solid lines), and 2.) potentiostatic holding at 1.2 V for 30 mins (dotted lines). The scan rate was 100 mV/s for both cases. The temperature was 65 ^{o}C.

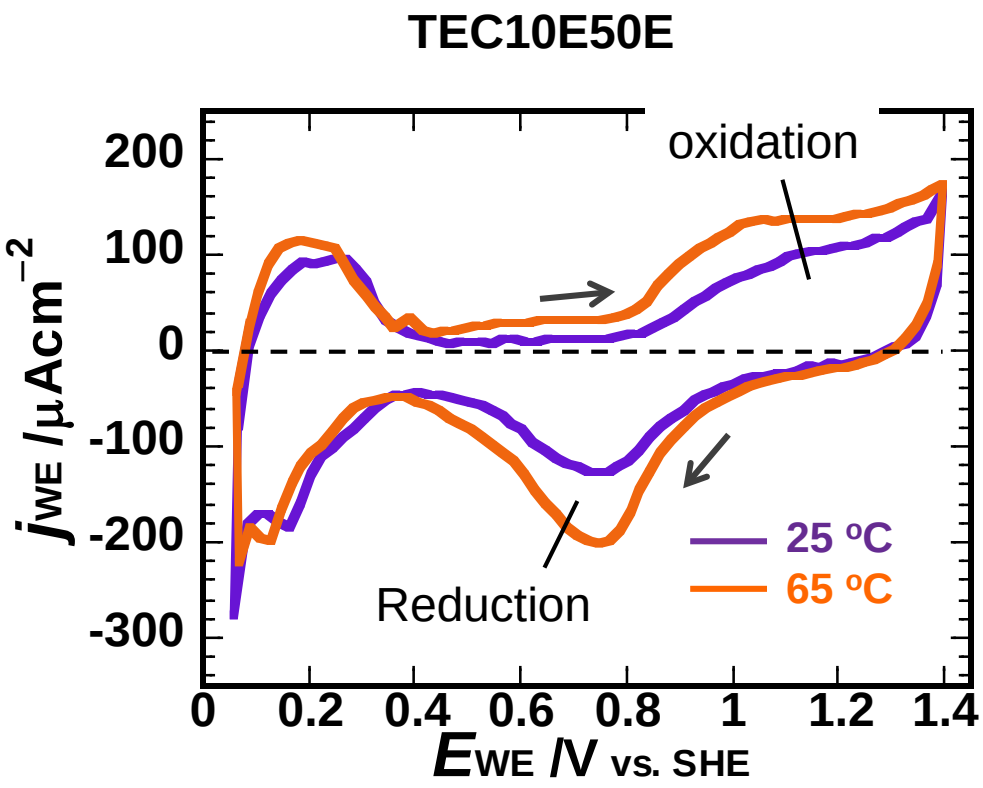

Fig. 4.7. CV of the Pt/C-loaded WE in 0.5 M H_2SO_4 at 25 and 65 °C in a CFDE. The scan rate was 100 mV/s for both.

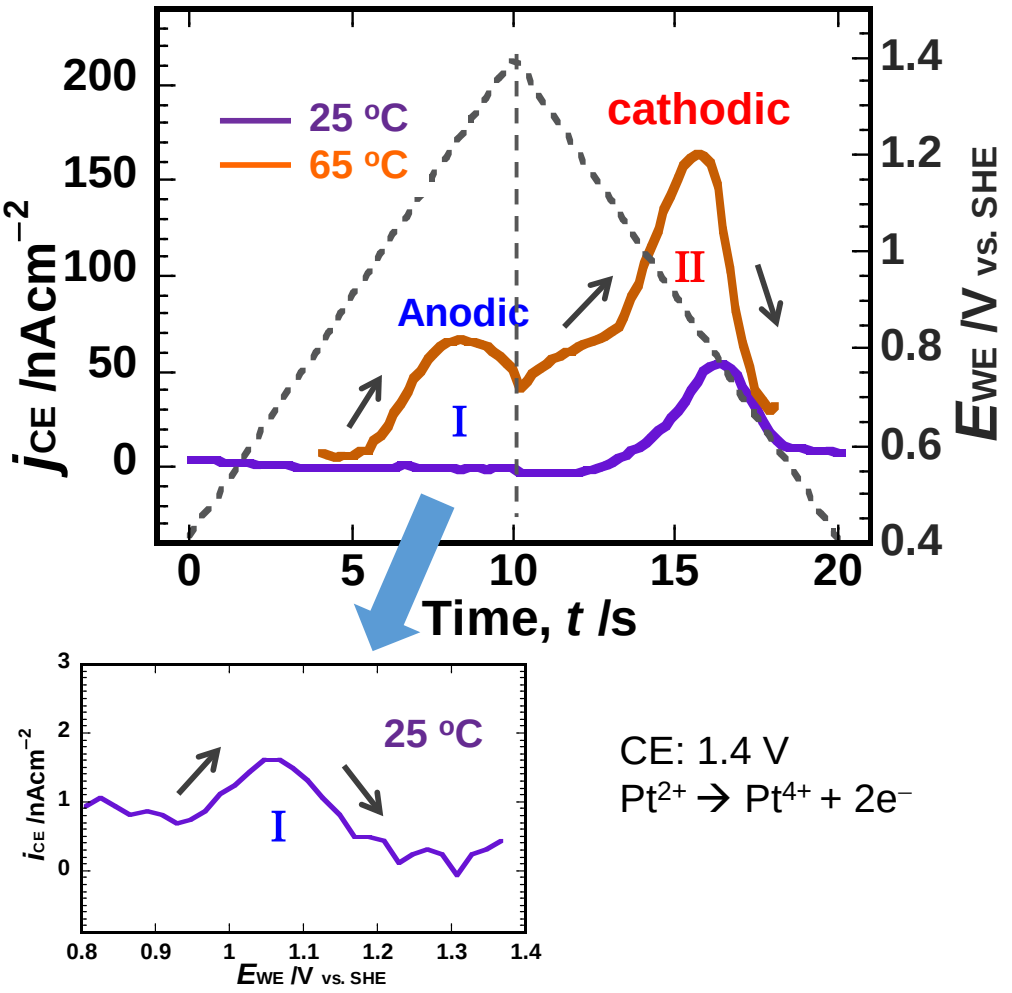

Fig. 4.8. I_{CE} plotted against time at 25 and 65 °C, while the WE (loaded with TEC10E50E) underwent CV at 100 mV/s.

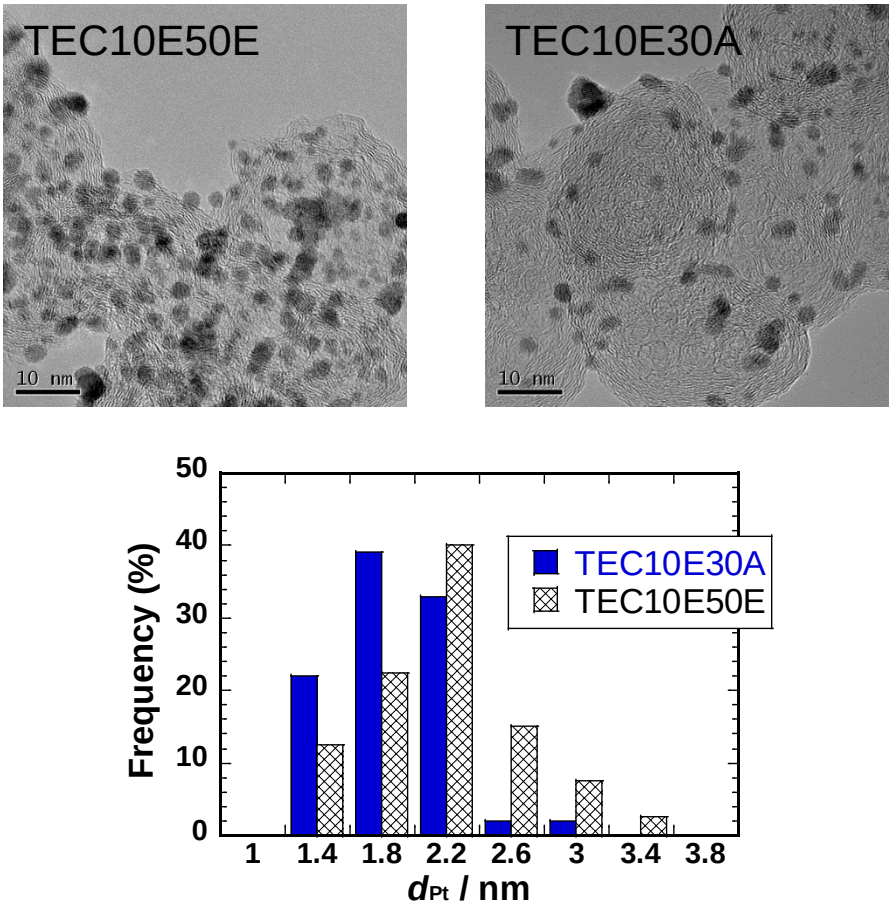

Fig. 4.9. TEM images of as-received TEC10E50E and TEC10E30A Pt/C samples, and comparison of Pt particle size (d_{Pt}) distributions.

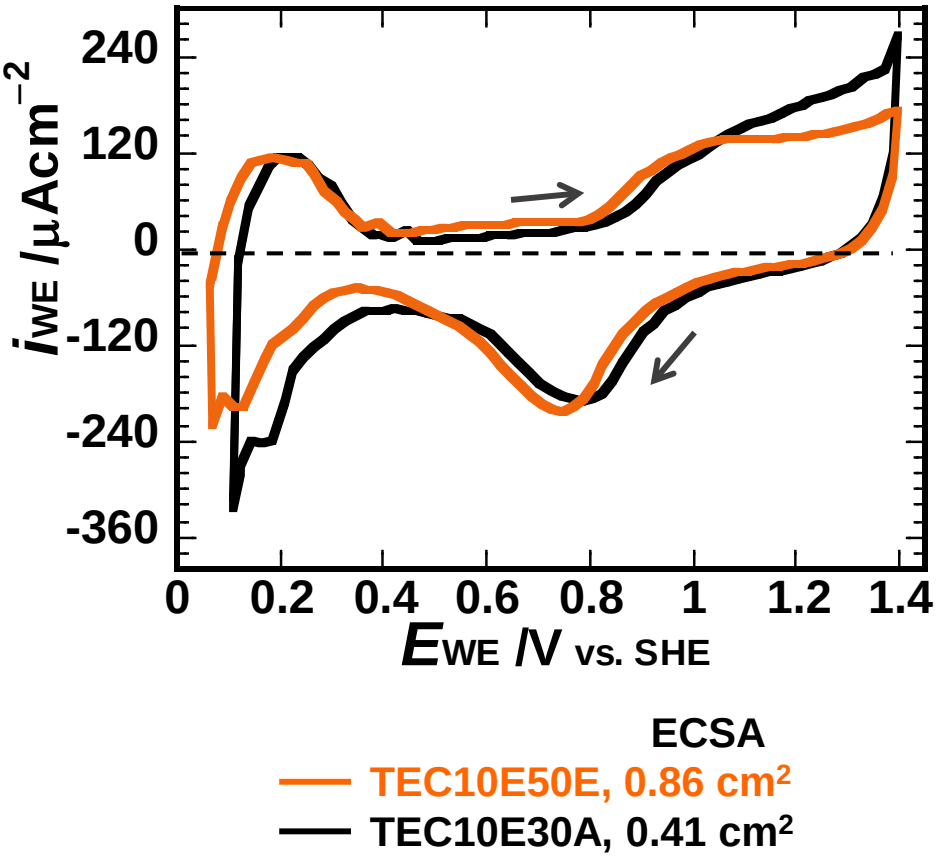

Fig. 4.10. CVs of WE loaded with TEC10E50E and TEC10E30A Pt/C in 0.5 M H_2SO_4 at 65 ^oC, respectively. The scan rate was 100 mV/s.

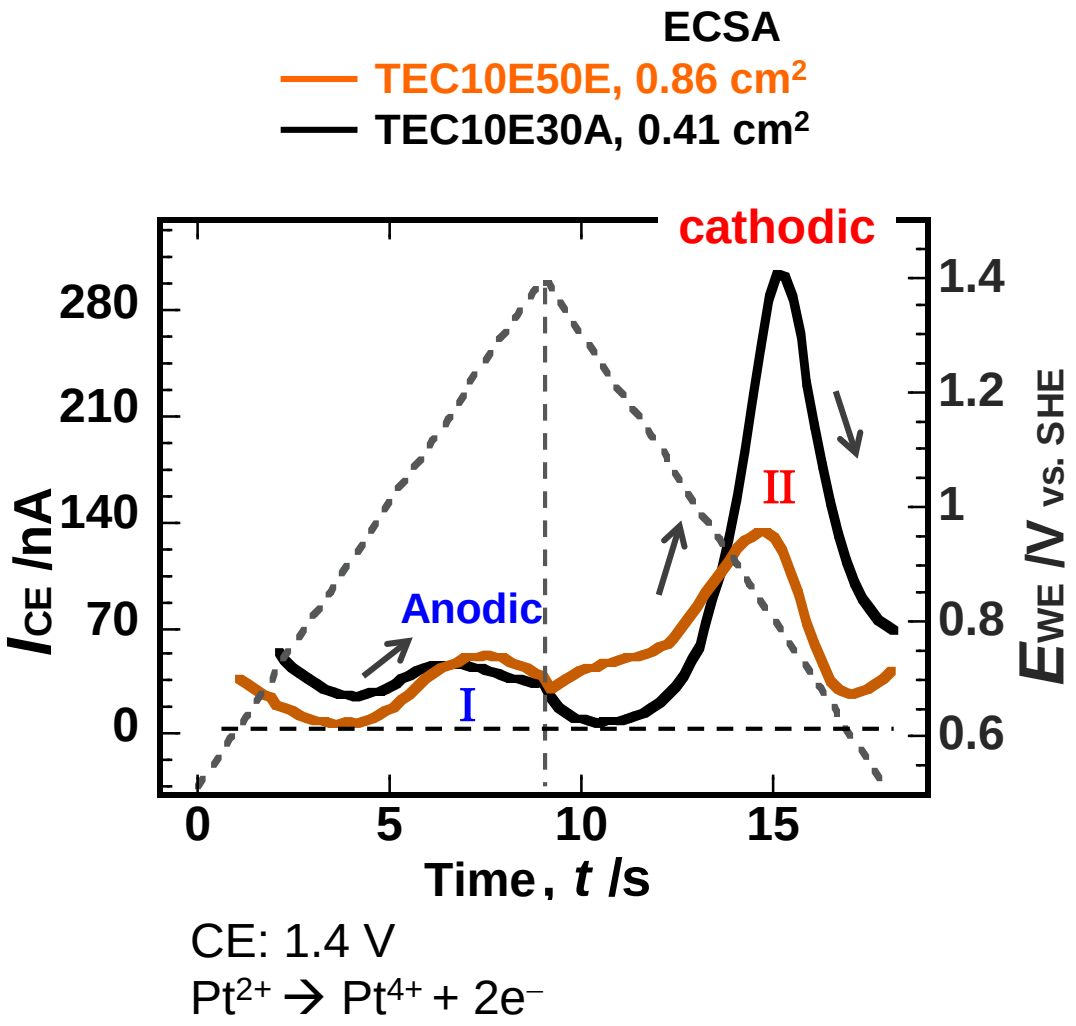

Fig. 4.11. I_{CE} plotted against time at 65 °C, while the WE loaded with TEC10E50E and TEC10E30A underwent CV at 100 mV/s.

Table 4.2. Pt dissolution under simulated start-stop potential cycle (0.4~1.4 V) (pgcm^{-2}cyle^{-1})

		CFDE calculation (3rd cylce)			ICP-MS (average of 300 cycles)
		Anodic	Cathodic	Total	
50E	65 °C	800	1700	2500	1250
	25 °C	4	517	521	580
30A	65 °C	540	5500	6040	1530
	25 °C	13	1800	1813	1000
Bulk		120	4900	5020	

50E: TEC10E50E, 30A: TEC10E30A

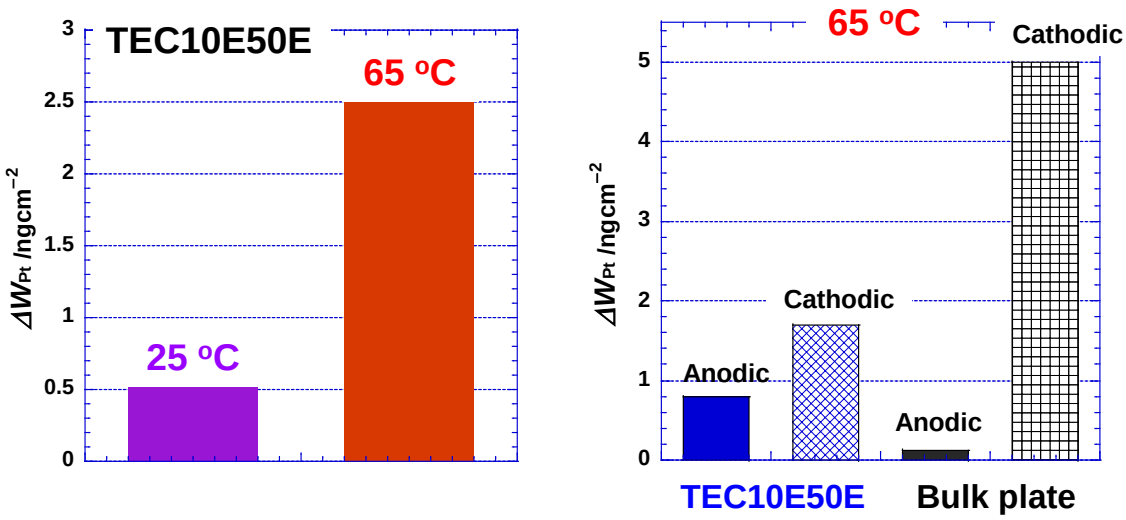

Fig. 4.12. Pt dissolution on TEC1050E at 25 and 65 °C (left), comparison of TEC10E50E with a bulk plate sample at 65 °C.

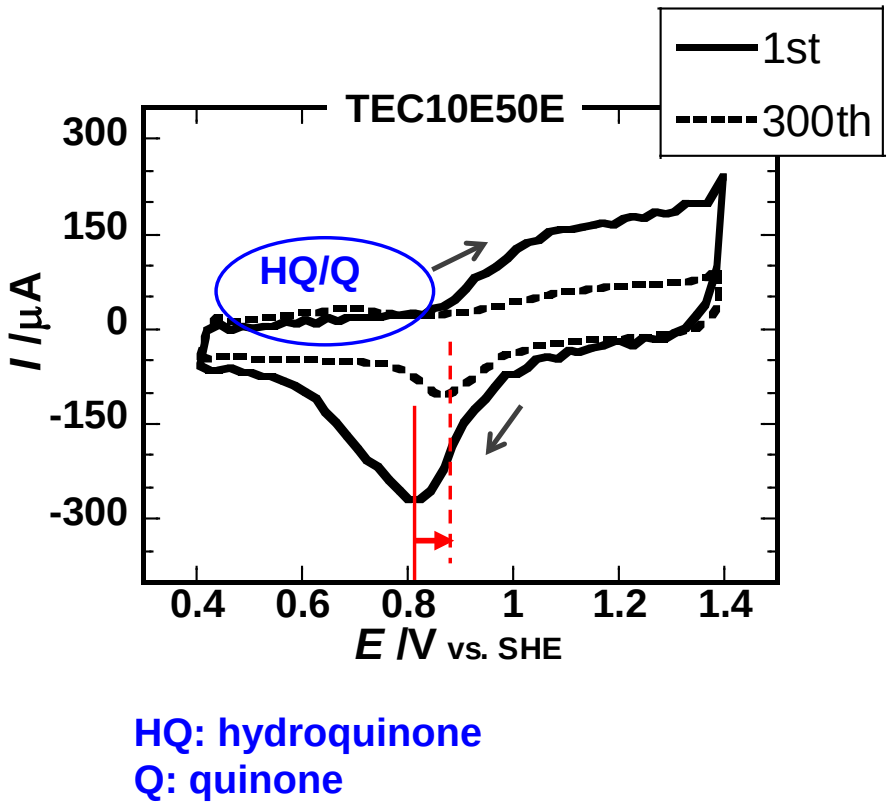

Fig. 4.13. The 1st and 300th cycles of CVs on TEC10E50E in 0.5 M H_2SO_4 at 65 °C in a stationary cell.

Chapter 5

Mechanism of Pt Dissolution Distilled from the Results of In Situ CFDE Analysis

5.1. Introduction

In the previous chapters, I analyzed Pt dissolution using an in situ CFDE method. Both bulk-like unsupported Pt film and commercial carbon supported Pt NPs were tested. In this chapter, I generalize the findings from these data, and try to formulate some new understandings of Pt dissolution.

In 2010, a preliminary model was proposed by Sugawara for explaining the dissolution behaviors under potential cycling [1]. This model discussed the occurrence of Pt dissolution upon potential regions; a place exchange process [2] was attributed for triggering the anodic dissolution above 1.2 V. And in 2014, a similar dissolution model was also proposed by Mayrhofer et al. [3]. In this chapter, the Sugawara's model is updated as the real-time dissolution/potential information was discovered from the in situ CFDE analysis. Though the word *Mechanism* in the chapter title, these proposals are in fact some cautionary hypothesis based on pure electrochemical observations. Besides, the data reported by other two groups [3-4] in parallel to the construction of this dissertation were also included for discussion, since they more or less agreed with the in situ CFDE data in this dissertation and, for this reason, served as good supports when distill the dissolution models.

5.2. Valence of dissolved Pt species

One contribution of in situ CFDE analysis was the understanding of the valence of the dissolved Pt species. Such information was instrumental in development of mechanistic theory or kinetic equations, as qualified by Jerkiewicz and Beauchemin et al. [5]. They coupled ion exchange chromatography with ICP-MS and confirmed the formation of both Pt^{2+} and Pt^{4+} complexes from a Pt polycrystalline foil after potential

cycles in 0.5 M H_2SO_4. According to their analysis, at least 80 % of Pt species presented as Pt^{2+} complex.

In chapter 2, the CFDE analysis revealed that Pt^{2+} complex formed below 1.2 V, and Pt^{4+} above 1.2 V, as illustrated in **Fig. 5.1**. For the formation of Pt^{2+} complex, Eqs. 5.1, 5.2, and 5.3 may be attributed. For Pt^{4+}, possible reactions are Eqs. 5.4, 5.5 and 5.6. Overall, the dissolution of Pt is electrochemical: from metallic Pt atom to Pt ion (Eq. 5.1 or Eq. 5.4). Here, in this chapter, the dissolution mechanism means the rate determining step (rds) for the dissolution process.

$$Pt \rightarrow Pt^{2+} + 2e^- \quad [5.1]$$

$$PtO + 2H^+ \rightarrow Pt^{2+} + H_2O \quad [5.2]$$

$$PtO_2 + 4H^+ + 2e^- \rightarrow Pt^{2+} + 2H_2O \quad [5.3]$$

$$Pt \rightarrow Pt^{4+} + 4e^- \quad [5.4]$$

$$PtO + 2H^+ \rightarrow Pt^{4+} + H_2O + 2e^- \quad [5.5]$$

$$PtO_2 + 4H^+ \rightarrow Pt^{4+} + 2H_2O \quad [5.6]$$

For carbon supported Pt NPs, however, the condition is more complex. Pt degradation during potential cycling included coalescence of NPs, detachment of NPs, and dissolution of Pt NPs. The potential region wherein each of the three processes dominate is different. As illustrated **Fig. 5.2**, coalescence of NPs is mainly responsible in the double layer region where Pt oxide is yet to form, while detachment of NPs proceeded in high potential region where corrosion of the carbon support took place. The dissolution of Pt NPs located in between these two regions. The anodic dissolution took place in the region 0.8 to 1.2 V, and the cathodic one in 1.1 V to 0.6 V. And both dissolutions produced

Pt^{2+} complex, according the CFDE analysis.

5.3. Electrochemical oxidation and reduction of Pt

A prerequisite for the mechanism of Pt dissolution is a comprehensive understanding of the oxidation and consecutive reduction of Pt surface under potential cycling. The current knowledge for the two processes is incomplete. For oxidation of bulk Pt, a mechanism was proposed by Jerkiewicz et al. in 2004 from their analysis using EQCM and auger electron spectroscopy [2]. Under potential scan up to 1.4 V, they argued that the oxidation of a Pt surface proceeded from a chemisorption of O atom (Eq 5.7) to half monolayer, and near 1.1 V, a place exchange initiates between the adsorbed O and Pt atoms (Eq. 5.8), while the second half-monolayer O_{ad} starts to form. This model of Pt oxidation ruled out existence or formation of transient oxide like PtOH, which were found later during the oxidation of Pt NPs [6-8]. Besides, the model also excluded the formation of PtO_2 at potentials less than 1.4 V, which seems favorable for explaining the cathodic dissolution observed on bulk Pt.

$$Pt + H_2O \rightarrow Pt\text{-}O_{ad} + 2H^+ + 2e^- \quad [5.7]$$

$$Pt\text{-}O_{ad} \rightarrow PtO \text{ (place exchange)} \quad [5.8]$$

For Pt NPs, as reported by Imai et al. [6], Nilsson et al. [7], and Fuller et al. [8], the oxidation process may proceed from chemisorption of both OH (Eq. 5.9) and O (Eq. 5.7) on Pt surface, followed by the conversion to PtO (5.10) and PtO_2 (Eq. 5.11). The process were found either in aqueous solutions [6] or PEFC single cell [8]. The oxide is an amorphous layer containing both PtO and PtO_2; several stable structures are shown in **Fig.**

5.3 [8].

$$Pt + H_2O \rightarrow PtOH + H^+ + e^- \quad [5.9]$$

$$PtOH \rightarrow PtO + H^+ + e^- \quad [5.10]$$

$$PtOH + H_2O \rightarrow PtO_2 + 3H^+ + 3e^- \quad [5.11]$$

In addition, as pointed out by Fuller et al [8], the formation of PtO_2 also differs on the atomic site, since the chemical potential for each site to form PtO_2 is different. Their model for oxidation and reduction of a Pt NP in acidic solutions is illustrated in **Fig 5.4**. They proposed that for planar site the process proceeded though Eq. 5.9 and Eq. 5.10, while at edge site, the oxidation may proceed through a single step by Eq. 5.11. The simulated CV shape using their model fitted well with the measured one [8].

$$Pt + 2H_2O \rightarrow PtO_2 + 4H^+ + 4e\text{-} \quad [5.12]$$

As a result, the potential region for reduction of the PtO_2 at different site is also different. The PtO_2 on the planar site is reduce at first near 0.8 V, then the reduction of edge site took place near 0.6 V.

5.4. Dissolution mechanism of Pt under potential cycling

The in situ CFDE analysis in chapter 2, 3, and 4 revealed that Pt complexes were produced during both anodic and cathodic scans. The structure of each complex is unknown yet. In general, the anodic dissolution was trivial compared with the cathodic dissolution. A similar result was also reported by Gaberscek et al. using in situ ICP-MS

analysis [4]. Here, in this chapter, I discuss a model for the dissolution of Pt under potential cycling. The model is illustrated in **Fig. 5.5**. The model divided one potential cycle into 5 regions. The main reactions on Pt surface are oxidation and reduction, Pt dissolution reactions are trivial processes.

5.4.1. Anodic dissolution

In region 1, 0.4 to 0.8 V, we have a bare Pt surface, may be with some adsorption of H_2O molecules. No tangible dissolution occurs in this region. Then, in region 2, the anodic dissolution of Pt^{2+} took place from approximately 0.8 to 1.2 V. The reaction may go through a single step by Eq. 5.1. The Pt^{2+} is formed directly from metallic Pt atom. The chemical dissolution pathway from PtO to Pt^{2+} (Eq. 5.3) is unlike to occur. As pointed by Myers et al. [9]: the Pt oxide was protective against dissolution under potential holding. And in chapter 4, the in situ CFDE analysis showed that the anodic dissolution of Pt^{2+} did decay after 1.1 V because of Pt oxide formation.

Then, let us look into the trivial Pt^{2+} dissolution on an atomic level. As illustrated in **Fig. 5.5**, on the surface Pt, Pt atoms may present at some edge sites or at the planar site. Eq. 5.1 may prefer to occur on the edge site Pt atoms, which is more unstable than the ones on the planar site, and more likely to form the stable Pt^{2+} aqueous complex. The number of edge-site Pt atoms is rare, thus, the anodic dissolution was trivial at 25 ^{o}C. However, at an elevated temperature, like 65 ^{o}C, the number of such particles may increase, and as a result, the anodic dissolution boosted.

Then, as the potential goes to more positive region, region 3, place exchange occurs [4] and dissolution of Pt^{4+} was triggered. However, at the current stage, it is difficult to predict whether the Pt^{4+} was from electrochemical oxidation of PtO or from chemical

process of PtO_2.

5.4.2. Cathodic dissolution

In region 4, 1.2 to 0.6 V, where the Pt oxide is reduced, the cathodic dissolution of Pt^{2+} occurs. For this dissolution, the electrochemical reduction of PtO_2 (Eq. 5.5) seems favorable at this stage. In chapter 2, 3, and 4, the Pt^{2+} was produced proceeded in the early stage of oxide reduction, wherein the PtO_2 at the planar site is reduced, according to Fuller et al. [8]. Thus, unlike the anodic dissolution, the cathodic dissolution of Pt^{2+} may prefer to occur on the planar site, where Pt lattice was distorted during the place exchange process.

At the edge site, however, the PtO_2 may form without the place exchange; the O atoms stay outside the Pt lattice. At the planar site, however, the PtO_2 forms with the penetration of O atoms into the Pt surface, and distorts the nearby lattice. The distorted PtO_2 may be more likely to go through Eq. 5.3 during reduction than the edge-site PtO_2.

At last, when the reduction is finished, the Pt surface goes back to region 5. After oxide formation and reduction of the Pt surface, some unstable atoms may be formed, which is available for dissolution in the next cycle.

The above dissolution model for Pt was tentative, since it was deduced from macro-level data. When micro-level data with parameters like atomic site, plane orientations well defined are ready, revision of the model will be inevitable, and hopefully leads us to the ultimate mechanism for Pt dissolution. At this stage, the grand generalization of Pt dissolution mechanism is still premature. The model I presented in this chapter is more or less a discussion for some detailed issues, since the understanding of them is absolutely a prerequisite.

5.5. Conclusion

In this chapter, I sketched a dissolution model for Pt under potential cycling in 0.5 M H_2SO_4. The model is distilled from the in situ CFDE analysis, and covers both anodic and cathodic Pt dissolutions. The anodic dissolution goes through a single step from metallic to Pt^{2+}, and consumes unstable Pt atoms at edge sites. The cathodic dissolution is from reduction of PtO_2 at planar sites.

Reference

1. Y. Sugawara, Doctoral dissertation, Tokyo Institute of Technology, 2010.
2. G. Jerkiewicz, G. Vatankhah, J. Lessard, M.P. Soriaga, and Y. Park, *Electrochim. Acta*, **49**, 1451 (2004).
3. A.A. Topalov, S. Cherevko, A.R. Zeradjanin, J.C. Meier, I. Katsounaros, and K.J.J. Mayrhofer, *Chem. Sci.*, **5**, 631 (2014).
4. P. Jovanovič, A. Pavlišič, V.S. Šelih, M. Šala, N. Hodnik, M. Bele, S. Hočevar, and M. Gaberšček, *ChemCatChem*, **6**, 449 (2014).
5. L. Xing, G. Jerkiewicz, and D. Beauchemin, *Analytica Chimica Acta*, **785**, 16 (2013).
6. H. Imai, K. Izumi, M. Matsumoto, Y. Kubo, K. Kato, and Y. Imai, *J. Am. Chem. Soc.*, **131**, 6293 (2009).
7. L. R. Merte, F. Behafarid, D. J. Miller, D. Friebel, S. Cho, F. Mbuga, D. Sokaras, R. Alonso-Mori, T. Weng, D. Nordlund, A. Nilsson, and B. R. Cuenya, *ACS Catal.*, **2**, 2371 (2012).
8. E.L. Redmond, B.P. Setzler, F.M. Alamgir, and T.F. Fuller, *Phys. Chem. Chem. Phys.*, **16**, 5301 (2014).
9. J.A. Gilbert, N.N. Kariuki, R. Subbaraman, A.J. Kropf, M.C. Smith, E.F. Holby, D. Morgan, and D.J. Myers, *J. Am. Chem. Soc.*, **134**, 14823 (2012).

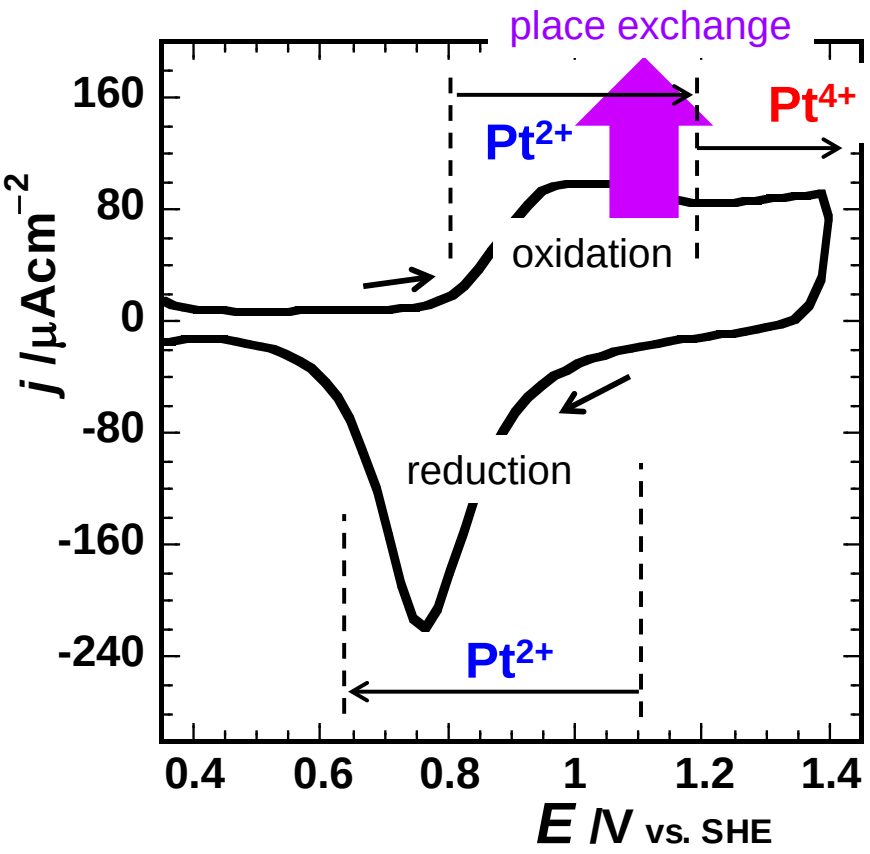

Fig. 5.1. Potential regions for dissolution of Pt^{2+} and Pt^{4+} from bulk samples under potential cycling in 0.5 M H_2SO_4.

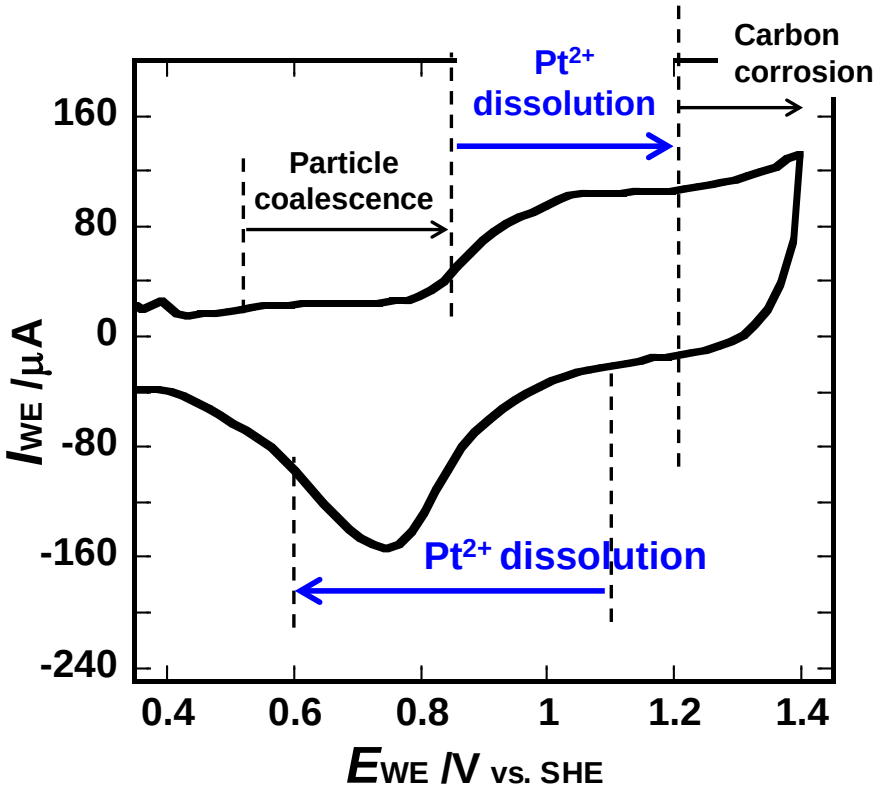

Fig. 5.2. Dominant degradation mechanism of Pt NPs upon potential regions under potential cycling.

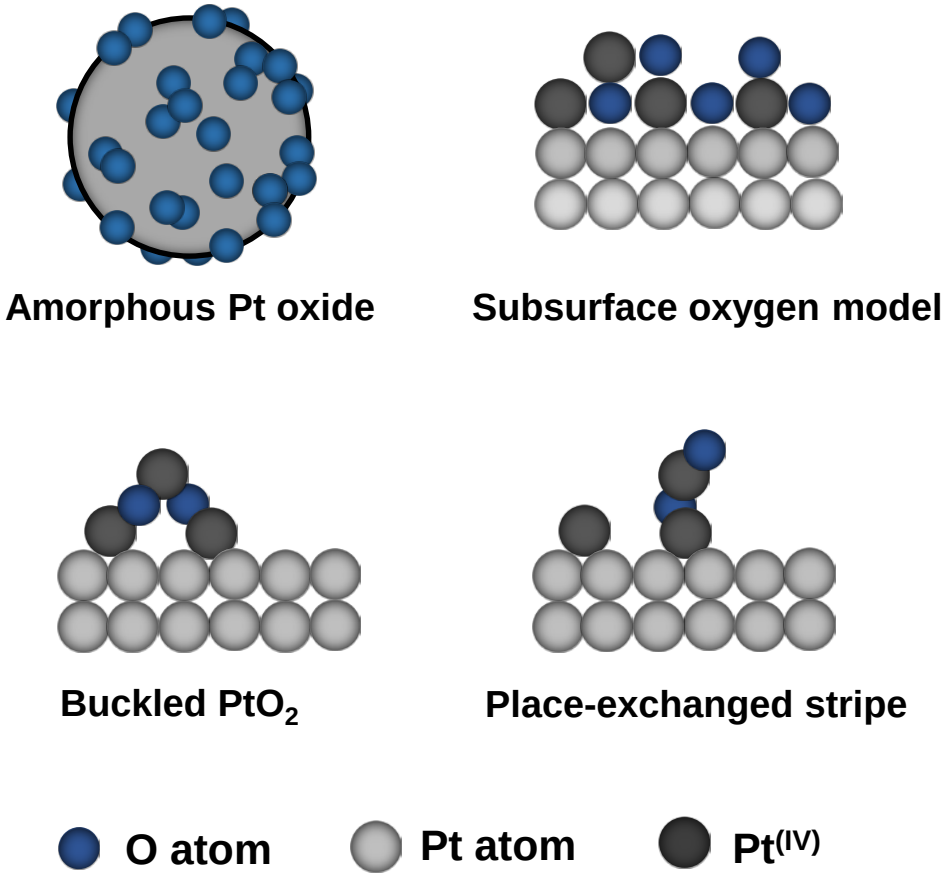

Fig. 5.3. Four types of Pt oxide formed on a Pt NP [8].

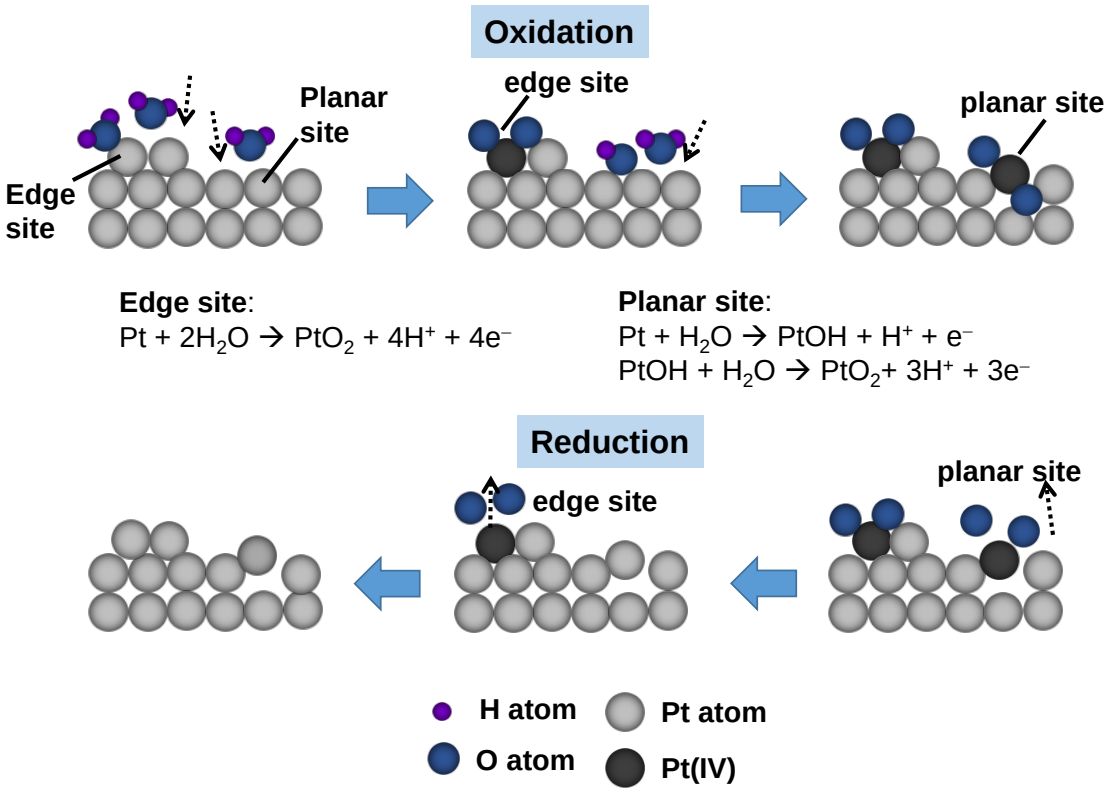

Fig. 5.4. Proposed oxidation and reduction of Pt surface under potential cycling [8].

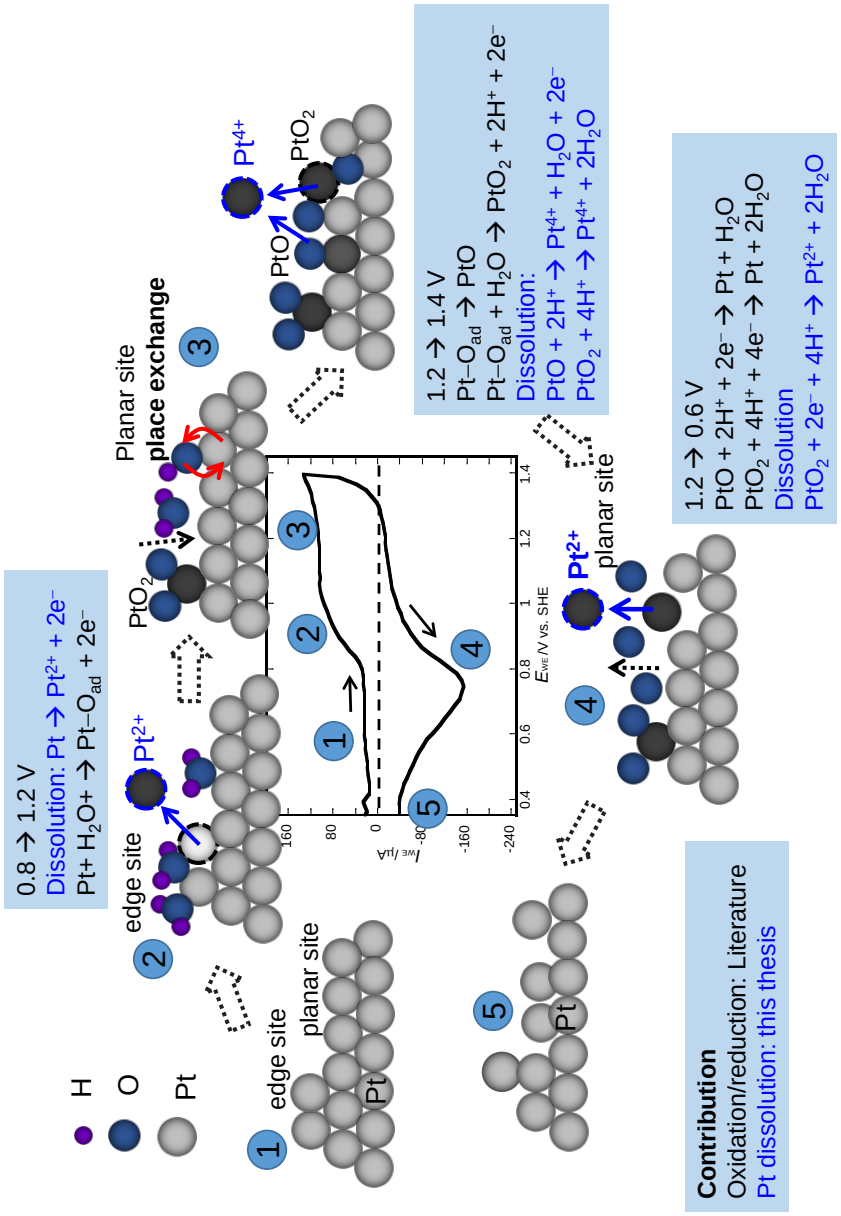

Fig. 5.5. Model of Pt dissolution under potential cycling.

Chapter 6

Summary

Chapter 1

In chapter 1, I introduced the background and motivation of the dissertation. I highlighted the merits that PEFC technology will bring to us, as well as the challenges for the massive production of FC vehicles and residential units in the next few decades. Pt dissolution is regarded as one of the critical issues that concerns the durability of PEFCs. From a scientific perspective, understanding the nature of this phenomenon is a necessary step for improving the lifetime of PEFCs.

Chapter 2

In chapter 2, I discussed the in situ CFDE method for monitoring Pt dissolution under potential cycling. For simplicity, I used an electroplated Pt film as a bulk-like model electrode. The in situ CFDE analysis revealed that dissolution of Pt^{2+} may initiate near 0.8 V (SHE) in an anodic scan. The amount of dissolved Pt^{2+} below 1.0 V was calculated using collector current (I_{CE}) and was confirmed by ex-situ inductively coupled plasma mass spectrometry. The amount of Pt^{2+} and Pt^{4+} dissolved in different potential regions during potential cycling was quantified by I_{CE} for the first time.

In addition, I also investigated the effect of scan rate (ν) on the instantaneous dissolution of Pt under potential cycling in the range of 0.5–200 mV/s. In an anodic scan, ν affects the initiation and inhibition of Pt dissolution during oxide formation. Slow scans induced Pt dissolution earlier, but soon suppressed it. The extent of dissolution, however, did not show significant changes like the oxide development did when changing the ν. In a cathodic scan, the electrochemical dissolution of Pt^{2+} during oxide reduction speeded up with ν.

Chapter 3

In chapter 3, the effect of Cl^- on Pt dissolution under both potentiostatic and potential cycling conditions was reported, using a channel-flow multi-electrode (CFME) as an in situ detection method. To avoid the contamination of the entire CFME system by Cl^-, a liquid-phase chloride ion gun is placed upstream of the double electrode. Under potentiostatic conditions, Cl^- enhanced Pt dissolution by forming $PtCl_4^{2-}$ at potentials below 1.0 V and $PtCl_6^{2-}$ above 1.2 V. Under potential cycling conditions, Cl^- accelerated Pt dissolution above 1.2 V by the enhanced formation of both $PtCl_6^{2-}$ and $PtCl_4^{2-}$. The cathodic dissolution of Pt^{2+} during PtO_2 reduction was also increased in the presence of Cl^-.

Chapter 4

In chapter 4, I evaluated Pt dissolution from standard commercial PEFC catalyst, which is in the form of Pt nanoparticles supported on carbon (Pt/C). The in situ CFDE analysis focused on the detection of Pt^{2+}, which is the dominant Pt species produced during potential cycles below 1.4 V. On Pt/C, I observed both anodic and cathodic dissolution of Pt^{2+} under potential cycling; the later dominated at an upper potential limit (EU) of 1.2 and 1.4 V. Both dissolutions were enhanced by elevating the temperature from 25 to 65 ^oC. In particular, the comparison between two Pt/Cs with a bulk Pt plate showed that Pt dissolution may depend on several parameters besides particle size. Moreover, I also evaluated Pt dissolution from Pt/C by ICP-MS. The results showed similarity with the CFDE data. In general, the CFDE showed its applicability to dissolution tests using supported nanoparticles. In the future, application of the in situ CFDE method for other Pt catalyst is also expected.

Chapter 5

In chapter 5, I sketched a model for Pt dissolution under potential cycling in 0.5 M H_2SO_4. The model is distilled from the in situ CFDE analysis, and covers both anodic and cathodic Pt dissolutions from an electrochemical perspective. The anodic dissolution goes through a single step from metallic to Pt^{2+}, and consumes unstable Pt atoms at edge sites. The cathodic dissolution is from reduction of PtO_2 at planar sites. I hope the dissolution model may provide some strategic information for improve the durability of PEFCs.

Chapter 6

In chapter 6, I summarized the dissertation.

Acknowledgements

With the completion of this thesis, I would like to express my sincere gratitude to my advisor Prof. Dr. Atsushi Nishikata (西方　篤　教授) for his support of my study, research, and life in Japan. His supervision and guidance helped me in all the time of my research and writing of this thesis.

I would like to thank my assistant advisor, Assoc. Prof. Dr. Eiji Tada, for teaching me experimental techniques; his advices and discussions helped my study and research.

Besides, I want to thank the rest of my thesis committee: Prof. Susa, Assoc. Prof. Kawamura, and Assoc. Prof. Ueda, for reviewing my thesis. Their comments, encouragement, and questions helped me to obtain the final shape of this thesis.

I would like to thank Mrs. Maki Kajitani for her help with my lab activities.

I would like to thank Prof. Emeritus Dr. Tooru Tsuru, Dr. Hiroo Numata and Ms. Yuko Harada for their help.

I also thank Mr. Ooi, Miss Kaneko, and all the labmates for their help and all the fun we have had in the last 5 years.

Last but not least, I want to thank MEXT for providing scholarship for my PhD study.